

**DESIGN AND ANALYSIS OF TITANIUM NITRIDE
PLASMONIC NANOPARTICLE EMBEDDED AND
UPCONVERTER INCORPORATED KESTERITE
TANDEM SOLAR CELL**

by

Nowshin Akhtary

1018062201

MASTER OF SCIENCE
IN
ELECTRICAL AND ELECTRONIC ENGINEERING



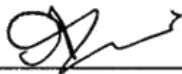
Department of Electrical and Electronic Engineering (EEE)
Bangladesh University of Engineering and Technology

Dhaka, Bangladesh

July 2023

This thesis titled, “**DESIGN AND ANALYSIS OF TITANIUM NITRIDE PLASMONIC NANOPARTICLE EMBEDDED AND UPCONVERTER INCORPORATED KESTERITE TANDEM SOLAR CELL**”, submitted by Nowshin Akhtary, Roll No.: 1018062201, Session: October 2018, has been accepted as satisfactory in partial fulfilment of the requirements for the degree of MASTER OF SCIENCE IN ELECTRICAL AND ELECTRONIC ENGINEERING on 22 July 2023.

BOARD OF EXAMINERS



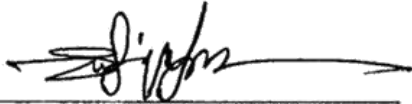
Dr. Ahmed Zubair
Associate Professor
Department of EEE, BUET, Dhaka

Chairman
(Supervisor)



Dr. Md. Aynal Haque
Professor and Head
Department of EEE, BUET, Dhaka

Member
(Ex-Officio)



Dr. Md. Shafiqul Islam
Professor
Department of EEE, BUET, Dhaka

Member



Dr. Apratim Roy
Professor
Department of EEE, BUET, Dhaka

Member



Dr. Mohammad Ryyan Khan
Associate Professor
Department of EEE, East West University,
Dhaka

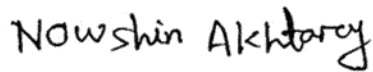
Member
(External)

Candidate's Declaration

This is to certify that the work presented in this thesis entitled, "DESIGN AND ANALYSIS OF TITANIUM NITRIDE PLASMONIC NANOPARTICLE EMBEDDED AND UPCONVERTER INCORPORATED KESTERITE TANDEM SOLAR CELL", is the outcome of the research carried out by Nowshin Akhtary under the supervision of Dr. Ahmed Zubair, Associate Professor, Department of EEE, Bangladesh University of Engineering and Technology (BUET), Dhaka 1205, Bangladesh.

It is also declared that neither this thesis nor any part thereof has been submitted anywhere else for the award of any degree, diploma, or other qualifications.

Signature of the Candidate



Nowshin Akhtary

1018062201

Dedication

To my family

Contents

Certification	ii
Candidate's Declaration	iii
Dedication	iv
List of Figures	viii
List of Tables	xv
Acknowledgement	xvi
Abstract	xvii
1 Introduction	1
1.1 Evolution of Solar Cells	3
1.1.1 First Generation Solar Cells	4
1.1.2 Second Generation Solar Cells	4
1.1.3 Third Generation Solar Cells	5
1.2 Kesterite Solar Cells	6
1.3 Plasmonic Solar Cells	7
1.4 Upconverter Solar Cells	10
1.5 Objectives of the Thesis	11
1.6 Thesis Overview	13
2 Plasmonic Light Trapping and Solar Cell Simulation	15
2.1 Localized Surface Plasmon Resonance	15
2.1.1 Normal Modes of Sub-Wavelength Metal Particles	17
2.2 Plasmonic Light Trapping in Thin-Film Solar Cells	18
2.2.1 Light Scattering Using Particle Plasmons	19
2.2.2 Light Concentration Using Particle Plasmons	20
2.2.3 Light Trapping Using SPPs	21
2.3 Alternative Plasmonic Materials	22
2.3.1 Limitations of Noble Metals	23

2.3.2	Optical Properties of Materials	25
2.3.3	Finding Alternatives.....	26
2.4	Scattering of Light by NPs	28
2.4.1	Scattering Cross-Section.....	28
2.4.2	Absorption Cross-Section	29
2.5	Near Field and Far Field.....	30
2.6	Solar Cell Model	32
2.7	Optical Simulation Model	36
2.8	Electrical Simulation Model.....	37
3	Light Absorption Enhancement by TiN Plasmonic Nanospheres	40
3.1	Introduction	40
3.2	Structural Design and Simulation Method	41
3.2.1	Structural Design	41
3.2.2	Simulation Methods	42
3.3	Effect of Constituent Material of Nanospere.....	44
3.4	Exploring TiN NP and Core-shell TiN NP	46
4	Light Trapping Using TiN Dimer of Spherical Nanoparticles	50
4.1	Introduction	50
4.2	Structural Design and Simulation Methods.....	51
4.2.1	Structural Design	51
4.2.2	Simulation Methods	52
4.3	Results and Discussion.....	54
4.3.1	Effect of Different Material-Based Plasmonic Spherical Dimer Nanoparticle.....	54
4.3.2	Absorption Enhancement by TiN-Based Dimer NP	59
4.3.3	Impact of Light Polarization	61
4.3.4	Impact of the Distance Between the Spheres of Dimer	63
4.3.5	Dependency on the Radius of the Dimer Spherical NP	64
5	Effiecient Light Trapping by TiN Plasmonic Bowtie Nanoparticles	66
5.1	Introduction	66
5.2	Structure and Simulation Method.....	67
5.2.1	Structural Design	67
5.2.2	Simulation Method	68
5.3	Results and Discussion.....	68
5.3.1	Effect of the Variation of Bowtie Nanoparticle Thickness	69
5.3.2	Impact of Light Polarization	72
5.3.3	Dependency on the Gap Distance Between the Triangles of the Bowtie	77

5.3.4	Effect of Varying the Shape and Thickness of Dielectric Material . . .	77
6	Titanium Nitride Bowtie Nanoparticle Incorporated Kesterite Solar Cell	82
6.1	Introduction	82
6.2	Photovoltaic Nanostructure Design and Simulation Methods.....	84
6.2.1	Structural Design	84
6.2.2	Simulation Methods.....	84
6.3	Results and Discussions	85
6.3.1	Current Density-Voltage and Power-Voltage Characteristics for Dif- ferent Shaped NP	85
6.3.2	Light Absorption Enhancement in Photovoltaic Cells by the NPs	89
6.3.3	Light Polarization Sensitivity of Bowtie-shaped NP Incorporated CZTS Solar Cells.....	93
7	Upconverter Solar Cell	95
7.1	Introduction	95
7.2	Upconversion Materials	97
7.2.1	Lanthanides.....	98
7.2.2	Organic Molecules.....	99
7.3	Downconversion Materials.....	100
7.4	Efficiency Improvement by Integration of Upconverter Layer	101
7.5	Designing Different Absorber Layer for Tandem Solar Cell	103
8	Conclusions	105
8.1	Conclusions	105
8.2	Future Works.....	107
	References	108

List of Figures

1.1	A chart of the highest confirmed conversion efficiencies for research cell for a range of photovoltaic technologies plotted from 1976 to the present. . . .	2
1.2	Photovoltaic cell generations.	3
1.3	First generation solar cell.	4
1.4	Second generation thin film CZTS solar cell.	5
1.5	Third generation plasmonic perovskite solar-cell configurations.	6
1.6	Crystal Structures of (a) Si, (b) CdTe (c) CIGSe and (d) CZTS materials. . .	7
1.7	Plasmonic solar cell.	8
1.8	Periodic table highlighting the Lanthanides.	11
1.9	Schematics of the energy levels involved in the upconverting processes occurring in the materials (Yb^{3+} and Er^{3+}).	12
2.1	(a) Surface plasmon polariton. (b) Localized surface plasmons.	16
2.2	Sketch of a homogeneous sphere placed into an electrostatic field.	18
2.3	(a) Light trapping by scattering from metal nanoparticles at the surface of the solar cell. (b) Light trapping by the excitation of localized surface plasmons in metal nanoparticles embedded in the semiconductor. The excited particles' near-field causes the creation of electron-hole pairs in the semiconductor. (c) Light trapping by the excitation of surface plasmon polaritons at the metal/semiconductor interface.	18
2.4	Fraction of light scattered into the substrate, divided by total scattered power, for different sizes and shapes of Ag particles on Si. Also plotted is the scattered fraction for a parallel electric dipole that is 10 nm from a Si substrate.	20
2.5	Two-dimensional calculation of the in-coupling cross-section for SPP and photonic modes as a function of wavelength for a 200-nm-thick Si slab.	21
2.6	The imaginary part of permittivity of gold in the optical range (solid line), the individual contributions from free electron losses (intraband transitions) and interband transition losses are shown in dotted lines.	23
2.7	Optical constants of metal nitride thin films deposited using DC reactive sputtering. The (a) real and (b) imaginary parts of dielectric functions.	28

2.8	Standard scattering geometry for measuring differential scattering cross-section.....	29
2.9	Polar plot for far-field spectra in xy plane depending on incident light for the 100 nm radius nanosphere consisting of TiN and Ag.....	31
2.10	Color map showing the spatial (a) xy, (b) zx, (c) yz distribution of E for TiN monomer NP placed on top of a thin Si ₃ N ₄ on a Si substrate.	32
2.11	A p-n junction solar cell.	32
2.12	The equivalent electrical circuit of a single solar cell.	33
2.13	Current-voltage characteristic of a solar cell.....	34
2.14	Yee grid in three-dimensional simulation domains.....	37
3.1	Illustration of spherical monomer nanoparticle on a 30 nm thin Si ₃ N ₄ underlayer on p-n Si photovoltaic cell.....	41
3.2	(a) Light trapping by scattering from metal nanoparticles at the surface of the solar cell. (b) Light trapping by the excitation of localized surface plasmons in metal nanoparticles embedded in the semiconductor. The excited particles' near-field causes the creation of electron-hole pairs in the semiconductor. (c) Plasmonic NP incorporated p-n junction PV cell.	42
3.3	(a) f_{sub} , (b) Q_T , (c) Q_{sc} , and (d) Q_{ob} as a function of wavelength for 100 nm radius nanosphere consisting of Ag, Au, Al, and TiN on a 30 nm thick Si ₃ N ₄ underlayer on Si substrate.	45
3.4	Polar plot for far-field spectra in xy plane depending on incident light for the 100 nm radius nanosphere consisting of (a)TiN(b)Ag, (c) Au, and (d) Al at 680 nm incident wavelength.....	46
3.5	Percentage of power absorbed after addition of each layer of (a) Ag, (b) Au, (c) Al, (d) TiN NP incorporated Si absorber layer solar cells.	47
3.6	(a) Q_T (b) Q_{sc} (c) f_{sub} (d) Q_{ob} as a function of wavelength for 100 nm radius nanosphere no plasmonic NP, TiN NP, and TiN core with Si ₃ N ₄ coating NP on a 30 nm thick Si ₃ N ₄ underlayer on Si absorber layer.....	48
3.7	(a) Power absorbed in TiN and TiN core with Si ₃ N ₄ coating NPs incorporated Si absorber layer for solar cells. (b) Absorption enhancement, g for TiN plasmonic nanosphere with different radii.	49
3.8	(a) power-voltage and (b)current density-voltage characteristic of 100 nm TiN monomer on si substrate layer.....	49
4.1	(a) Illustration of spherical dimer TiN nanoparticle on a 30 nm thin Si ₃ N ₄ underlayer on Si substrate acting as the absorber layer of the photovoltaic cell. (b) Perspective view and (c) cross-sectional view of a single dimer of spherical nanoparticles.	50

4.2	A cross-section of the simulation setup. Light from the source was incident on the particle in the negative z-direction.....	51
4.3	(a) f_{sub} , (b) Q_T , (c) Q_{sc} , and (d) Q_{ab} as a function of wavelength for 100 nm radius dimer NPs consisting of Ag, Au, Al, TiN, and TiN with Si_3N_4 coating on a 30 nm thick Si_3N_4 underlayer on Si substrate.	53
4.4	Schematic of the LSPR plasmon modes for NP dimers. The coupling of the dipoles in the two spheres of the dimer, created by the plasmon, can occur in the direction of the dimer axis or perpendicular to it.	54
4.5	Color map showing the xy distribution of $ E $ for (a) Ag, (b) Au, (c) Al (d) TiN (e) (d) TiN with Si_3N_4 coating dimer NP placed on top of a 30 thin Si_3N_4 on a Si substrate.	55
4.6	The E-field spectra at (a) yz, and (b) xy plane for spherical dimer NPs comprised of different materials placed on top of a 30 thin Si_3N_4 on a Si substrate.	56
4.7	Color map showing the yz distribution of $ E $ for (a) Ag, (b) Au, (c) Al (d) TiN (e) TiN with Si_3N_4 coating dimer NP placed on top of a 30 thin Si_3N_4 on a Si substrate.....	57
4.8	Absorption spectra of TiN dimer NP incorporated Si absorber layer and Solar irradiance spectra.	58
4.9	Percentage of power absorbed for (a) Ag, (b) Au, (c) Al, (d) TiN NP incorporated Si absorber layer for solar cells.	59
4.10	Absorption enhancement, g for the dimer of plasmonic spherical NPs for r = (a) 15 nm, (b) 25 nm, and (c) 30 nm. (d) The g for TiN NPs with different radii.....	60
4.11	(a) f_{sub} , (b) Q_T , (c) Q_{sc} , and (d) Q_{ab} as a function of wavelength for TiN dimer shaped NP with varying the polarization angle of the source from $\theta=15^\circ$ to 90°	61
4.12	Color map showing the distribution of E-field in xy plane at Z=0 for TiN dimer NP placed on top of a 30 nm thin Si_3N_4 on a Si Substrate with varying the polarization angle of the source from $\theta = 15^\circ$ to 90°	62
4.13	Color map showing the distribution of $ E $ in the yz plane at x=0 for TiN dimer NP placed on top of a 30 nm thin Si_3N_4 on a Si Substrate with varying the polarization angle of the source from $\theta = 15^\circ$ to 90°	63
4.14	(a) f_{sub} , (b) Q_T , (c) Q_{sc} , and (d) Q_{ab} as a function of wavelength for TiN dimer spherical NP with distance, d = 0, 20, 70, and 100 nm placed on top of a 30 nm Si_3N_4 on a Si substrate.	64
4.15	(a) f_{sub} , (b) Q_T , (c) Q_{sc} , and (d) Q_{ab} as a function of wavelength for TiN dimer spherical NP for 30° source polarization angle of the source with distance, d = 0, 20, 70, and 100 nm placed on top of a 30 nm Si_3N_4 on a Si substrate.....	65

4.16	(a) f_{sub} , (b) Q_T , (c) Q_{sc} , and (d) Q_{ab} as a function of wavelength for dimer spherical TiN NPs with radius, $r = 50, 70, 100,$ and 120 nm placed on top of a 30 nm Si_3N_4 on a Si substrate.....	65
5.1	Visual representations of (a) a bowtie-shaped TiN nanoparticle, (b) a bowtie-shaped TiN nanoparticle with a distance of 60 nm between the two triangular plates, and (c) a triangle-shaped TiN nanoparticle. These nanoparticles were placed on top of a thin Si_3N_4 layer on a Si substrate. (d) A cross-section of the simulation set up. Light from the source was incident on the particle in the z -direction.....	67
5.2	(a) f_{sub} , (b) Q_T , (c) Q_{sc} , and (d) Q_{ab} as a function of wavelength for Tin bowtie shaped nanoplate with thickness, $h = 50, 100, 150, 200,$ and 250 nm placed on top of a 10 nm Si_3N_4 on a Si substrate.....	69
5.3	Color map showing the xy spatial distribution of $ E $ for TiN bowtie-shaped nanoplate placed on top of a 10 nm thin Si_3N_4 on a Si substrate with varying thickness, $h =$ (a) $50,$ (b) $75,$ (c) $100,$ (d) $150,$ (e) $200,$ and (f) 250 nm.....	70
5.4	Color map showing the zx spatial distribution of $ E $ for TiN bowtie-shaped nanoplate placed on top of a 10 nm thin Si_3N_4 on a Si substrate with varying thickness, $h =$ (a) $50,$ (b) $75,$ (c) $100,$ (d) $150,$ (e) $200,$ and (f) 250 nm.....	71
5.5	Color map showing the yz spatial distribution of $ E $ for TiN bowtie-shaped nanoplate placed on top of a 10 nm thin Si_3N_4 on a Si substrate with varying thickness, h of (a) $50,$ (b) $75,$ (c) $100,$ (d) $150,$ (e) $200,$ and (f) 250 nm.....	72
5.6	(a) f_{sub} , (b) Q_T , (c) Q_{sc} and (d) Q_{ab} for various polarization angle of the source from $\theta=15^\circ$ to 90°	73
5.7	Absorbed power spectra for various polarization angle of the source from $\theta=15^\circ$ to 90°	74
5.8	Color map showing the xy distribution of $ E $ for TiN bowtie-shaped nanoplate placed on top of a 10 nm thin Si_3N_4 on a Si substrate with varying the polarization angle of the source from $\theta=15^\circ$ to 90°	75
5.9	Color map showing the zx spatial distribution of $ E $ for TiN bowtie-shaped nanoplate placed on top of a 10 nm thin Si_3N_4 on a Si substrate with varying the polarization angle of the source from $\theta=15^\circ$ to 90°	75
5.10	Color map showing the zx distribution of $ E $ for a cross-section at $y=100$ nm for TiN bowtie-shaped nanoplate placed on top of a 10 nm thin Si_3N_4 on a Si substrate with varying θ from 15° to 90°	76
5.11	Color map showing the yz distribution of $ E $ at $x=0$ nm for TiN bowtie-shaped nanoplate placed on top of a 10 nm thin Si_3N_4 on a Si substrate with varying θ from 15° to 90°	77

5.12	(a) f_{sub} , (b) Q_T , (c) Q_{sc} , and (d) Q_{ab} as a function of wavelength for Tin bowtie-shaped nanoplate with varying distance, d between the triangles. $d=10, 30, 50, 60,$ and 70 nm placed on top of a 30 nm Si_3N_4 on a Si substrate.	78
5.13	Average (a) f_{sub} , (b) Q_T , (c) Q_{sc} , and (d) Q_{ab} for TiN bowtie-shaped nanoplate for various thickness of dielectric material, Si_3N_4 on a Si substrate.	79
5.15	(a) f_{sub} , (b) Q_T , (c) Q_{sc} , and (d) Q_{ab} as a function of wavelength for TiN bow tie-shaped nanoparticle placed on top of a 10 nm thin Si_3N_4 on a Si substrate.....	80
5.14	(a) f_{sub} , (b) Q_T , (c) Q_{sc} , and (d) Q_{ab} as a function of wavelength for TiN bowtie-shaped nanoparticles placed on top of a 30 thin Si_3N_4 on a Si substrate.	81
5.16	Average (a) f_{sub} , (b) Q_T , (c) Q_{sc} , and (d) Q_{ab} as a function of wavelength for TiN triangle shaped nanoparticle varying the thickness of dielectric material, Si_3N_4 on a Si substrate.	81
6.1	(a) Illustration of different shapes TiN nanoparticle on a 10 nm thin Si_3N_4 under-layer on kesterite solar cell.....	83
6.2	(a) Current density-voltage characteristic and (b) Power-voltage of bowtie-shaped TiN NP on CZTS solar cells. (c) Comparative power-voltage characteristics curves for the bare, spherical, dimer of spherical, and bowtie-shaped NP incorporated CZTS solar cells.	86
6.3	(a) Current density-voltage and (b) power-voltage characteristic of monomer shaped TiN NP on CZTS cell.	86
6.4	(a) Current density-voltage and (b) power-voltage characteristic of dimer shaped TiN NP on CZTS substrate cells.	87
6.5	Absorption data versus wavelength λ for CZTS absorber material.....	88
6.6	(a) Refractive index and (b) extinction co-efficient of CZTS.....	89
6.7	f_{sub} as a function of wavelength for (a) TiN bowtie NPs varying the thickness, $h = 100, 150,$ and 200 nm, (b) TiN monomer-spherical NPs with radius, $r = 100, 150,$ and 200 nm placed on top of a 10 nm Si_3N_4 on a Si and CZTS cells.....	90
6.8	Percentage of power absorbed in each layer of TiN nanosphere on (a) CZTS, (b) Si, substrate. Percentage of power absorbed in each layer of TiN bowtie-shaped nanoplate on (a) CZTS, (b) Si substrate.	91
6.9	Absorption enhancement, g for bowtie-shaped TiN plasmonic nanoplates with $h = 15, 30, 70$ and 100 nm.	92
6.10	(a) (a) Reflection, transmission, and absorption of TiN bowtie-shaped nanoplates based CZTS solar cell. (b) Absorption spectra of bowtie-shaped TiN NP incorporated CZTS absorber layer and Solar irradiance spectra.	93

6.11	f_{sub} for TiN bowtie-shaped nanoplates varying the polarization angle of the source for from $\theta=15^\circ$ to 90° on a 10 nm Si_3N_4 on top of (a) Si and (b) CZTS solar cells.....	94
6.12	(a) Current density-voltage and (b) power-voltage characteristics of bowtie-shaped TiN NP on CZTS solar cells for various θ . The θ was varied from 15° to 90°	94
7.1	Different losses in a solar cell, (a) schematic diagram of a solar cell and (b) band diagram of a solar cell.....	96
7.2	(a) Illustration of different shapes TiN nanoparticle on a 10 nm thin Si_3N_4 under-layer on kesterite solar cell incorporated with upconverter solar cell. (b) An illustration of the concept of a UC-enhanced device harvesting sub-bandgap photons via a UC layer located on a kesterite solar cell. (c) Absorption spectra of TiN dimer NP incorporated kesterite absorber layer in the air-mass 1.5 global (AM 1.5G) solar spectra, indicating the wavelength by a UC layer.....	97
7.3	Upconversion process; two photons with energy $1/2 E_g \leq h\nu \leq E_g$. generate a photon with energy $h\nu \geq E_g$, where E_g denotes the band gap of the material and (b) A schematic diagram of a solar cell with UP converter. (c) Down conversion process; one photon with energy $h\nu \geq 2E_g$ yields two photons with $h\nu \geq E_g$ and (d) A schematic diagram of a solar cell with down converter.....	98
7.4	Energy scheme for upconversion in organic molecules. The singlet state of the sensitizer is excited and relaxes through a fast intersystem crossing to the triplet state of the sensitizer	100
7.5	A schematic illustration of the system for upconversion.....	101

7.6 Absorption power for bowtie-shaped TiN plasmonic nanoplates with upconverter layer tandem solar cell for different absorber materials. The black line represented the absorbed power for the tandem cells with kesterite in the top layer, a YAG upconverter layer, and Si in the bottom layer. The green line represented the absorbed power for the tandem cells with kesterite in the top layer, a YAG upconverter layer, and kesterite in the bottom layer. The pink line represented the absorbed power for the kesterite in the top layer with a YAG upconverter layer. The blue line represented the absorbed power for the tandem cells with kesterite in the top layer, a YAG upconverter layer, and kesterite in the bottom layer. The wine color line represented the absorbed power for the tandem cells with kesterite in the top layer, a YAG upconverter layer, and Ge in the bottom layer. The cyan color line represented the absorbed power for the tandem cells with kesterite in the top layer, a YAG upconverter layer, and InAs in the bottom layer..... 103

7.7 Absorption enhancement, g for bowtie-shaped TiN plasmonic nanoplates with upconverter layer tandem solar cell for different absorber materials. 104

List of Tables

5.1	Dependency of the cross-sections on bowtie thickness	70
5.2	Effect of polarization of incident light on cross-sections	74
5.3	Cross-section comparison for different shapes of the nanoparticles	80
6.1	Comparison of electrical Properties of various shape and size of kesterite solar cells	87
6.2	Electrical parameters of materials used in simulation	89
6.3	Electrical parameters used in simulation in the proposed solar cell	90
6.4	Light absorption enhancement on 100 nm bowtie-shaped NPs incorporated cells	93
7.1	Electrical performance of the nanoparticle and upconversion layer incorporated kesterite solar cell	102

Acknowledgement

All praise goes to the Almighty for giving us the patience and drive required to complete our thesis and finish the dissertation in due time. We also thank my family members, without whose support and encouragement, it would be impossible to carry on with my study smoothly.

I would like to express my sincere gratitude to my supervisor, Dr. Ahmed Zubair, Associate Professor, Department of Electrical and Electronic Engineering, Bangladesh University of Engineering and Technology (BUET), for his continuous support throughout the course of my research. His patient hearing of my ideas, critical analysis of my observations, and detection of flaws in my thinking and writing have been invaluable. I also want to thank him for affording me so much time for me to explore the areas of my research and new ideas and improve the writing of this dissertation. I feel immensely grateful to him for his motivation, enthusiasm, persistence, patience, generosity, and above all, belief in my abilities which made this work possible.

I would also like to express my appreciation to the members of my thesis committee Dr. Md. Aynal Haque, Dr. Md. Shafiqul Islam, Dr. Apratim Roy, and Dr. Mohammad Ryyan Khan, for taking the time to evaluate my work and provide insightful suggestions.

Lastly, I am grateful to almighty Allah for keeping me safe and sound and providing me with the strength to finish the thesis.

Abstract

This thesis presents the design, optimization, and performance analysis of titanium nitride nanoparticle embedded and upconverter incorporated kesterite solar cells. We systematically studied scattering cross-section and absorption enhancement by nanoparticles (NPs) of alternative material, TiN. At first, we performed a comparative performance analysis of TiN with noble metals, Au and Ag to establish its functionality as a plasmonic material. Afterward, we explored different-shaped plasmonic nanosystems, which consisted of dimer, monomer, and bowtie-shaped NPs. Moreover, we determined the total scattering cross-section, the fraction of light scattered into the substrate, light scatter into the substrate, the absorption cross-section, and spatial mapping of the electric field in the plasmonic nanosystems. Additionally, we studied the polarization-sensitive performance varying the light polarization angle. We conducted a shape-dependent comparative analysis of the nanoparticles. We examined the impact of the dielectric coating of the nanoparticles. We considered monomer spherical, dimer spherical, and bowtie-shaped TiN NPs on CZTS thin film-based solar cells and found that bowtie-shaped had the best electrical and optical performance. In the solar cell, the nanoparticle with the best performance was utilized. Instead of using silicon cells, kesterite solar cells are utilized to increase solar cell efficiency. Our suggested solar cell concept features tandem solar, and an upconverter layer is inserted to increase light trapping efficiency. We conducted comparison analyses with the metals Ag, Au, and Al to ascertain the performance of TiN as a plasmonic material. TiN NP had the higher absorption cross-section, Q_{ab} and fraction of light scattered into the substrate, f_{sub} values greater than those of Ag, Au, and Al. TiN dimer exhibited better absorption enhancement, g for the whole spectral range than Ag, Au, and Al dimers. Utilizing TiN-based plasmonic nanostructures, we demonstrated that the f_{sub} can be tuned by varying the shape, size, thickness, dielectric thickness, and source angle. Moreover, total scattering in the wavelength range of the solar spectrum was modulated. The scattering performance improved for the thicker dielectric layer. Among the nanostructures, the bowtie shape showed a better light absorption cross-section. Solar cells based on the kesterite mineral structure and its alloys stand out from other thin-film solar cells due to their earth-abundance and non-toxicity. Incorporating plasmonic nanoparticles with kesterite opens a promising path of light trapping efficiency. The main losses in solar cells result from the incomplete utilization of the solar spectrum. The otherwise-unused sub-bandgap photons can be utilized by adding an upconverting layer on a solar cell. For 100 nm thickness, g was greater than 1 for the whole spectral range, and the maximum value was ~ 1.2 . The optimal thick bowtie-shaped NP had the highest efficiency, η at 26.27% and had the open circuit voltage $V_{oc} = 0.58$ V, and short circuit current density, $J_{sc} = 54.01$ mA/cm². The absorbed power for bowtie-shaped TiN NP incorporation enhanced the average absorption from $\sim 61\%$ to $\sim 88\%$ for the kesterite cell. The incorporation of upconverter layer YAG increased the solar cell efficiency up to $\sim 28.90\%$

Chapter 1

Introduction

There has been significant research for increasing the efficiency of solar cells using light trapping by scattering from nanoparticles [1,2] and using up-down converters [3,4] recently. Thin film photovoltaic (PV) technologies open an economically promising and flexible opportunity to harness solar energy lowering cost as it is lightweight, compatible with both flexible and rigid substrates, and tunable light spectrum response [5,6]. Chalcogenides CdTe and Cu(In,Ga)(S,Se)₂ (CIGS) materials-based solar cells have shown efficiencies above 20%, long-term stability, and have been commercialized for over a decade [7, 8]. Their market share has stagnated because of the rapid decline in the cost of Si-based PV as well as the use of rare materials (In, Ga) [9,10]. These either limit cost savings or raise environmental concerns, thus detracting from the product's value compared to Si-based PV. Therefore, sustainable terawatt-level deployment of photovoltaics will eventually require the design and development of compounds. Kesterite is in the adamantine family of chalcogenides, as its crystal structure is similar to CIGS but free from toxic components. This cross-substitution change brings expansive adaptability in component determination, enabling the incorporation of earth-abundant constituents. Kesterite Cu₂ZnSn(S, Se)₄ can be a promising candidate for high-efficiency solar cells because of its non-toxic components [11].

Plasmonic materials can support electrons or plasmons over a broad spectrum from infrared to ultraviolet solar light. Until recently, researchers were confined to noble metals like Ag and Au as plasmonic material. Ag and Au are commonly used plasmonic metals and optical metamaterial due to their low resistive losses or high DC conductivity [12–15]. However, there is confinement for plasmonic metals while an electron in the valence band in a metal absorbs a photon to jump to the Fermi surface or while an electron close to the Fermi surface absorbs a photon to fill the subsequent unoccupied conduction band inflicting an excessive loss in conventional plasmonic materials. Additionally, the optical properties of metals cannot be tuned or adjusted easily and are not cost-effective. Because of these shortcomings of conventional plasmonic materials, researchers have been searching for alternatives [16].

Titanium Nitride (TiN) can overcome one or more of the abovementioned drawbacks [17] as they show metallic properties within visible and longer wavelengths [18, 19].

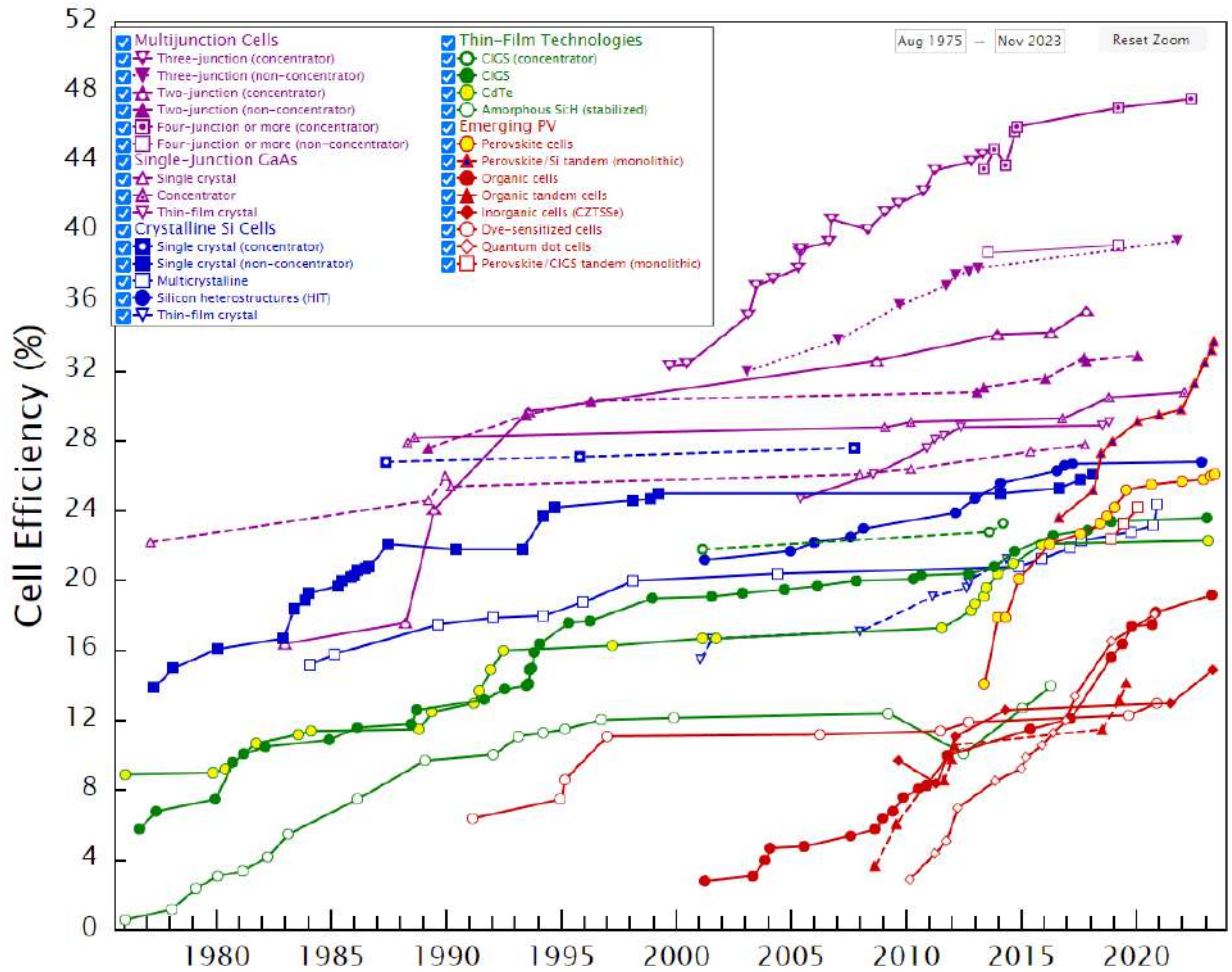


Figure 1.1: A chart of the highest confirmed conversion efficiencies for research cell for a range of photovoltaic technologies plotted from 1976 to the present.

[20]

The thermalization of high-energy photons (1150 nm) and transmission of low-energy photons of the solar spectrum has an adverse effect on the conversion efficiency of solar cells. These problems can be overcome by modifying the solar spectrum through up-conversion mechanisms. Upconverter materials can enhance the upconversion efficiency [21, 22]. For selecting suitable nanoparticle geometry with appropriate plasmonic material in kesterite-based solar cells to enhance path length and, consequently, to improve absorption, a comprehensive study of kesterite-based plasmonic solar cells is essential. Moreover, the design and optimization of the upconversion layer for the kesterite solar cell will benefit high-efficiency solar cells.

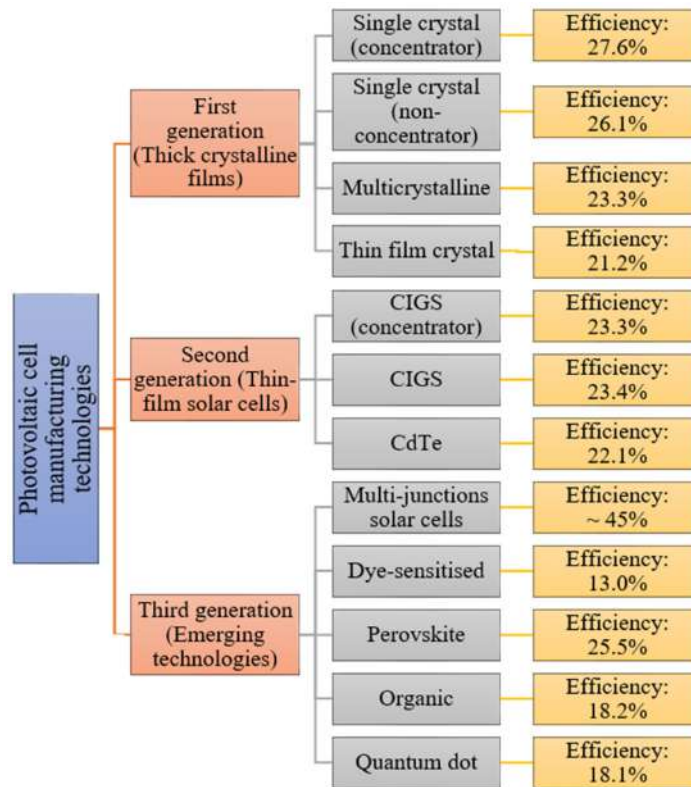


Figure 1.2: Photovoltaic cell generations.

1.1 Evolution of Solar Cells

Alexandre Edmond Becquerel was the first to observe the photovoltaic effect via an electrode in a conductive solution exposed to light in 1839; since then, the evolution of solar cells has become a never-ending process as can be seen in Figure 1.1. It is captivating to look at the history of PV cells because there are lessons to be learned that can guide the future development of PV cells. In 1954 Bell Lab announced Silicon solar cell [23] with the 8% efficiency. This was the foundation for the development of a variety of markets for PV. Several novel technologies were demonstrated, such as single crystal AlGaAs/GaAs solar cells with a 20 % efficiency that were also more radiation resistant than silicon solar cells. The following attempt used silicon powder in monolithic structures, which resulted in amorphous silicon. Tandem solar cells, plasmonic solar cells, and quantum dot solar cells are examples of solar cell types that deviate from the single crystal theory foundation. Solar cells have significantly improved efficiency, commercialization, and utility in the energy sector over the past 50 years [24]. The multifunction solar cells have the highest efficiency as the light trapping occurs in two or more absorber layers [20]. Emerging solar cells are becoming famous as cost-effective and sustainable; however, their efficiency is still lagging. The emerging solar cell requires more research. The solar cell evolution is mainly classified into three generations presented in Figure 1.2. These generations are categorized based on growth and significantly different methodologies, materials, and technologies.

1.1.1 First Generation Solar Cells

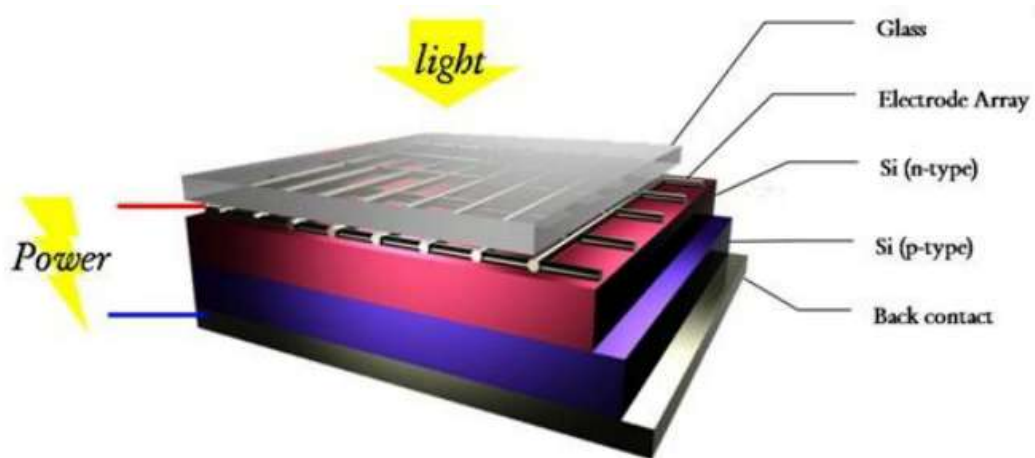


Figure 1.3: First generation solar cell.
[25]

First-generation photovoltaic is the oldest commercially available technology and is mature in technology and manufacturing processes. Typically, they are made of either crystalline silicon (c-Si) or GaAs wafers presented in Figure 1.3. In contrast to silicon, GaAs is a direct bandgap semiconductor material with a bandgap of 1.43 eV at 300 K and impressive optical characteristics. Contrarily, silicon has an indirect bandgap with a bandgap of around 1.12 eV at 300 K. GaAs solar cells outperform crystalline silicon solar cells in terms of performance [26].

However, GaAs has not yet been chosen for commercial solar electricity generation purposes as the GaAs solar cell manufacturing process is much more expensive. Silicon solar cells require relatively thick silicon wafers to absorb the incident sunlight sufficiently. Materials for first-generation solar cells are mostly based on silicon wafer technology [27]. It uses monocrystalline (single crystal) silicon and some polycrystalline solar cells. Due to area-related costs, which make up a significant portion of system costs, the efficiency of a solar cell is crucial. Therefore, efficiency improvements were the main focus in both laboratories and manufacturing facilities. Currently, $\sim 26.7\%$ is the maximum experimental efficiency for monocrystalline silicon. These solar cells' main drawbacks are that they are expensive and unsuited for flexible electronics applications.

1.1.2 Second Generation Solar Cells

The most efficient thin film solar cells are based on Cu(In,Ga)(S,Se)_2 , (CIGSSe) and CdTe compounds, known as second generation polycrystalline thin films [28]. The second generation thin film solar cell is presented in Figure 1.4. The current challenge for terrestrial

applications for the production of solar cells are cost efficiency, high efficiency and environmentally friendly manufacturing processes [29]. The second-generation thin-film solar cells open an easy path for lowering the cost/watt of devices. The relative quantity of the compounds' component parts, their application in important sectors, and the technology employed in producing solar cells all affect the cost per peak watt. The key difficulty with these materials is lowering the cost per watt of solar energy conversion. Still, they are actually formed by expensive and scanty elements in the earth's crust, such as In, Ga, Te and there present toxicity issues like Cd [7].

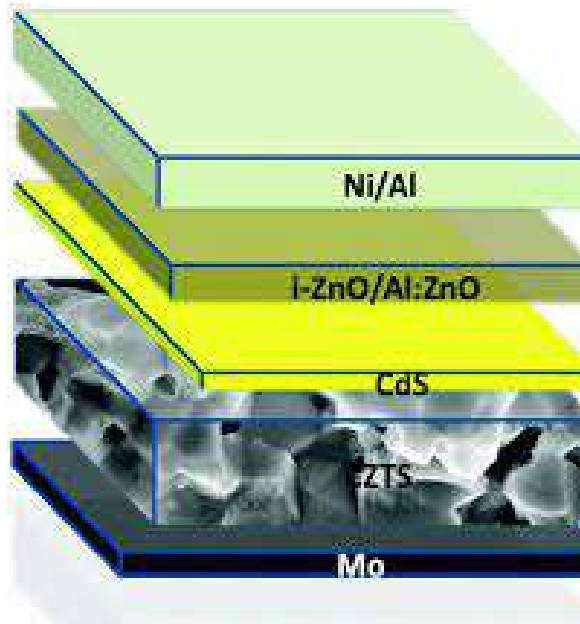


Figure 1.4: Second generation thin film CZTS solar cell.
[30]

New materials have been suggested as alternatives to the main second-generation solar cells; they offer characteristics useful for photovoltaic applications and are made of relatively plentiful and harmless components. Semiconductor compounds with kesterite structure ($\text{Cu}_2\text{ZnSn}(\text{S}_x\text{Se}_{1-x})_4$, $\text{Cu}_2\text{ZnSnS}_4$, $\text{Cu}_2\text{ZnSnSe}_4$) and others like In_2S_3 , all of them Cadmium-free have been proposed as new candidates for thin film solar cells [5]. There has been the development of technological steps for processing solar cells based on kesterite compounds and the deposition method for In_2S_3 buffer layer as alternatives to CdTe and CdS films.

1.1.3 Third Generation Solar Cells

The third generation solar cells are based on newer technology which comprises nanocrystalline solar cells, organic solar cells [31], perovskite solar cells [32], quantum dot solar cells [33], plasmonic solar cells [34] polymer-based solar cells [35], and various tandem

cells fall into this category. Figure 1.5 presents the third generation solar cell based on perovskite plasmonic solar cell. This structure, which is still in its early stages of development, has great potential as a technology. Third-generation solar cells have significant potential for producing solar electricity on a big scale because they are solution processable. They are affordable, and each solar cell family is seen to have a high potential for widespread adoption using roll-to-roll (R2R) manufacturing. [36].

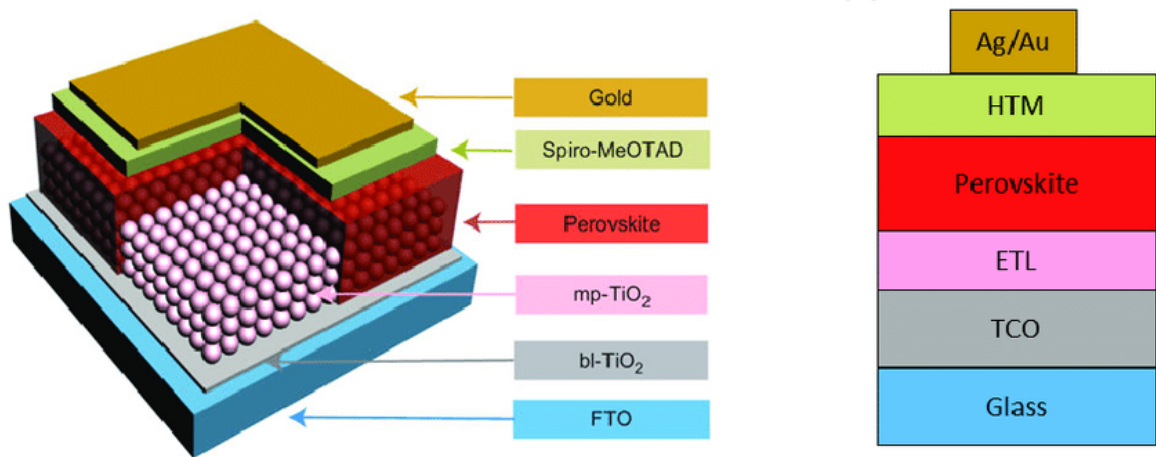


Figure 1.5: Third generation plasmonic perovskite solar-cell configurations. [37]

1.2 Kesterite Solar Cells

Thin film photovoltaic technologies open an economically promising and flexible opportunity to harness solar energy [5, 6]. Kesterite $\text{Cu}_2\text{ZnSn}(\text{S},\text{Se})_4$ (CZTSSe) materials have emerged as the most successful thin film among Se, SnS, Cu_xS , FeS_2 , Cu_2SnS_3 , Cu_2O , and $\text{Sb}_2(\text{S},\text{Se})_3$ due to non/low-toxic and earth-abundant constituents [7, 38]. Kesterite is a member of the chalcogenide family, but it was created by substituting two group III cations with one group II (Zn) and one group IV (Sn) cation. This allowed the integration of the plentiful earthly elements shown in Figure 1.6. Kesterite-based materials inherit the benefits of the high absorption coefficient (above 10^4 cm^{-1}) and tunable band gap energy between optimum zones from 1.0 to 1.5 eV from CIGS since they share a comparable lattice crystal and energy band structure. The chance to aid in the early development of this affordable PV technology has been made available by Kesterite [39]. Kesterite solar cells have reached 12.6% efficiency, which is a level that is competitive on the market [40].

Despite the promise of reducing the cost per watt of solar energy conversion, thin-film, CIGS chalcopyrite, and CdTe photovoltaic technologies approaches rely on elements that are either costly or rare in the earth's crust (e.g., In, Ga, Te) or that present toxicity issues (e.g., Cd). While maintaining the advantages of the chalcopyrite and CdTe materials, less

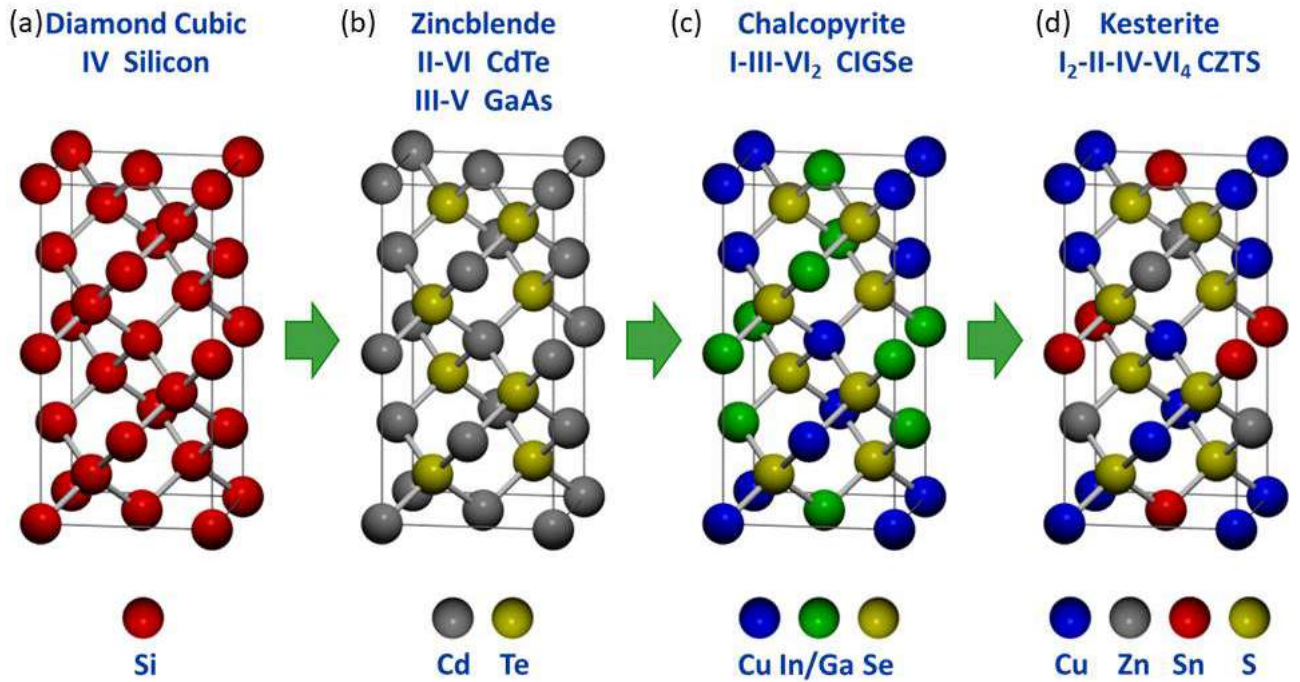


Figure 1.6: Crystal Structures of (a) Si, (b) CdTe (c) CIGSe and (d) CZTS materials. [11]

toxic and lower-cost elements are desirable to develop a compatible photovoltaic technology. Kesterite-based $\text{Cu}_2\text{ZnSn}(\text{S},\text{Se})_4$ (CZTSSe) thin-film solar cells have replaced indium and gallium from CIGSSe by the available elements zinc and tin, providing appropriate direct band gap tunability over the solar spectrum, high device performance and compatibility with low-cost manufacturing [41]. As vacuum-deposited devices allowed for optimization within the compositional phase space and produced selenium-free CZTS devices with efficiencies as high as 6.8%, the CZTS research has demonstrated promising potentialities. More recently, a liquid-based approach has been described that allowed for the deposition of CZTSSe devices with a power conversion efficiency of 9.7%. The absorber and its surrounding interfaces must be enhanced if kesterite solar cells are to perform even better. A greater comprehension of the loss mechanism in kesterite solar cells has led to the enumeration of numerous workable solutions that are constantly looking for new optimizations [42, 43]. Kesterite can develop bespoke processes and structures, revising the research routes on its unique properties.

1.3 Plasmonic Solar Cells

The deposition of metal nanoparticles on the top surface of the solar cell is a popular design. The light is scattered widely when it strikes the surface plasmon resonance of these metal nanoparticles. As a result, the solar cell can absorb more light since light can move along the

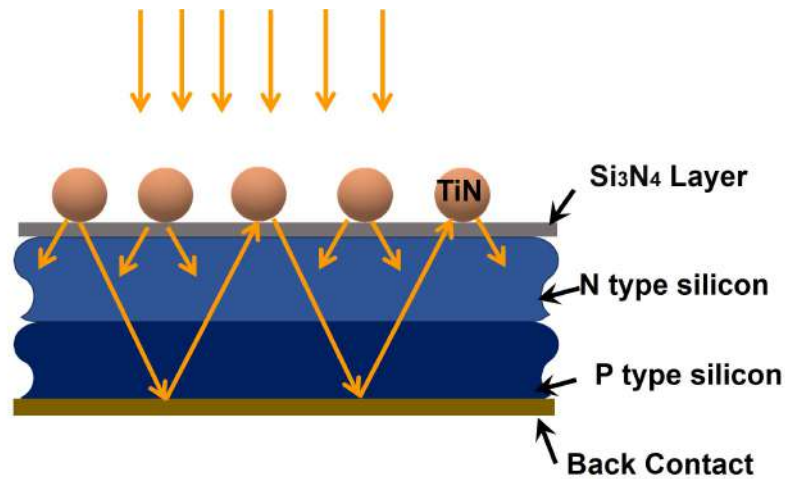


Figure 1.7: Plasmonic solar cell.

solar cell and bounce off the substrate and nanoparticles. The optical absorption of semiconductors will be aided by the concentrated near-field intensity caused by the localized surface plasmon of the metal nanoparticles. Recently, it has been discovered that the plasmonic asymmetric modes of nanoparticles favor the broadband optical absorption and electrical characteristics of solar cells. The simultaneous plasmon-optical and plasmon-electrical effects of nanoparticles show a potential aspect of nanoparticle plasmon. An electron and hole are split apart when a photon is activated in the solar cell's substrate. Due to their opposite charges, they will desire to unite once more once the electrons and holes are split apart. The electrons can be employed as a current for an external circuit if collected before this occurs. There is always a trade-off when determining the thickness of a solar cell between reducing this recombination (thinner layers) and absorbing more photons (thicker layers). As shown in Figure 1.7, by scattering light with the help of metal nanoparticles activated at their localized surface plasmon resonance, plasmonic-enhanced cells increase absorption. Plasmonic core-shell nanoparticles can help poor Si solar cell absorption in the near-infrared region; the maximum optical path length enhancement can be as high as 3133, and the percentage of light scattered into the substrate can be reduced [44]. Incoming light at the plasmon resonance frequency causes electron oscillations at the surface of the nanoparticles, which is a property that direct plasmonic solar cells take advantage of. A conductive layer can then catch the oscillating electrons, creating an electrical current. The bandgap of the conductive layer and the potential of the electrolyte in contact with the nanoparticles both affect the generated voltage.

The plasmonic light trapping mechanism is an excellent way of improving solar cell efficiency. One of the main challenges to the performance of the development of thin film solar cells is the creation of efficient light trapping methods [45–49]. Surface texturing, utilization of back reflectors, and various other approaches have been proposed for enhancing absorption in thin film solar cells [50,51]. Recently, plasmonics has been used for light trap-

ping employing metal nanoparticles [45]. Surface plasmons are collective oscillations of the free charges at the metal surface. Metals sustain surface plasmons, either localized in the metal nanoparticles or propagating in the case of planar metal surfaces. The surface plasmon resonance or plasmon propagation can be tuned by controlling the size and shape of the metallic nanostructures. Since the surface plasmon resonance of metal occurs primarily in the visible or the infrared wavelength region, they are of particular interest for photovoltaic applications [52,53].

Developing glass plastic materials based on thin film solar cells on the substrate could be an apace growing market [54]. However, these solar cells are affected by some common issues like low efficiency, intense degradation of recombination rate, and less stability [1, 55, 56]. The larger surface area can decrease the performance of these solar cells due to an increase in minority carrier recombination. In recent years, several solutions for more effective light concentration and trapping have been proposed to solve these issues, mainly using plasmonic structures made of thin metal films or nanoparticles [57]. They were quite successful at enhancing and redirecting the incident light beam. Plasmonic structures have diverse applications [34], especially in the field of photovoltaics [12,58,59] where many different technological approaches were proposed to explore plasmon excitation and light localization for highly efficient solar cells. Many studies were conducted illustrating the coupling of plasmons to optical emitters, plasmon focusing, and hybridized plasmonic modes in nanoscale metal shells [15, 60–62].

Introducing metallic nanoparticles (NPs) has created an alternative approach to improving absorption efficiency. Surface plasmon resonance (SPR) can significantly enhance electromagnetic (EM) waves by placing plasmonic structures in the active layer. This phenomenon ensures enhanced light absorption providing strong scattering between the intense plasmon field and the active layer [53, 63]. Localized surface plasmon resonances (LSPRs) generate light scattering by NPs. When the frequency of the optical photon matches the natural frequency of the collective vibration of conduction electrons in NPs, the LSPR occurs, producing sharp spectral absorption, scattering peaks, and strong near-field electromagnetic enhancement [64]. The enhancement of optical absorption of NPs is the foremost attribute of LSPR [65]. The LSPR phenomenon has been utilized to enhance light absorption and photocurrent in various solar cell configurations [66, 67]. The most significant improvement happens when the junction between the absorber and NPs is illuminated by polarized light. Sensitivity that results in near-infrared (NIR) sensing and plasmon hybridization can be achieved using complex structures. Due to the extension of the inside field to the outside environment, the NPs structure can overcome this limitation leading to a significant increase in the detection sensitivity. Plasmonic materials can support electrons or plasmons over a broad spectrum from infrared to ultraviolet solar light.

1.4 Upconverter Solar Cells

The conversion efficiency of solar cells is not very efficient as longer wavelengths cannot be utilized in light absorption. These problems can be overcome by modifying the solar spectrum through down-conversion (quantum cutting) and up-conversion mechanisms. In an upconversion process, photons with energies below the band gap of the solar cell are transformed into photons with higher energies.- [68, 69]. The efficiency of the solar cell is increased when these higher photons are reflected back to it and absorbed. Transmission or sub-bandgap losses refer to the inability of incident photons with energy below the threshold to contribute to the creation of electrons in the solar cell. By combining two or more photons with energies below the threshold energy into one photon with a useful energy, upconversion lowers these losses. It was assumed that the upconverter system under study was photon selective, meaning that photons of a given energy could only trigger one particular transition, and that the upconversion process involved two transitions of various energies. Additionally, it was shown that it is crucial for at least one non-radiative relaxation process to take place during the upconversion process sequence in order to reduce the likelihood of the reverse process sequence.

An upconverter (UC) is a material characterized in that the emitted photons have higher energy than the absorbed photons [70]. This so-called anti-Stokes emission can be achieved in particular ways. In second harmonic generation (SHG), a birefringent crystal converts a highly monochromatic and coherent laser from existent energies to higher energies. This process is very adept for high laser powers but inefficient for spectral conversion. An intermediate-stage upconverter is required to convert the infrared part of the solar spectrum. By absorbing two IR photons, a two-step excitation process raises the system from the ground state, through an intermediate state, to a high-energy state. Emission from the highly excited energy state follows this.

To increase the efficiency of the solar cell demonstrated, conversion materials such as Ln^{3+} ions doped glasses, glass-ceramics, and phosphor modify the incident solar spectrum presented in Figure 1.8 [72]. UC materials convert low-energy infrared photons to high-energy near-infrared or visible photons whose energies are slightly greater or equal to the energy gap of a Si solar cell. Upconversion-based solar cells represent a different type of infrared solar cell. The infrared portion of the sun's irradiation is really absorbed by a separate layer in these devices, not the active material, which is not its function. A multiphoton relaxation procedure is then used to transfer this energy in the light-absorbing range of the active material. According to theoretical modeling, using rare earth ions or plasmonic nanostructures to reduce the thermal losses of a single junction solar cell outside of its typical frequency range may be a promising way to get closer to the theoretically achievable efficiency limit of 85% for a general-purpose photovoltaic device.

Figure 1.8: Periodic table highlighting the Lanthanides.
[71]

Ytterbium ions and Erbium ions are frequently used in this method, which requires the excitation of Ytterbium at 980 nm and the emission of green and red light after energy transfer processes between Yb^{3+} and Er^{3+} . A very effective up converter, NaYF_4 doped with Yb^{3+} and Er^{3+} absorbs infrared photons with an efficiency of about 50% and emits visible light. The quantum dots release photons at a wavelength of about 1520 nm, which is resonant to the absorption of Er^{3+} . Upconverting nanoparticles have been also employed to enhance the absorption of dye-sensitized solar cells. The two-step energy transfer is presented in Figure 1.9. The ${}^2F_{7/2}$ to ${}^2F_{5/2}$ transition has a relatively strong oscillator and Er^{3+} has a state with a similar energy (${}^4I_{11/2}$), which is filled by energy transfer from Yb^{3+} , the Yb^{3+} ion is an ideal sensitizer for Er^{3+} . The population of Yb^{3+} in its first excited state (${}^4I_{11/2}$) is thus precisely proportional to the strength of the entering light. Energy transfer from the first excited state (${}^4I_{11/2}$) to the second excited state (${}^4F_{7/2}$) occurs when upconversion is the primary route. Following a few minor energy-relaxation steps, emission from the ${}^4S_{3/2}$, ${}^2H_{11/2}$ (green), and ${}^4F_{9/2}$ (red) states is seen. Transferring energy from the ${}^4I_{13/2}$ state to the ${}^4F_{9/2}$ is possible.

1.5 Objectives of the Thesis

The main objectives of this work are to explore the light trapping efficiency using plasmon nanoparticle-based photovoltaics varying their shapes, sizes, and dielectric thickness. To establish the relevance of alternative plasmonic materials the cross-section properties and absorption enhancement for different materials with TiN are compared. This work aims to develop a comprehensive study of kesterite-based plasmonic solar cells and design and

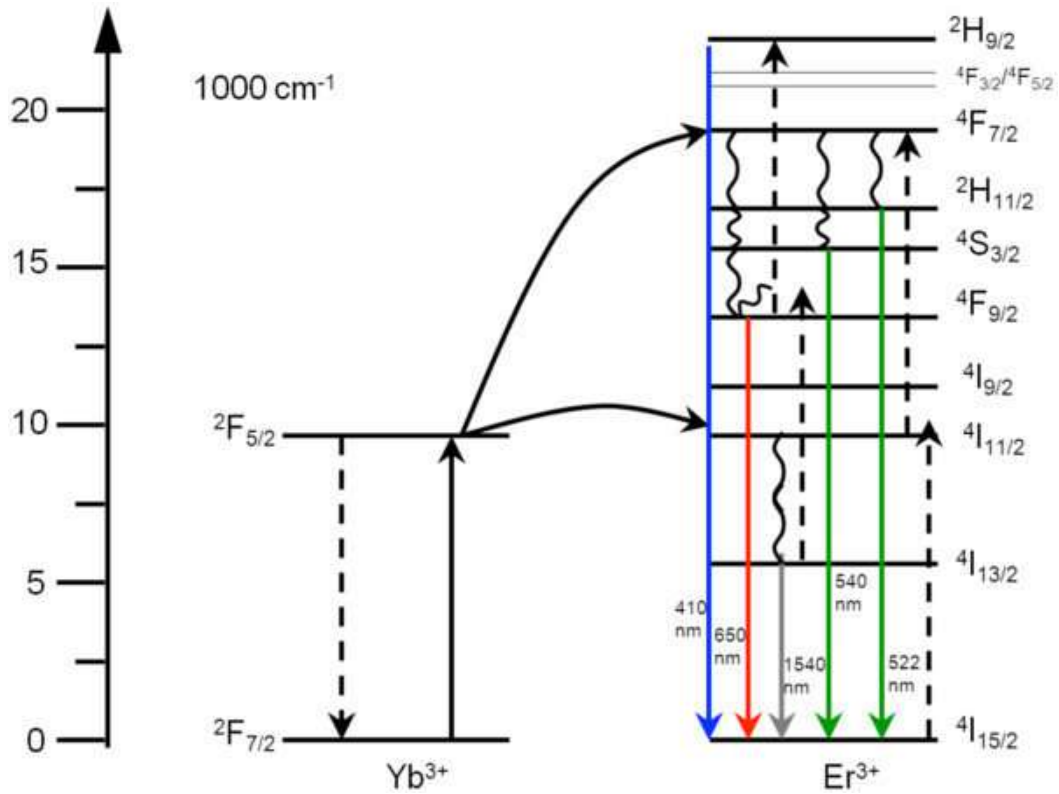


Figure 1.9: Schematics of the energy levels involved in the upconverting processes occurring in the materials (Yb^{3+} and Er^{3+}).

[73]

optimize the upconversion layer for the kesterite solar cell for high-efficiency solar cells. The specific objectives of this work are recapitulated here:

- To evaluate the prospect of alternative plasmonic nanoparticles based on titanium nitride (TiN) for higher efficiency of solar cells by replacing noble plasmonic metals such as gold and silver.
- To optimize light trapping absorbing layers by varying the thickness, and polarization angle of the source, and varying the shapes and thickness of the dielectric of the nanoparticle.
- To design and analyze TiN nanoparticle embedded kesterite solar cells using thin film $\text{Cu}_2\text{ZnSnS}_4$ (CZTS) absorber layer and analyze their performances.
- To design a solar cell model adding an upconversion layer with thin film and plasmonic for better tunability and compare the performances by varying different parameters of the model.

- To evaluate the tandem solar cell consisting of TiN plasmonic nanoparticle embedded and upconversion layer incorporated CZTS absorber layers.

1.6 Thesis Overview

This thesis is divided into eight chapters.

Chapter 1 starts with a general introduction and delineates the motivation behind the thesis is followed by the historical background of solar cells, the emergence of kesterite and plasmonics, and design challenges of plasmonic-based solar cells, and the objectives of this work.

Chapter 2 briefly overviews localized surface plasmon and light scattering and briefly describes some relevant theories that explain plasmonic light trapping and alternative plasmonic NPs. It also covers the basic key concepts of solar cells and their operation and introduces the parameters for quantifying results. A brief review of the optical model and electrical model used in the study are also presented in this section.

Chapter 3 details monomer-shaped plasmonic nanoparticles, the design, numerical techniques, and the simulation methodology used to obtain the scattering cross-section, absorption enhancement, E-field and far-field result. The discussion of simulated results for spherical NPs is also highlighted in Chapter 3.

Chapter 4 provides the details of spherical dimer plasmonic nanoparticles, the design, numerical techniques, and the simulation methodology used to obtain the comparative results of different parameters. The discussion of simulated results for dimer NPs is also highlighted in Chapter 4.

Chapter 5 provides the details of bowtie-shaped plasmonic nanoparticles, the design, numerical techniques, and the simulation methodology used to obtain the performance result. The discussion of simulated results for bowtie-shaped NPs is also highlighted in Chapter 5.

Chapter 6 studies current density-voltage ($J - V$) and power-voltage ($P - V$) characteristic curves and absorption enhancement of CZTS substrate for different shapes and sizes by incorporating TiN NPs. A comparative analysis has been performed among monomer, sphere, and bowtie-shaped NPs. The optimized plasmonic shape has been incorporated on the kesterite cell and analyzed.

Chapter 7 provides the idea of the upconversion and downconversion process. Afterward, an optimized solar cell was modeled, which was composed of alternative plasmonic material titanium nitride (TiN) based nanoparticle embedded on a semi-infinite crystalline CZTS

solar cell and cascaded an up-converter layer added CZTS solar cell has been proposed. The efficiency and compared performance of solar cell absorption efficiency with and without plasmonic, CZTS film, and upconverter (UC) layer incorporated cells has been illustrated.

Chapter 8 contains the concluding remarks and suggestions for future works.

Chapter 2

Plasmonic Light Trapping and Solar Cell Simulation

2.1 Localized Surface Plasmon Resonance

Localized surface plasmons are electromagnetic field-coupled, non-propagating excitations of the conduction electrons in metallic nanostructures. When a tiny, sub-wavelength conductive nanoparticle scatters in an oscillating electromagnetic field, modes inevitably develop. The driven electrons are effectively restored by the particle's curved surface, which allows for the emergence of a resonance and subsequent field amplification both inside the particle and in the vicinity of it. The brief localized plasmon resonance or localized surface plasmon is another name for this resonance. Another effect of the curved surface is that, in contrast to propagating SPPs, where phase-matching procedures must be used, plasmon resonances can be produced by direct light illumination presented in Figure 2.1.

To arrive at the resonance condition, the interaction of metal nanoparticles with an electromagnetic wave before looking into the physics of localized surface plasmons are explored. The consequences of interactions between particles in ensembles are discussed along with investigations of plasmon resonances in particles of various sizes and shapes. In addition to solid particles that sustain localized plasmons, other significant nanostructures include dielectric inclusions in metal bodies, surfaces, and nanoshells. The resonance for gold and silver nanoparticles is in the visible portion of the electromagnetic spectrum. The brilliant colors that particles display in transmitted and reflected light due to resonantly enhanced absorption and scattering are a noticeable side effect of this. This result has been used for centuries, such as for coloring glass for windows or decorative cups.

The oscillating electromagnetic field of the light leads to collective oscillations when light is incident on a metal nanoparticle. Effects of conduction electrons (plasmon excitation)

lead to resonant behavior due to continuous polarization effects and restoring forces. Light is most efficiently scattered at the nanoparticle in the wavelength region where resonance occurs simultaneously enhancing the parasitic absorption in the nanoparticle [74]. The favorable feature is that it is characterized by the ability to scatter light in large angles outside the specular direction, in the ‘forbidden zones’. Light is confined in the high refractive index layer with a higher refractive index than the neighboring media [75, 76]; this can preferentially be the absorber layer.

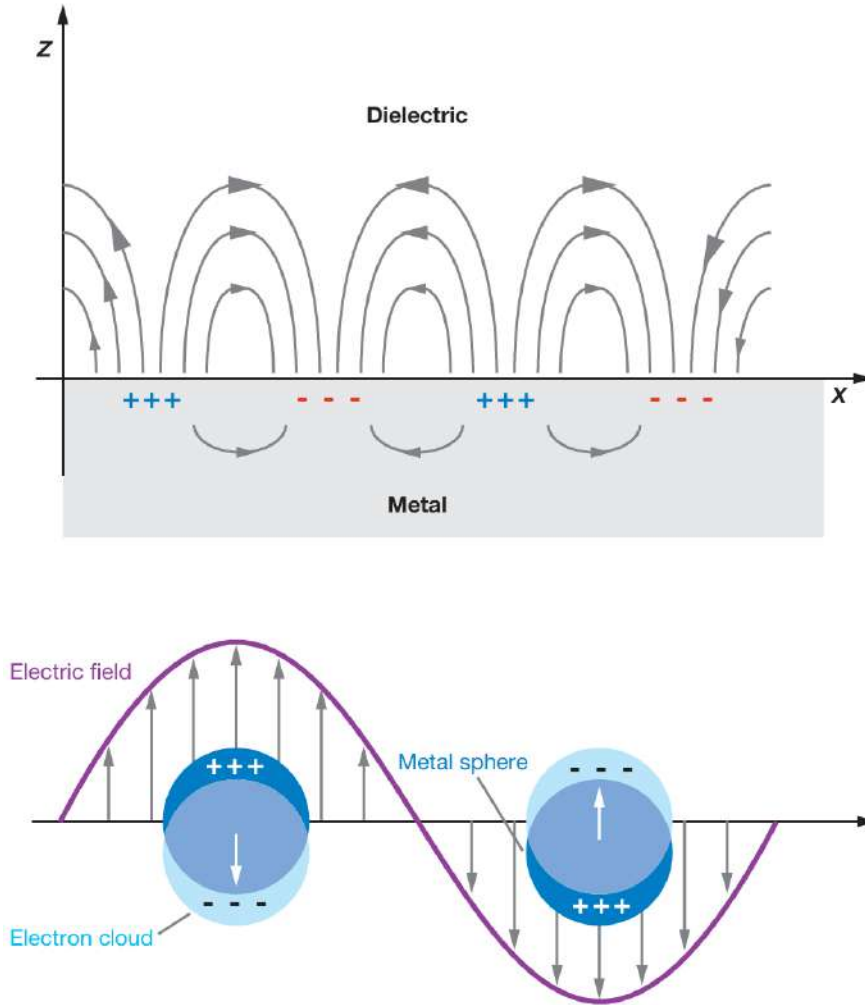


Figure 2.1: (a) Surface plasmon polariton. (b) Localized surface plasmons. [77]

To describe the surface plasmon resonance polarizability, α is introduced, which describes the tendency of charge distribution (like the free electrons in a metal nanostructure) to be distorted by an external electric field. In the case of a spherical metal nanoparticle with radius r the complex function α is given as [78],

$$\alpha = 4\pi r^3 \frac{\epsilon_m - \epsilon_d}{\epsilon_m + 2\epsilon_d} \quad (2.1)$$

Here ϵ_m is the wavelength-dependent complex dielectric function of the metal of the NP and ϵ_d is that of the surrounding dielectric. The dielectric function of a free electron metal is determined by the Drude formula as

$$\epsilon_m = 1 - \frac{\omega_p^2}{\omega^2 + i\omega\gamma} \quad (2.2)$$

Here, ω_p is the plasma frequency, γ is the damping constant. This condition corresponds to the surface plasmon resonance frequency ω_{sp} given by,

$$\omega_{sp} = 1 - \frac{\omega_p}{\sqrt{1 + 2\epsilon_d}} \quad (2.3)$$

With deviation from the spherical shape of the NP multiple resonance peaks can occur. The polarizability changes for each shape. For nanoparticles at an interface the dielectric the function of the surrounding medium can as an approximation be assumed as the average of the two materials (ϵ_1 and ϵ_2) at the interface can be illustrated as,

$$\epsilon_d = \frac{\epsilon_1 + \epsilon_2}{2} \quad (2.4)$$

2.1.1 Normal Modes of Sub-Wavelength Metal Particles

The interaction of a particle of size d with the electromagnetic field can be studied using the simple quasi-static approximation since $d \ll \lambda$ or the particle is substantially smaller than the wavelength of light in the surrounding medium. Since the phase of the harmonically oscillating electromagnetic field is essentially constant over the particle volume, it is possible to determine the spatial field distribution in this scenario by assuming that a particle is in an electrostatic field. The harmonic time dependency can be incorporated into the solution once the field distributions have been defined. The optical properties of nanoparticles smaller than 100 nm are well captured by this lowest-order approximation of the complete scattering problem for various applications.

A homogeneous, isotropic sphere of radius a situated at the origin in a steady, uniform electric field $\mathbf{E} = E_0 \bar{z}$ is the most practical geometry for an analytical treatment explained in Figure 2.2. At a sufficiently great distance from the sphere, the field lines are parallel to the z -direction and the surrounding medium is isotropic and non-absorbing with a dielectric constant of ϵ_m . The dielectric function $\epsilon(\omega)$, which we will assume for the time being to be a simple complex number ϵ , further describes the sphere's dielectric response.

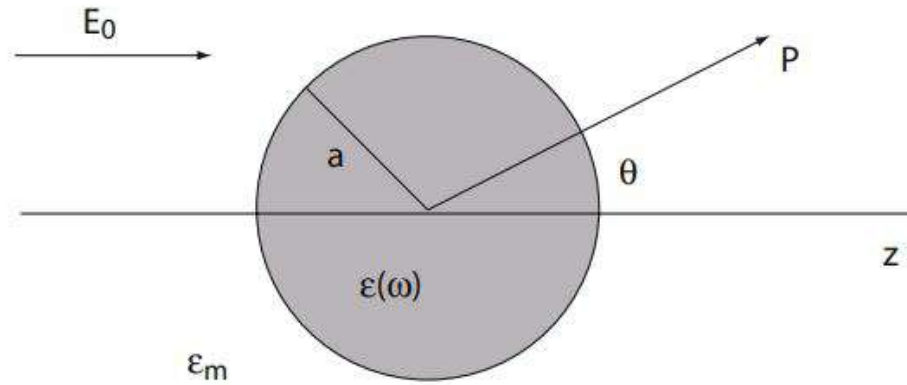


Figure 2.2: Sketch of a homogeneous sphere placed into an electrostatic field. [79]

2.2 Plasmonic Light Trapping in Thin-Film Solar Cells

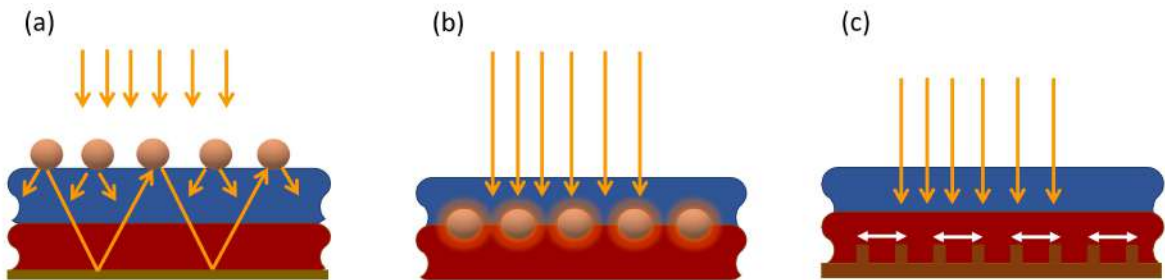


Figure 2.3: (a) Light trapping by scattering from metal nanoparticles at the surface of the solar cell. (b) Light trapping by the excitation of localized surface plasmons in metal nanoparticles embedded in the semiconductor. The excited particles' near-field causes the creation of electron-hole pairs in the semiconductor. (c) Light trapping by the excitation of surface plasmon polaritons at the metal/semiconductor interface.

To allow near-perfect light absorption and photo carrier collection conventionally, photovoltaic absorbers must be 'optically thick'. To improve the efficiency of solar cells, the system must have minority carrier diffusion lengths several times the material thickness for all photo carriers to be collected [80]. There are several ways of reducing the physical thickness of the photovoltaic absorber layers. Among them, plasmonic structures can be utilized in at least three ways while keeping their optical thickness constant, as seen in Figure 2.3. First, metallic nanoparticles have opened the opportunity to be used as sub-wavelength scattering elements to couple and trap freely propagating plane waves from the sun into an absorbing semiconductor thin film by folding the solar spectra into a thin absorber layer [81,82]. Here, light is preferentially scattered and trapped into the semiconductor thin film by multiple and

high-angle scattering, causing an increase in the effective optical path length in the cell. Second, metallic nanoparticles can be used as sub-wavelength antennas in which the plasmonic near-field is coupled to the semiconductor, increasing its effective absorption cross-section [83]. The excited particles' near-field causes the creation of electron-hole pairs in the semiconductor. Third, a thin photovoltaic absorber layer can couple solar spectrum into surface plasmon polarization modes supported at the metal/semiconductor interface by a corrugated metallic film on the back surface [6].

2.2.1 Light Scattering Using Particle Plasmons

Several research groups are looking into the full potential of the particle scattering concept, taking into account integration with enhanced anti-reflection coatings. Their form and size mostly determine the in-coupling efficiency of metal nanoparticles. This is seen in Figure 2.3 (a), which demonstrates that due to enhanced near-field coupling, smaller particles, whose effective dipole moment is placed closer to the semiconductor layer, link a greater portion of the incident light into the underlying semiconductor. In fact, 96% of the incident light is scattered into the silicon substrate at the limit of a point dipole, indicating the effectiveness of the particle scattering technique. The apex of the plasmon resonance spectrum exhibits the strongest of these light-trapping effects. Since metal nanoparticle scattering cross-sections can be up to ten times the geometric area, a solar cell with coverage of just 10% could convert most incident sunlight into plasmon excitations.

There is already a lot of experimental proof that the photocurrent spectral response of thin-film solar cells is enhanced by light scattering from arrays of metal nanoparticles. Various physical parameters must be harmonized to maximize plasmonic light trapping in a solar cell. The advantage of using small particles to achieve the forward scattering anisotropy observed in, Figure 2.4. However, scattering scales with volume v^2 , whereas extremely small particles suffer from significant ohmic losses that scale with volume v , making it desirable to use larger particles to improve the scattering rate. For instance, an Ag particle in the air with a diameter of 150 nm has an albedo (the percentage of light emitted as radiation) of up to 95%. Interestingly, spacing the particles farther from the substrate can avoid destructive interference effects between the incident and reflected particles, increasing the effective scattering cross-section. In contrast to improved coupling, Fano resonance effects can produce reflection for frequencies above the plasmon resonance by interfering destructively between scattered and unscattered light beams. One technique to solve the latter issue is utilizing a geometry where particles are positioned on the back of the solar cell. In this instance, poorly absorbed (infra-)red light is scattered and retained by metal nanoparticles while blue and green light are directly absorbed in the cell. On the solar cell's surface, metal strips' arrays may also be used to couple in light. Calculations indicate that compared to a solar

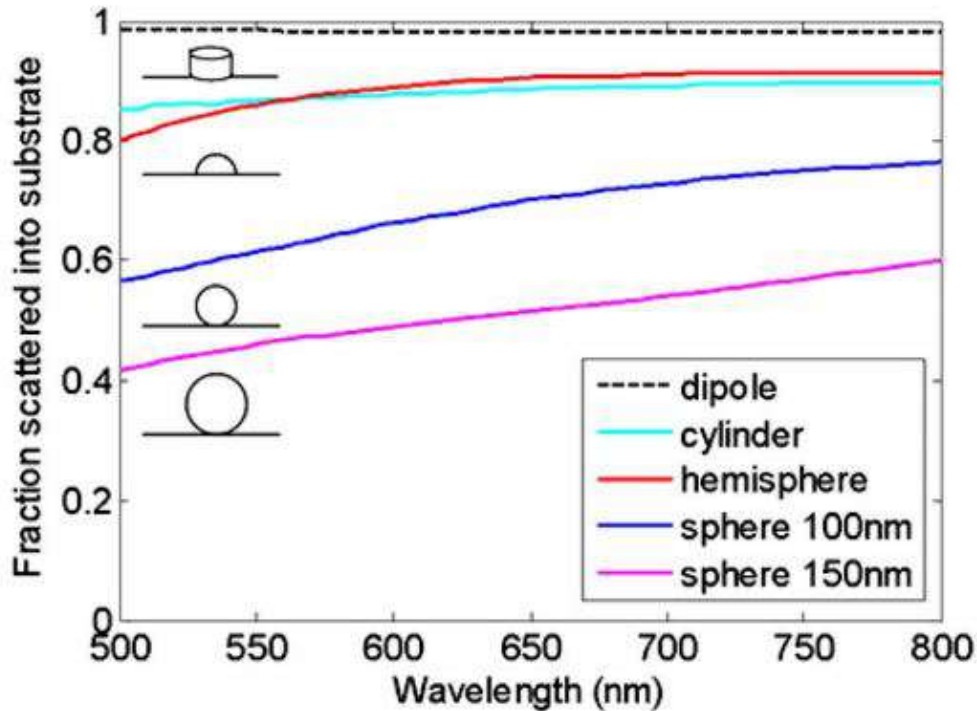


Figure 2.4: Fraction of light scattered into the substrate, divided by total scattered power, for different sizes and shapes of Ag particles on Si. Also plotted is the scattered fraction for a parallel electric dipole that is 10 nm from a Si substrate.

[84]

cell with a flat back contact, utilizing this design can increase the short-circuit current by 45%. Last but not least, we developed improved plasmonic light-trapping arrays.

2.2.2 Light Concentration Using Particle Plasmons

Resonant plasmon excitation utilizes the effective local field enhancement surrounding the thin-film solar cells as a substitute for metal nanoparticles to boost absorption in the semiconductor material around them. The incident sunlight is subsequently effectively captured by the nanoparticles, which serve as an "antenna," storing the energy in a confined surface plasmon state, can be seen in Figure 2.3 (b). The antennas are especially helpful in materials where short carrier diffusion lengths necessitate the generation of photocarriers close to the collection junction region. The absorption rate in the semiconductor must be greater than the reciprocal of the normal plasmon decay time (lifetime 10-50 fs) for these antenna energy conversion effects to be effective; otherwise, the absorbed energy is lost as ohmic damping in the metal. Many organic and direct-bandgap inorganic semiconductors can achieve such high absorption rates. Ultrathin-film organic solar cells doped with incredibly tiny (5 nm diameter) Ag nanoparticles have been shown to perform better.

2.2.3 Light Trapping Using SPPs

A third plasmonic light-trapping design transforms light into SPPs, electromagnetic waves that move along the boundary between a metal back contact and the semiconductor absorber layer as can be seen in surface plasmon state can be seen in Figure 2.3 (c). The evanescent electromagnetic SPP fields are confined close to the interface at dimensions significantly lower than the wavelength near the plasmon resonance frequency. Light can be efficiently trapped and guided into the semiconductor layer by SPPs excited at the metal/semiconductor contact. As a result of the effective 90° rotation of the incident solar light in this shape, light is effectively absorbed along the lateral direction of the solar cell, which has dimensions that are orders of magnitude more than the optical absorption length. This plasmonic coupling approach can be applied in a natural way because metal contacts are a typical component of solar-cell construction. SPPs experience quite substantial losses at frequencies close to the plasmon resonance frequency (usually in the 350–700 nm spectral region, depending on the metal and dielectric). It is possible to further tailor the plasmon dispersion by utilizing a thin-film metal shape. The ideal metal-fiber design, therefore, depends on the intended solar-cell shape because increased propagation length comes at the expense of decreased optical confinement. The SPP coupling mechanism is advantageous for efficient light absorption if the SPP is more strongly absorbed in semiconductors than in metals.

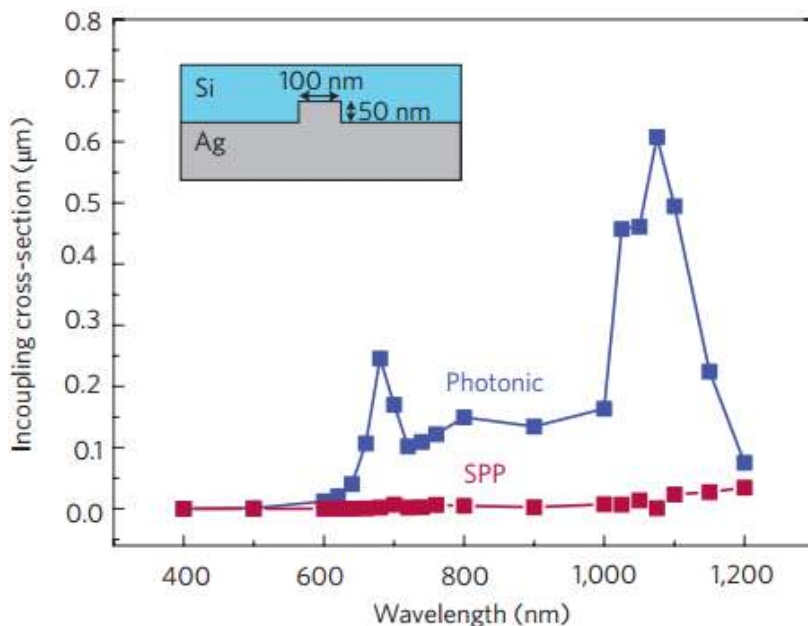


Figure 2.5: Two-dimensional calculation of the in-coupling cross-section for SPP and photonic modes as a function of wavelength for a 200-nm-thick Si slab.

[84]

The metal/dielectric interface must incorporate a light-incoupling structure due to the momentum mismatch between the incident light and the in-plane SPPs. The findings of electrodynamic simulations of the scattering from an incident plane wave into SPPs by a ridge

constructed in the Ag/Si interface are plotted in Figure 2.5 (taking into account in- and outcoupling). The Ag ridge is 50 nm tall and the Si layer is 200 nm thick. The simulations demonstrate that light is coupled into both an SPP mode and a photonic mode that propagates through the Si waveguide and that the height of the scattering item can vary the coupling strength to either mode. The photonic modes are particularly fascinating since their losses in the metal are so minute. With increasing wavelength, there is a rise in the percentage of light linked into both modes. This is mostly because the incoming light beam is directly absorbed in the Si layer at shorter wavelengths. The shape, height, and interparticle arrangements of incoupling structures can all be tuned for preferential coupling to specific modes, even though this example only demonstrates coupling from a single, isolated ridge. No photonic modes exist in the ultimate, ultrathin Si solar cell (thickness 100 nm), and all scattered light is transformed into SPPs. More analysis is necessary to determine whether three-dimensional scattering structures integrated in the rear contact will improve further. Research on amorphous Si thin-film solar cells coated on a textured metal back reflector has shown a 26% increase in short-circuit current, with the predominant photocurrent increase occurring in the near-infrared spectrum [85].

A comparable conversion mechanism into surface polariton waves has recently been established concerning the plasmonic coupling effect, although employing lossy dielectrics rather than metals [86]. Another efficient light coupling into a two-dimensional wave that can be absorbed in a semiconductor layer occurs here. Several other publications on integrating SPP geometries with thin-film solar-cell geometries, including organic solar cells, are also emerging [87, 88].

2.3 Alternative Plasmonic Materials

Understanding how nanophotonic devices work and what they are constructed of will help one better comprehend the pressing need for materials innovation in this field. Nanophotonics makes it feasible to confine light to the nanoscale, a feat made possible by materials with a high refractive index or resonance. Although no naturally occurring materials have exceptionally high refractive indices at optical frequencies, connecting light to electronic resonances in materials is a typical technique. A wide band of wavelengths, including infrared, visible, and ultraviolet, can enable electronic or plasmon-polaritonic resonance in free electron plasma, just like in metals. Metals are one of the fundamental components of nanophotonic devices and are hence referred to as plasmonic materials.

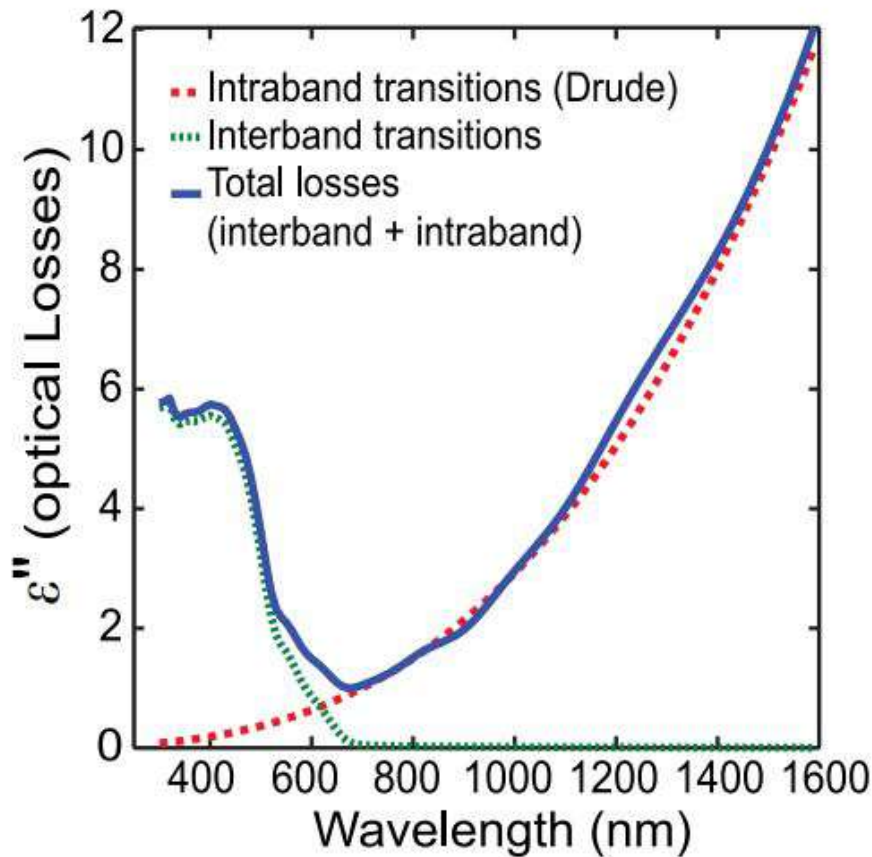


Figure 2.6: The imaginary part of permittivity of gold in the optical range (solid line), the individual contributions from free electron losses (intraband transitions) and interband transition losses are shown in dotted lines.

[16]

2.3.1 Limitations of Noble Metals

Due to their low ohmic losses, silver and gold are frequently utilized in plasmonic and optical metamaterial systems. However, interband transitions, a different loss process, play a significant role in these metals at optical frequencies. When an electron near the Fermi surface absorbs a photon to jump to the next vacant conduction band or when a valence electron in a metal absorbs a photon to jump to the Fermi surface, a loss from interband transitions results. The loss process that gives copper and gold their color is accountable for this. Figure 2.6 depicts the imaginary part of gold's optical permittivity. Two components to the loss are represented by the imaginary fraction of permittivity: interband and intraband losses. The near-infrared (NIR) has large intraband losses (or Drude losses) in gold, while shorter wavelengths have reduced intraband losses. On the other hand, for shorter visible wavelengths, interband losses in gold are substantial. Metals like gold are unsuitable for many plasmonic and metamaterial devices due to the extra losses at optical frequencies brought on by interband transitions. Even when interband transitions are absent in the op-

erating spectral range for applications like transformation optics (TO) that demand that the imaginary part of a metal's dielectric function is small, intraband transitions and scattering losses are invariably present and frequently lead to significant overall losses. One of the main drawbacks of utilizing metals like gold and silver in plasmonics, optical metamaterials, and TO is the significant loss in typical plasmonic materials. One problem is that in ordinary metals, the actual fraction of the permittivity has a very large magnitude. Since many TO devices frequently need meta-molecules with a nearly balanced polarization response, this presents a challenge in their design. The geometric fill fractions of the metal and dielectric can be easily modified to meet the design requirements when the real parts of permittivity of the metal and dielectric are in the same order. The metal fill fraction in the meta-molecule will be a few orders smaller than the dielectric if, on the other hand, the magnitude of the real component of permittivity of the metal is a few orders bigger than that of the dielectric. This restriction would require the meta molecule to have incredibly minute metal inclusions, which presents a variety of challenges, particularly for successful nanofabrication. Therefore, it would be preferable in many applications for plasmonic materials to have smaller magnitudes of real permittivity.

Metals present difficulties for nanofabrication in addition to the loss and nonadjustable dielectric permittivity problems mentioned above, particularly when formed as thin films. When compared to bulk metal, metal thin films have quite distinct morphologies, which might cause the optical characteristics to deteriorate. First off, thin metal films deposited using standard methods such as sputtering or evaporation frequently form discontinuous or semi-continuous filaments. When formed on widely used substrates like glass, quartz, sapphire, and silicon, metal films show a percolation threshold in the film thickness. It would need more work, such as the use of a wetting layer or a substrate that matches the lattice, to go over this limit. However, these methods have drawbacks in terms of scalability and design integration. Typically, the structure of thin metal films is made up of several tiny grains. The optical characteristics of thick films, on the other hand, are similar to those of bulk materials since they are often made of big grains. When the films are thin, the granular structure increases the losses in the metal by increasing grain-boundary scattering for free electrons. Surface roughness is connected to another loss process resulting from the microstructure of thin metal sheets. Rough surfaces and edges are inevitably produced during nanoscale patterning, which increases optical losses and scattering.

The chemical stability of the materials is a crucial factor to consider in the context of realistic devices and integration. In the manufacture and integration of devices, the deterioration of metals due to exposure to air, oxygen, or humidity would present additional challenges. Silver and copper, which are common plasmonic materials, are known to deteriorate in air, yet gold is remarkably robust there. Silver is sensitive to sulfidation and tarnishes to generate a layer of silver sulfide, whereas copper forms a native oxide layer in the air. These metals'

optical properties are directly impacted by tarnishing, and as a result, optical losses rise, increasing the imaginary component of the dielectric function's values.

The inability to quickly alter or adjust the optical characteristics of metals is a major disadvantage. For instance, applying mild electric, optical, or thermal fields will not significantly alter the carrier concentration of metals. Therefore, metals cannot be employed as tunable elements in applications where switching or modifying the optical characteristics is crucial. The numerous drawbacks of conventional plasmonic materials have motivated researchers to search for alternatives. There have been numerous reports of several alternative materials that can overcome one or more of the drawbacks mentioned above [89–91].

2.3.2 Optical Properties of Materials

Free electrons as plasma in plasmonic materials can support electronic or plasmon over a broad spectrum from infrared to ultra-violet light. The free-electron response of metals can be described from the Drude model.

$$\epsilon_{Drude} = \epsilon_b - \frac{\omega_p^2}{(\omega^2 + \gamma^2)} + i \frac{\omega_p^2}{(\omega^2 + \gamma^2)\omega} \quad (2.5)$$

$$\gamma = \gamma_0 + A \frac{v_F}{d} \quad (2.6)$$

$$\gamma = \text{Loss factor} \times \gamma_0 \quad (2.7)$$

Here ϵ_b is the polarization response from the core electrons, ω_p is the plasma frequency and γ is the Drude relaxation rate. Scattering and ohmic losses are caused by the relaxation rate, which scales in direct proportion to the imaginary part of the dielectric function. Additionally, the real and imaginary parts of the permittivity scale are directly proportional to the square of the plasma frequency, ω_p^2 , which is proportional to carrier concentration (n). The Drude scattering rate, or γ , has been observed to be a phenomenological parameter in optics that depends on the microstructure of the plasmonic structure. For instance, the metal film's interior grain size can raise the carrier dispersion rate. The relaxation rate is given by γ_0 when the grain size is large, as in a bulk metal. since there is more grain-boundary scattering when the grain size is small, as in the case of thin metal films, (2.6) characterizes the increased relaxation rate, where A is a dimensionless empirical constant, v_F is the Fermi-velocity of the electrons in the metal and d is the average grain size. Smaller grains result in a larger γ and, hence, higher losses. Surface roughness is yet another element that could increase the effective γ . A quantity termed the loss factor, which is stated in (2.7)

can be used to describe all of these impacts objectively. Experimental results indicate that nanopatterned gold and silver films typically have a loss factor of 3 to 5.

While the reaction from free carriers (or intraband transitions in a quantum image) is well captured by the Drude model, the response from interband transitions of electrons is more challenging to explain. Interband transitions, which take place when electrons move from one energy band to a higher unoccupied energy band by absorbing light photons, are a substantial loss mechanism in materials at optical frequencies. When an incoming photon strikes a bound electron in a metal, the electron may move from a lower energy band to the Fermi surface or from a region close to the Fermi surface to the following higher empty energy band. High loss is experienced at optical frequencies as a result of both of these interband transitional processes.

2.3.3 Finding Alternatives

It is difficult to develop materials with a certain set of qualities; thus, researchers frequently use a range of techniques to address this issue. For instance, the decreased carrier concentration in plasmonic materials might result in a lower imaginary permittivity and a smaller magnitude of real permittivity in the section on ideal plasmonic materials. Doping semiconductors to provide just enough free carriers and eliminating extra free carriers from traditional plasmonic materials by alloying and compounding are two methods for reducing or modifying the carrier concentration. There have been many strategies to find alternative plasmonic like

- Increasing the carrier concentration in semiconductors enough to cause them to behave like metals. Lower limits are placed on the required carrier concentration by achieving metal-like optical characteristics ($\epsilon' < 0$) in the desired spectrum. This minimal carrier concentration can be calculated using the Drude model's description of the optical response of free carriers from (2.5). The lower limit on the plasma frequency (ω_p) and, therefore the carrier concentration (n) is provided by 2.8 to get metal-like characteristics ($\epsilon' < 0$) for $\omega < \omega_c$

$$\omega_p^2 > \epsilon_b(\omega_c^2 + \gamma^2), \quad n > \frac{\epsilon_0 m^*}{e^2} \epsilon_b(\omega_c^2 + \gamma^2) \quad (2.8)$$

where ϵ_0 is the vacuum permittivity, e is the electron charge, and m^* is the effective mass of the carrier

- Compounds of III-V semiconductors, such as those based on GaAs and InP, are semiconductors with an optical bandgap that is comparable to that of silicon and the electron mobility is very high in these materials due to a small effective mass. A carrier

concentration greater than 10^{20} cm^{-3} is needed to exhibit plasmonic characteristics in these materials at the telecommunication wavelength. However, due to the reduced solid solubilities of the dopants and poor doping efficiency, such high doping is exceedingly difficult in these materials. It is known that doping at levels higher than 10^{19} cm^{-3} might have effects like doping compensation. As an illustration, silicon is a typical n-type dopant in GaAs, but at high doping levels, silicon can also function as a p-type dopant. Due to silicon's ability to adapt, doping efficiency is low at large doping densities. Beyond 10^{19} cm^{-3} , N-type doping is unquestionably challenging in GaAs films.

- Metallic alloys, intermetallics and metallic compounds are potential candidates for alternative plasmonic materials owing to their large free electron densities. Noble metals have excellent plasmonic properties; therefore, one way to make these materials better is to move the interband transitions to a different (less significant) region of the spectrum. This can be done by reacting or alloying two or more elements to produce distinctive band structures that can be fine-tuned by changing the ratio of each reactant or alloy. Since noble metals are the typical plasmonic materials, noble metal alloys have drawn much attention. Studies on standard plasmonic alloys of Ag-Cu, Au-Ag, Ag-Al, Au-Cd, Ag-In, and Ag-Mg have revealed that the optical properties typically degrade below the best of the original metals. However, alloying aids in altering the interband transitions, where it has been found that a straightforward mixing algorithm provides a fair approximation.
- Another approach to decrease the excessive optical losses in metals is to reduce the carrier concentration in the material. A smaller carrier concentration may be achieved in intermetallic or metallic compounds, which we will term "dilute metals" or "less metals." In general, the carrier concentration is decreased when non-metallic components are added to a metal lattice. Additionally, this modifies the electrical band structure and may have unfavorable effects like increased Drude-damping losses and massive interband absorption losses. However, there is a lot of opportunity for improvement, and academics haven't paid much attention to this area of study. The benefits of plasmonic intermetallic or metallic compounds, such as their tunability and simplicity in production and integration, may outweigh their drawbacks. Therefore, it is worthwhile to continue looking for products that contain diluted metals. According to a review of the literature, numerous types of diluted metals have had their optical characteristics investigated in the past. They include ceramics such as oxides, carbides, borides, nitrides, and metal silicides and germanides, which were all discovered to display negative real permittivities in various regions of the optical spectrum. None of these materials have minimal optical losses, and none of them have all the desirable qualities. But there has been a rise in curiosity about critical substances in

terms of technological applications. Particularly, metal nitrides and silicides, already employed in silicon CMOS technology, have drawn much attention.

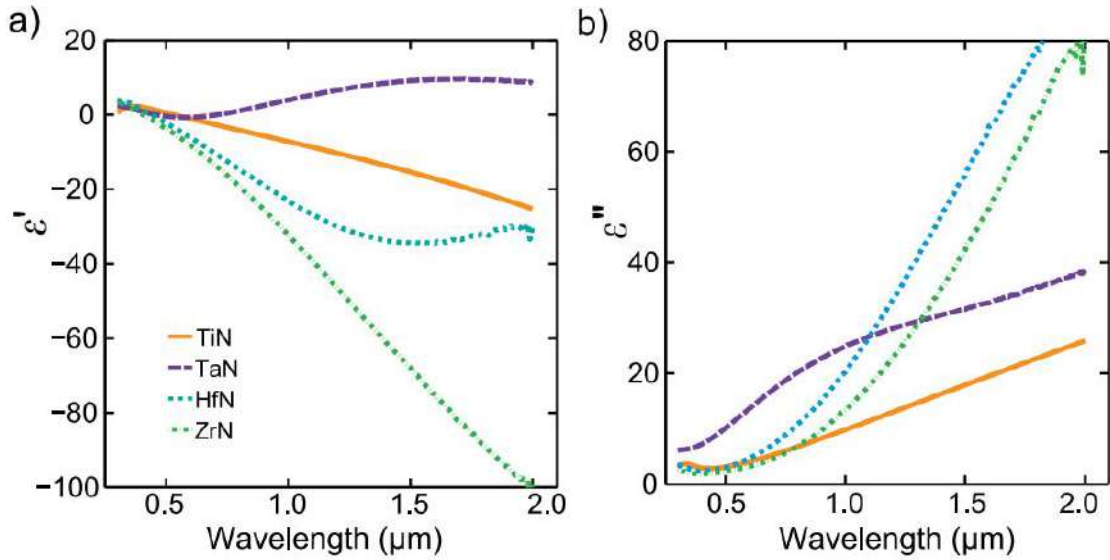


Figure 2.7: Optical constants of metal nitride thin films deposited using DC reactive sputtering. The (a) real and (b) imaginary parts of dielectric functions.

[16]

Metal nitrides such as titanium nitride (TiN), zirconium nitride (ZrN), and tantalum nitride (TaN) are notable for carrying metallic properties within the visible and infrared wavelengths [18, 19, 92]. These nitrides are non-stoichiometric, interstitial compounds with large free-carrier concentrations, their real and imaginary part of the dielectrics are presented in Figure 2.7. These materials are refractory, stable, and hard. Amazingly, their optical properties are tunable by varying their composition [13, 15]. However, metal nitrides offer fabrication and integration advantages which could be useful to overcome the challenges of the metals. Among them, Titanium Nitride (TiN) is an interstitial compound with a high concentration of free carriers. Moreover, they are compatible with silicon CMOS technology.

2.4 Scattering of Light by NPs

2.4.1 Scattering Cross-Section

A scattering cross-section, Q_T is a quantity proportional to the rate at which a particular radiation–target interaction occurs. Specifically, if the incoming radiation is considered as being composed of quanta or particles a cross-section is a scattering rate (number of scattering events per unit time) per unit incident radiation flux, where the latter is the number

of incident particles striking the target surface per unit time per unit area. Scattering cross-sections are determined by dividing the power of the scattered wave by the intensity of the incident wave, where the radiation is treated as a continuous wave.

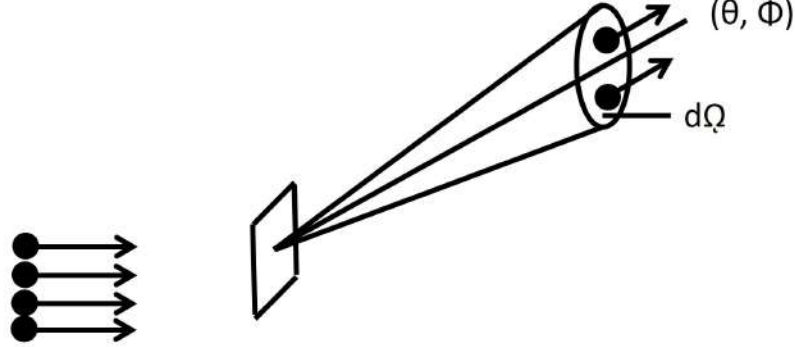


Figure 2.8: Standard scattering geometry for measuring differential scattering cross-section.

Differential scattering cross-sections, dQ_T are determined by placing a detector at a particular angular position at a substantial distance away from the scattering target as can be seen in Figure 2.8. The incident beam travels in the positive z -direction and the radiation is scattered into a differential solid angle $d\Omega$ at polar angle θ and azimuthal angle ϕ . The differential scattering cross-section can be presented as

$$dQ_T/d\Omega = dR/d\Omega \phi_{in} \quad (2.9)$$

Based on the Localized Surface Plasmon Resonance (LSPR) for NPs at interfaces scattering cross-section, Q_T can be calculated from

$$Q_T = \frac{1}{6\pi} \left(\frac{2\pi}{\lambda}\right)^4 |\alpha|^2. \quad (2.10)$$

Here, α can be calculated from (2.1).

2.4.2 Absorption Cross-Section

Absorption cross-section is a measure of the probability of an absorption process. It quantifies the probability of a certain particle-particle interaction. Absorption cross-section is the ability of a nanoparticle to absorb a photon of a particular wavelength and polarization. Analogously, it refers to the probability of a particle (usually a neutron) being absorbed by a nucleus. The total absorbed power divided by the power per unit area of the incident light

was defined as absorption cross-section, Q_{ab} . It can be presented as

$$dN/dz = -NnQ_{ab}. \quad (2.11)$$

Here, dN/dz is the number of photons absorbed between the points z and $z+dz$, N is the number of photons penetrating to depth z , and n is the number of absorbing molecules per unit volume. Based on the Localized Surface Plasmon Resonance (LSPR) for NPs at interfaces Q_{ab} can be calculated from,

$$Q_{ab} = \frac{2\pi}{\lambda} \text{Im}[\alpha]. \quad (2.12)$$

2.5 Near Field and Far Field

The quasi-static approach, the finite element method (FEM), the finite-difference time-domain (FDTD) method, and the discrete dipole approximation (DDA) can be used to study the near- and far-field plasmonic properties of dielectric metals. The metal's dielectric function, the surrounding dielectric environment, and, most significantly, the form of the particle all affect where the extinction maximum appears on the spectrum. The findings from the quasistatic model of the particles qualitatively describe all these dependencies presented in (2.1). Analytically, the electromagnetic field of an oscillating point dipole positioned in the center of the particle can be used to approximate the electromagnetic field of the dipolar surface plasmon modes on ellipsoidal metal nanoparticles. This is consistent with the findings of the quasistatic approximation for spherical particles, but it also holds true for dipolar surface plasmon resonances on arbitrarily shaped metal nanoparticles. The fundamental finding from this approach is that the electromagnetic field of Surface plasmonics on metal nanoparticles (SPNs) has two limiting spatial domains:

- The near field: The term "near field" refers to areas close to the metal or inside any polarizable material surrounding it where interference with the generation and emission of electromagnetic waves is possible while the field lines are electrically connected to the antenna. As a result, radiation absorption in the near field by nearby conducting objects noticeably affects the loading on the signal generator (the transmitter). In various subregions of the near field, the electric and magnetic fields can coexist separately and one type of field can be disproportionately greater than the other. It dominates in the vicinity of the particle for distances much smaller than the wavelength of the electromagnetic fields. For spherical particles, it diminishes proportionally to r^{-3} with increasing distance r from the particle center. Retardation effects barely matter under this regime.

- The far field: The area where the field has settled into "normal" electromagnetic radiation is known as the far field. Transverse electric or magnetic fields with electric dipole properties predominate in this area. Radiated power declines with distance in the far-field zone, and radiation absorption does not flow back to the transmitter. Spherical waves predominate at distances from the particle substantially greater than the wavelength of the electromagnetic fields. The field decreases in this region of r -distance proportionally to r^{-1} . The ratio of the electric and magnetic field intensities is essentially the wave impedance of the medium in the far-field region, where each electric and magnetic component of the electromagnetic field is produced by a change in the other component.

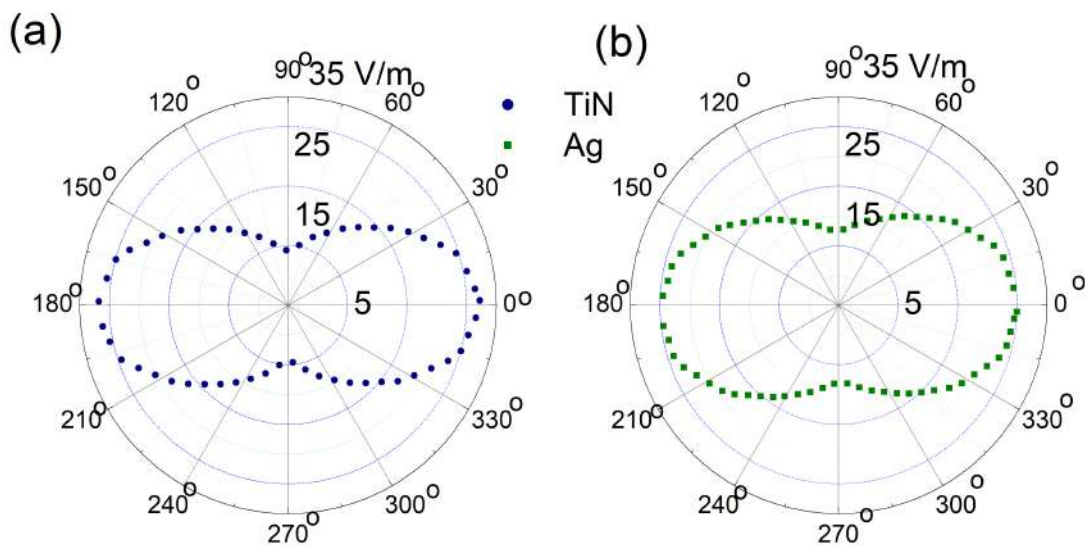


Figure 2.9: Polar plot for far-field spectra in xy plane depending on incident light for the 100 nm radius nanosphere consisting of TiN and Ag.

Understanding surface plasmon polaritons' basic optical characteristics and creating miniature photonic devices depend on mapping the near-field profiles and dynamics of these particles. The effective polariton wavelength is shorter than the free-space excitation wavelengths, necessitating a spatial resolution on the sub-wavelength scale. Here, the spatial distribution of the dominant perpendicular component of surface plasmon fields in a metal nanoparticle-film system can be mapped at the sub-wavelength scale by combining total internal reflection excitation with surface-enhanced scattering imaging. This is done by spectrally selective and polarization-resolved excitation of the vertical gap mode. The far field of TiN and Ag 100 nm spheres are presented in Figure 2.9.

Figure 2.10 displayed the near-field enhancement surrounding a TiN monomer on a silicon substrate. Color map showing the xy, zx, yz distribution of $|E|$ for TiN nanosphere. As the source was incident on the z-axis and the polarization was along the x-axis, the field

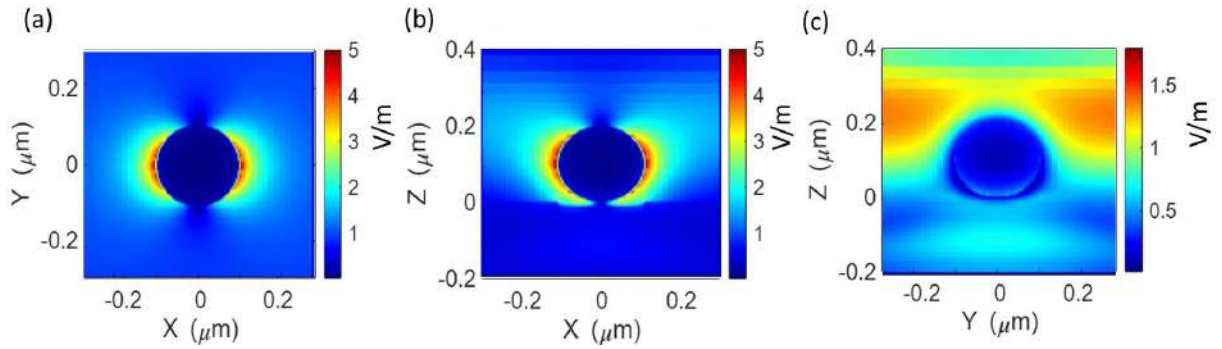


Figure 2.10: Color map showing the spatial (a) xy , (b) zx , (c) yz distribution of $|E|$ for TiN monomer NP placed on top of a thin Si_3N_4 on a Si substrate.

enhancement was observed along the x -axis. The xy plane had a better enhancement than zx and yz planes.

2.6 Solar Cell Model

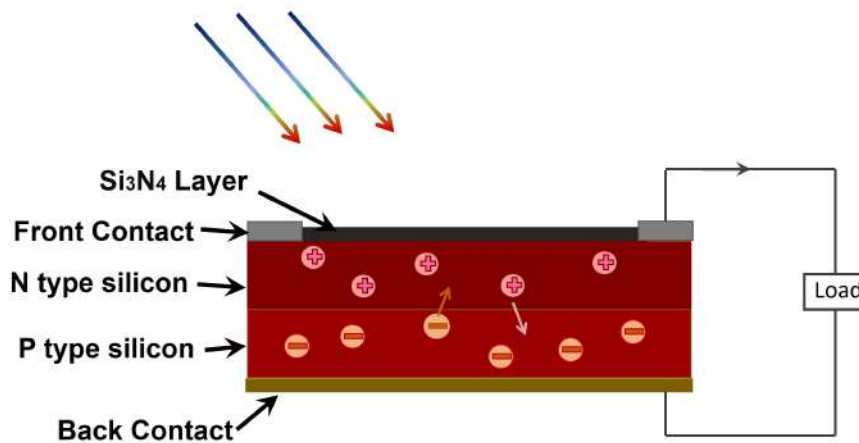


Figure 2.11: A p-n junction solar cell.

The solar cell structure consists of two layers of different semiconductor materials doped differently. The solar cell is like a p-n junction diode. An absorber layer with embedded metal elements is used on the upper side of the electrode to avoid penetration of direct solar irradiation. The fundamental building block of a solar energy generation system is a solar cell directly converts light energy into electrical energy without the need for any additional processing. A solar cell is also referred to as a photovoltaic cell because it exclusively relies on its photovoltaic effect. A semiconductor device is essentially for a solar cell. The current capacity of the cell is nearly proportional to the intensity of incident light as well as the area that is exposed to the light, whereas the voltage or potential difference established across the terminals of the cell is fixed and is essentially independent of incident light intensity.

Like all other types of battery cells, each solar cell contains one positive and one negative terminal. A photovoltaic or solar cell typically has a positive rear contact and a negative front contact. Between these two contacts lies a semiconductor p-n junction.

Some photons of light are absorbed by the solar cell while sunlight is shining on it. Some of the absorbed photons will have energy above the semiconductor crystal's valence band–conduction band energy gap. As a result, one excited valence electron gains energy from one photon, leaps out of the bond, and produces one electron-hole pair. Light-generated electrons and holes are the electrons and holes in these e-h pairs presented in Figure 2.11. Due to the electrostatic force of the field across the junction, light-generated electrons close to the p-n junction migrate to the n-type side of the junction. Similar electrostatic forces cause the light-generated holes produced close to the junction to migrate to the p-type side of the junction. By creating a potential difference between the two sides of the cell in this manner, current will begin to flow from the positive to negative terminals of the solar cell if an external circuit connects the two sides. This was the fundamental idea behind how a solar cell functions.

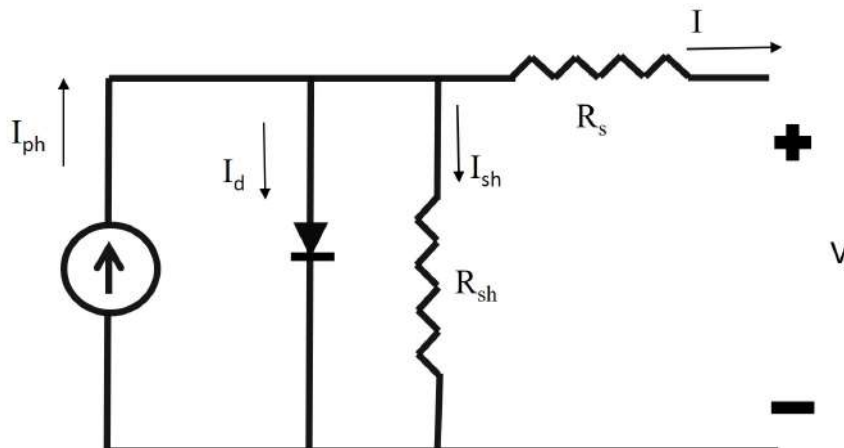


Figure 2.12: The equivalent electrical circuit of a single solar cell.

Solar cells are designed in different sizes and shapes to maximize the effective surface area and reduce the losses because of contact resistance. Each technology leads to building PV cells using the physics variables such as the power-voltage and current-voltage relationships. Although irradiance is an essential factor in the efficiency of a solar cell, the behavior of different types of solar cells is similar in different irradiances. Thus, electrical equivalent circuits are used as the models to describe their electrical behavior presented in Figure 2.12. Generally, the Shockley diode equation is used to determine the characteristics of the solar cells [93]. So a solar cell is modeled as a light sensor that absorbs the photons of irradiation and converts them into current. Also, an anti-parallel connected diode to the light sensor manages the current's direction. Based on the described model, a mathematical equation shows a solar cell's implicit and nonlinear current-voltage relationship. Finally, numerical

and analytical methods with a series of simplifications and approximations are used to solve the implicit nonlinear equation of the $I - V$ relation [94].

In the above model, I is the output current obtained by the Kirchhoff law,

$$I = I_{ph} - I_D \quad (2.13)$$

$$I_D = I_0 \left[\exp\left(\frac{V}{AV_T}\right) - 1 \right] \quad (2.14)$$

where V is the voltage imposed on the diode, I_0 is the leakage current or the reverse saturation current of the diode, I_{ph} is the photocurrent, A is the ideality factor of diode and V_T is called the thermal voltage of the diode because of its exclusive dependency on the temperature. The thermal voltage can be calculated by $V_T = \frac{k_B T}{q}$ where q is the unit of electrical charge, k_B is the Boltzmann constant, and T is the cell temperature in Kelvin.

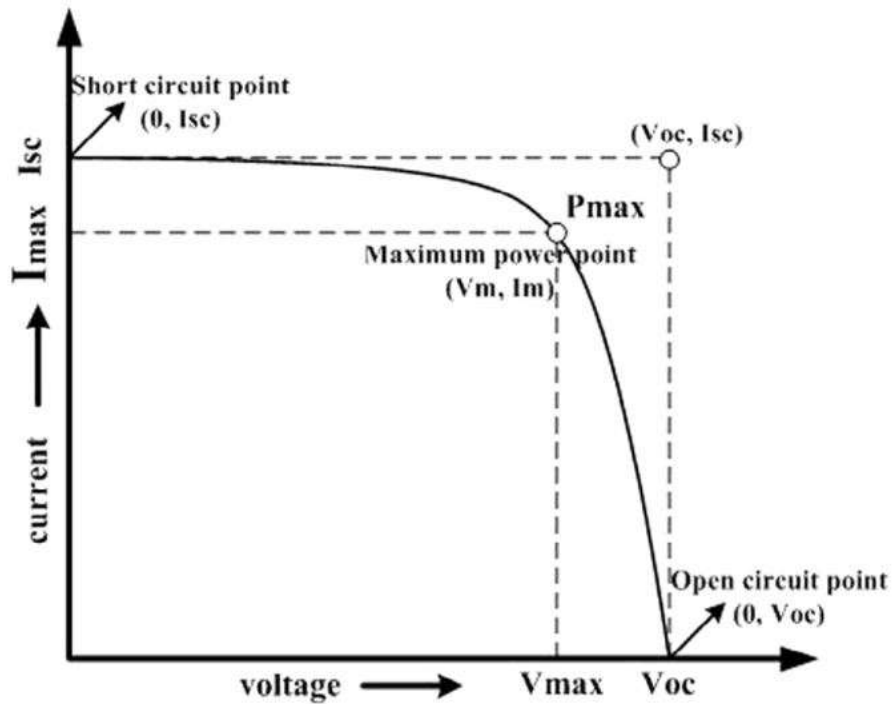


Figure 2.13: Current-voltage characteristic of a solar cell.

There is an optimum point of (I_m, V_m) $I - V$ curves where both the current and voltage have the maximum amount simultaneously. The maximum electrical power that a solar cell can produce will be present at the bend point of the characteristic curve if we plot the $I - V$ characteristics of a solar cell, as seen in Figure 2.13. It is demonstrated in the $I - V$ characteristics of solar cells by P_m . The current at which maximum current occurs is shown in the $I - V$ characteristics of solar cells by I_m . The voltage at which maximum

power occurs is shown in the $I - V$ characteristics of solar cells by V_m . Also, there are two other characteristics I_{sc} as the short-circuit current when $V=0$ and V_{oc} is the open-circuit voltage when $A=0$. Short-circuit current is the solar cell's maximum current capacity without endangering its own constriction. It is determined by short-circuiting the cell's terminals while it is in its most optimal state for delivering the most amount of output. The phrase "optimized condition" was adopted because, for fixed exposed cell surfaces, the rate of current production in solar cells depends on both the amount and angle of light hitting the cell. It is preferable to indicate maximum current density rather than maximum current since current production also depends on the amount of cell surface that is exposed to light. The ratio of the cell's exposed surface area to the maximum or short circuit current is known as the maximum current density or short circuit current density rating expressed as,

$$J_{sc} = \frac{I_{sc}}{A}. \quad (2.15)$$

When no load is attached to the cell, the voltage between its terminals is monitored. This voltage is influenced by manufacturing processes and temperature but less so by light intensity and exposed surface area. Solar cells typically have an open circuit voltage between 0.5 and 0.6 volts.

Finally, based on these characteristics, it can result in another Fill Factor (FF), which is defined by,

$$FF = \frac{I_m V_m}{I_{sc} V_{oc}}. \quad (2.16)$$

$$I_{sc} = I_{ph} - I_0 \left[\exp\left(\frac{I_{ph} R_s}{A V_T}\right) - 1 \right] \quad (2.17)$$

The factor that affects the final current is all-external resistance that leads to reduce the electric current because of connections between the solar cells and other parts of the electrical system. This resistance is represented by R_s and is called the series resistance.

$$V_{oc} = A V_T \ln \left(1 + \frac{I_{sc}}{I_0} \right) \quad (2.18)$$

The higher value of FF means the PV cell has more efficiency. The power conversion efficiency, η is referred to as a ratio and represented in percentage terms as the highest electrical power output to the radiation power input to the cell, which can be calculated from (2.16) to (2.18),

$$\eta = \frac{V_{oc} I_{sc} FF}{P_{in}}. \quad (2.19)$$

Here P_{in} is the power density of the average global solar spectrum after passing through 1.5

atmospheres. It has a value of 100 mW/cm²

2.7 Optical Simulation Model

One of the most often used methods nowadays for solving electromagnetic problems is the FDTD method. We used an FDTD-based software package to conduct the optical calculations. It has been used to solve a remarkably broad range of issues, including scattering from metal and dielectric objects, antennas, microstrip circuits, and electromagnetic absorption in the exposed human body. The primary factor influencing the FDTD method's effectiveness is its extraordinary simplicity, even when used to design a three-dimensional code. K. Yee was the one who first proposed the method, which was later modified in the early 1970s by others.

Complex refractive index= $n + j\kappa$ of each layer was used to model the solar cells in FDTD, where n , k are the dielectric permittivity, refractive index, and extinction coefficient, respectively. The standard solar spectrum AM 1.5G was utilized to model the solar irradiance that was incident perpendicularly. The simultaneous time-dependent solution of Maxwell's third and fourth equations, which is provided by, serves as the foundation for the FDTD simulator.

$$\frac{\partial E}{\partial t} = \frac{1}{\epsilon_0} \nabla \times H \quad (2.20)$$

$$\frac{\partial H}{\partial t} = -\frac{1}{\mu_0} \nabla \times E \quad (2.21)$$

Here, E is the electric field intensity, and ϵ_0 is the permittivity of free space. H is the magnetic field intensity, and μ_0 is the permeability of free space. In the one-dimensional case, we can use only E_x and H_y , and (2.20), (2.21) can be rewritten as

$$\frac{\partial E_x}{\partial t} = -\frac{1}{\epsilon_0} \frac{\partial H_y}{\partial z} \quad (2.22)$$

$$\frac{\partial H_y}{\partial t} = -\frac{1}{\mu_0} \frac{\partial E_x}{\partial z} \quad (2.23)$$

that represents a plane wave traveling in the z -direction.

Maxwell's equations are discretized using central difference approximations to the partial derivatives of space and time. The finite-difference equations are subsequently resolved using the leapfrog technique. Yee's scheme consists in considering E_x and H_y shifted in space by half a cell and in time by half a time step when considering a central difference

approximation of the derivatives.

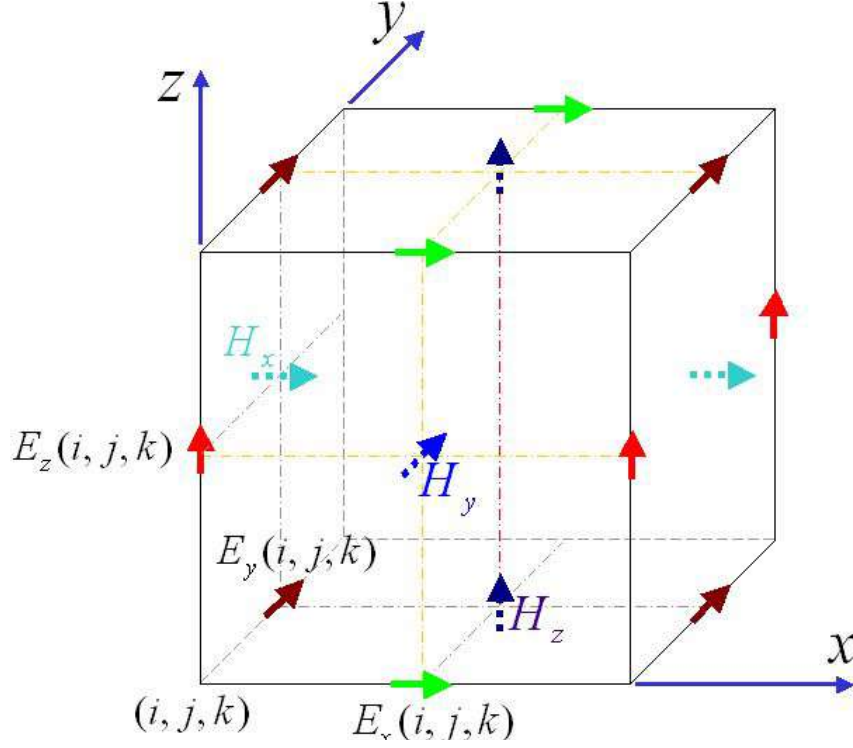


Figure 2.14: Yee grid in three-dimensional simulation domains. [95]

In such a case, (2.22) and (2.23) can be written as

$$\frac{E_x^{n+1/2}(K) - E_x^{n-1/2}(K)}{\Delta t} = -\frac{1}{\epsilon_0} \frac{H_y^n(K + 1/2) - H_y^n(K - 1/2)}{\Delta z} \quad (2.24)$$

$$\frac{H_y^{n+1}(K + 1/2) - H_y^n(K - 1/2)}{\Delta z} = -\frac{1}{\mu_0} \frac{E_x^{n+1/2}(K) - E_x^{n-1/2}(K)}{\Delta z} \quad (2.25)$$

A spatially staggered vector component of the E-field and H-field about rectangular unit cells of a Cartesian computing grid was introduced by this method. Each E-field vector component is sandwiched between two H-field vector components because of how it was put up. Later, this grid came to be known as the Yee grid presented in Figure 2.14.

2.8 Electrical Simulation Model

A 2D-axisymmetric simulation was performed to calculate the photocurrent (J_{ph}) and other parameters by solving the drift-diffusion equations for obtaining the electrical characteristics of the solar cells by using the generation rate ($G=G_n/G_p$) imported from the optical

simulation results of the FDTD solver. The drift-diffusion equations for electrons and holes (carriers) are given by,

$$J_n = q\mu_n n E + qD_n \nabla_n, \quad (2.26)$$

$$J_p = q\mu_p p E - qD_p \nabla_p. \quad (2.27)$$

Where $J_{n(p)}$ is the current density of electron (hole) (A/cm²), q is the positive electron charge, $\mu_{n(p)}$, is the mobility of electron (hole), E is the electric field, $D_{n(p)}$, is the diffusivity of electron (hole), and n and p are the densities of the electron and hole, respectively. Each carrier (electron or hole) moves under the influence of two competing processes: drift due to the applied electric field and random thermal diffusion due to the gradient in the density.

The mobility $\mu_{n(p)}$ describes the ease with which carriers can move through the semiconductor material and is related to the diffusivity, $D_{n(p)}$ through the Einstein relation represented by,

$$D_{n(p)} = \mu_{n(p)} \frac{k_B T}{q}. \quad (2.28)$$

Here k_B is the Boltzmann constant. The mobility is a key property of the material and is modeled as a function of temperature, impurity or doping concentration, carrier concentration, and electric field. We must ascertain the answers to the following Poisson's equation to find the electric field to solve drift-diffusion equations.

$$-\nabla \cdot \epsilon E = E(p - n + N_A - N_d). \quad (2.29)$$

N_A and N_d are the acceptors, and donor concentrations, respectively. Finally, the auxiliary continuity equations are required to determine charge conservation:

$$\frac{\partial n}{\partial t} = -\frac{1}{q} \nabla \cdot J_n - R_n + G_n \quad (2.30)$$

$$\frac{\partial p}{\partial t} = -\frac{1}{q} \nabla \cdot J_p - R_p + G_p \quad (2.31)$$

Here $R_{n(p)}$ is the recombination rate and $G_{n(p)}$ are the recombination and generation rates for electrons(holes). Recombinations and generations, which occur equally for electrons and holes, play significant roles in carrier behavior. As a result, various recombination processes, such as Shockley-Queisser, radiative, and trap-assisted recombination, are modeled. However, due to the limitation of data and simulation tool, Auger recombination was not considered. Using an analytical trap density, unaccounted recombinations are combined into a single recombination process. Both a steady-state and a time-varying form may be

produced by the equations once they have been solved. Steady-state simulations are crucial when examining the system's behavior under a set operating condition. Different boundary condition absorber layer to the dielectric, absorber layer to the reflector, absorber layer to conducting material was considered for calculating the electric property of the cell. The boundary condition of electron and hole velocity for the absorber layer to the passivation layer Si_3N_4 was 1000 cm/s.

The electrical model determines how many photogenerated electron-hole pairs are gathered at the electrical connections and how much of that power is output electrical power. In this step, it will be taken into consideration how the materials' electrical and thermal qualities affect the effectiveness of the collection. The current-voltage parameters of the solar cell, including the short-circuit current (J_{sc}), open-circuit voltage (V_{oc}), fill-factor (FF), and photovoltaic efficiency, can be determined by performing a voltage sweep calculated from (2.16) to (2.19).

Chapter 3

Light Absorption Enhancement by TiN Plasmonic Nanospheres

3.1 Introduction

Nanostructure incorporation is one of the groundbreaking ideas for increasing light absorption in a thin film [84]. The key factor in the enhancement of light absorption by local surface plasmons is the suitable selection of the shape, size, and material of the nanoparticles [96–98].

When the incoming light's natural frequency and the collectively oscillating electrons' natural frequency coincide at a localized surface plasmon resonance, light is preferentially scattered into the absorbing layer by the NPs adorning the solar cell's surface, which enhances free carrier generation [99, 100]. Solar cell efficiency is significantly increased by using plasmonic NPs, which are metallic nanoparticles with plasmon resonances adjusted to effectively scatter light into the absorbing layer [101]. Transition metal nitrides such as titanium nitride can have high electron concentrations, and the actual visible dielectric constants of these metal nitrides are much lower than those of noble metals. TiN NP represents a good candidate that can be integrated into a thin film solar cell for efficient light-trapping because of their ease of manufacture and integration into standard silicon manufacturing processes [17, 102, 103].

In this chapter, we studied the production of plasmonic active substances consisting of TiN nanoparticles embedded in Si with the potential to be used at the absorber layer of thin-film solar cells for improved light trapping and increased light conversion efficiency. It presented the plasmonic properties of TiN by exciting surface plasmon polaritons (SPPs) on these films. We provide a comparative study of the optical performance of TiN-based plasmonic nanosphere with noble metals. We studied the total scattering cross-section, far-

field spectra, and absorption power of different NP materials. We further explored TiN NP with Si_3N_4 coating and calculated absorption cross-section, Q_{ab} and total scattering cross-section, Q_T , Absorption. enhancement by TiN nanoparticles and power-voltage and current density-voltage characteristics were analyzed to determine the impact of TiN NP on the photovoltaic cell.

3.2 Structural Design and Simulation Method

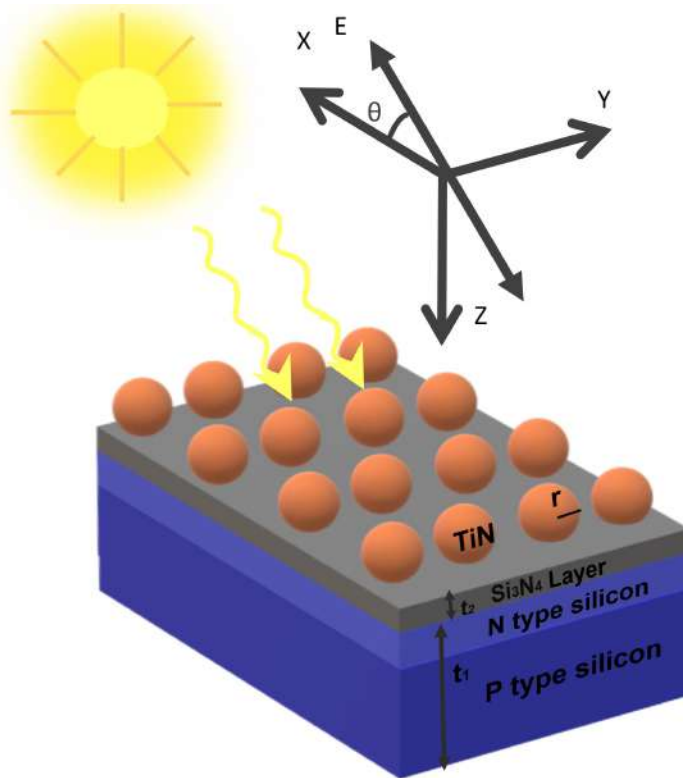


Figure 3.1: Illustration of spherical monomer nanoparticle on a 30 nm thin Si_3N_4 underlayer on p-n Si photovoltaic cell.

3.2.1 Structural Design

Our designed structure consisted of TiN-based nanospheres embedded on the semi-infinite crystalline silicon substrate, as seen in Figure 3.1. The plasmonic particles were separated from the semi-infinite silicon absorption layer by a thin Si_3N_4 layer. The Si_3N_4 has great performances as a passivation layer dielectric material alongside SiO_2 and TiO_2 as determined by a defined figure of merit, which takes into consideration both the optical and thermal properties of the dielectric material [104]. Moreover, the Si_3N_4 layer act as an anti-reflection coating reducing light reflection. TiN NP is ideal for light absorption en-

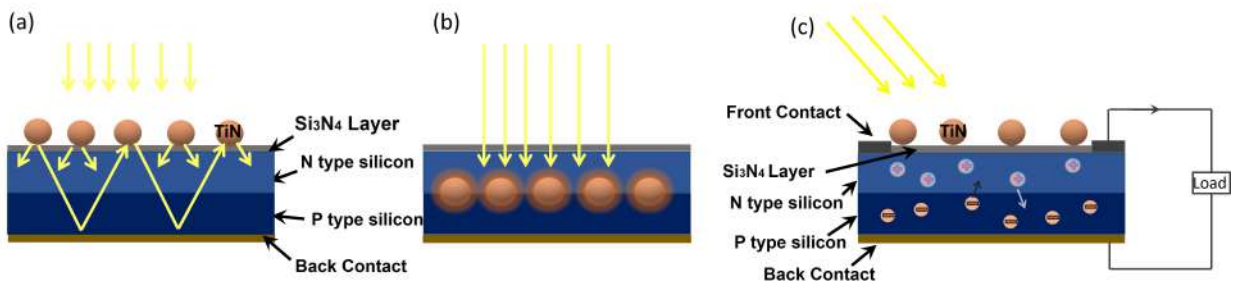


Figure 3.2: (a) Light trapping by scattering from metal nanoparticles at the surface of the solar cell. (b) Light trapping by the excitation of localized surface plasmons in metal nanoparticles embedded in the semiconductor. The excited particles' near-field causes the creation of electron-hole pairs in the semiconductor. (c) Plasmonic NP incorporated p-n junction PV cell.

enhancement of silicon substrates because of its localized surface plasmon impact and higher light absorption and cost-effectiveness compared to noble plasmonic metal. The complex refractive index of the Si, TiN [105] and Si₃N₄ were collected [106] and utilized in this study. Plasmonic NPs can enhance light trapping by scattering the light when placed on the anti-reflecting coating layer, or by electron-hole pair generation through near-field enhancement when placed between N-type and P-type layers. They can result in light trapping as can be seen in Figures 3.2(a)-(b). Figure 3.2(c) presented our designed photovoltaic cell. Figure 3.1 presented the spherical array we designed, Here, r represents the radius of the spherical particles, and the thickness of the thin film and substrate were denoted by t_1 and t_2 , respectively. The polarization angle of the source was represented by θ .

3.2.2 Simulation Methods

Numerical simulations were performed using the FDTD method by Maxwell's equation. The FDTD computational space had characteristic dimensions $1.2 \mu\text{m} \times 1.2 \mu\text{m} \times 1.25 \mu\text{m}$, and a perfectly matched layer (PML) boundary conditions were used in all directions during simulation. A total-field scattered-field (TFSF) plane wave was incident on the particle in the z -axis. The TFSF source was polarized perpendicular to the surface normal on the particle from the air side as the nanoparticles will be at the front face of a solar cell. To study the scattering properties of the nanoparticles, a TFSF source was very useful and it allowed us numerically to separate the incident field from the scattered field. The TFSF source volume comprised both incident field and scattered field, while outside the source volume, all the fields were detected as scattered light. The incident field inside these regions was subtracted from the total field to numerically give the value of scattered fields. We added electric field monitors outside the TFSF box to calculate the scattering spectra of the nanoparticles. The mapping of the near electric field intensity was calculated by positioning

a monitor at the desired spatial point. The electric and magnetic fields around the particle were measured, afterward, we performed a Fourier transform of the time domain electrical field into a frequency domain. This transformation is given by,

$$E(\omega) = \int_{t=0}^{t=T_f} E(t)e^{i\omega t} dt. \quad (3.1)$$

Here, $E(\omega)$ is the electrical field as a function of angular frequency, ω . $t = 0$ is the starting time and T_f is the final time. The radial Poynting vector, $S(\omega)$ is presented by,

$$S(\omega) = \text{Real} \left[\frac{1}{2} \times E(\omega) \times H^*(\omega) \right]. \quad (3.2)$$

Here, $H(\omega)$ is the magnetic field. The scattered powers along +x and +y directions are defined as P_1 and P_2 , respectively, which are given by,

$$P_1 = \int_{y_{min}}^{y_{max}} \int_{z_{min}}^{z_{max}} S_x(y, z, \omega) dz dy. \quad (3.3)$$

$$P_2 = \int_{x_{min}}^{x_{max}} \int_{z_{min}}^{z_{max}} S_y(x, z, \omega) dz dx. \quad (3.4)$$

Here, $S_x(y, z, \omega)$ is the radial Poynting vector in yz plane and $S_y(x, z, \omega)$ is the radial Poynting vector in xz plane. Similarly, we calculated P_3 , P_4 , P_5 , and P_6 along +z, -x, -y, and -z directions. The sum of power detected along all six monitors in the scattered field region was calculated as the total power scattered by the nanoparticle, P_s given by,

$$P_s = P_1 + P_2 + P_3 + P_4 + P_5 + P_6. \quad (3.5)$$

Using the Mie theory, the fraction of light scatter to the substrate, f_{sub} , the total amount of scattered light, and the light absorption in the plasmonic nanoparticles were determined. Absorption cross-section, Q_{ab} and total scattering cross-section, Q_T are calculated based on the localized surface plasmon resonance (LSPR) for NPs at interfaces from (2.1), (2.10) and (2.12). The absorption per unit volume was calculated from the divergence of the Poynting vector as given by,

$$p_{abs} = -\frac{1}{2} \text{real} (\vec{\nabla} \cdot \vec{S}). \quad (3.6)$$

However, divergence calculations tend to be very sensitive to numerical issues. Therefore, the easiest way to calculate absorbed power is,

$$p_{abs} = -\frac{1}{2} \text{real} (i\omega \vec{E} \cdot \vec{D}^*). \quad (3.7)$$

It can be modified as

$$p_{abs} = -\frac{1}{2} \omega |E|^2 \text{imag}(\epsilon). \quad (3.8)$$

Here, D is the electric displacement field, and ϵ is the permittivity. The path length enhancement was calculated from,

$$\text{Path Length Enhancement} = \frac{2d_{av}}{1 - f_{sub}}. \quad (3.9)$$

The factor of 2 was used as the ideal rear reflector was assumed [52]. The effect of diagonal propagation is represented by the factor d_{av} , which is the ratio of the optical path length over one pass of the device to the thickness of the device, averaged over the angular distribution of light. The d_{av} can be determined by performing a weighted integral of $\frac{1}{\cos\theta}$ over the angular distribution of the scattered power, with θ as the angle with the normal [107].

We studied the impact of NPs Q_T , the light scattered into the substrate Q_{sc} , f_{sub} , and Q_{ab} by investigating their structural properties. To comprehend the usefulness of NPs in photovoltaic applications, We studied the far field, power absorption, and enhancement of NPs.

3.3 Effect of Constituent Material of Nanosphere

In the light trapping process, multiple scattering events occur and path length enhancement depends on them [44]. Path length enhancement is an important factor for measuring the effectiveness of light trapping in the absorber layer. The path length enhancement depends on many factors like f_{sub} , the polarization angle of the light propagating through the device. The fraction of light scatter to the substrate is the ratio of power scattered into the substrate and total scattered power. We calculated d_{av} to be 0.4725 for the TiN nanoparticle and $d_{av}=0.635$ for the Ag nanoparticle of 100 nm radius. By calculating the path length of the light coupled out through the front surface after each reflection from the back surface, we can construct a geometric series of average path lengths that yield approximately the maximum path length enhancement from (3.9). We calculated the path length enhancement for 100 nm wavelength of Ag and TiN spherical NPs, which were 2.45 and 2.25, respectively. We compared the f_{sub} of different plasmonic spherical materials. The value of f_{sub} exhibited a greater value for TiN than Ag, Au, and Al for the whole spectrum. The peak value of f_{sub} was 0.5 for the TiN monomer presented in Figure 3.3(a). The source light was normal incident along the negative z-axis and the polarization angle was at 0° along the x-axis. If the light incidents at incident angles other than normal, the optical path length will increase resulting in enhancement of light absorption. The Q_T , Q_{sc} , and Q_{ab} was the highest for TiN monomers (see Figures 3.3(b)-(d)). The peak value of Q_T was 17 W/m^2 and of Q_{ab} was 3.9 W/m^2 for TiN NP and it was greater than that of other NPs.

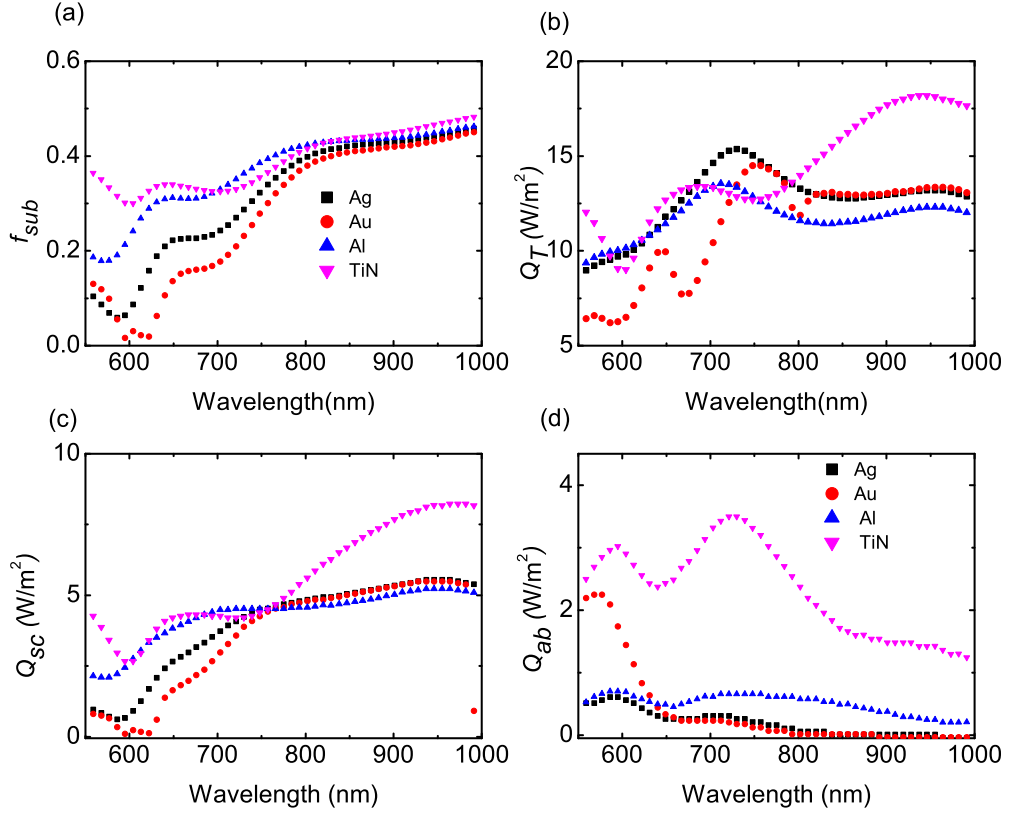


Figure 3.3: (a) f_{sub} , (b) Q_T , (c) Q_{sc} , and (d) Q_{ab} as a function of wavelength for 100 nm radius nanosphere consisting of Ag, Au, Al, and TiN on a 30 nm thick Si_3N_4 underlayer on Si substrate.

The near field and far field are regions of the electromagnetic (EM) field transmitting and scattering off around an object [108, 109]. At increasing distances, far-field characteristics predominate over electromagnetic radiation. When the electric and magnetic fields for the localized oscillating source are solved using Maxwell's equations, the results show field levels that degrade according to the source's distance, d . The far-field consists of the radiating fields and the area where d is large enough for these fields to dominate. The far field is dominated by transverse electric or magnetic fields with electric dipole properties. Radiated power drops in the far-field zone as the square of the distance, and radiation absorption does not feed back to the transmitter. The far-field spectra for different materials at the central location are presented in Figure 3.4. The far field is presented in this polar plot by θ at a wavelength of 680 nm. Here, 0° and 90° were the x-polarized and y-polarized light. The TiN nanoparticle had the highest far-field distance $d = 33.14$ nm and Al had the lowest far-field distance $d = 25.62$ nm. The far-field wave shape is more planar than the near-field.

We calculated the power absorbed for the bare absorber layer and after adding each layer in each of the optimized plasmonic Ag, Au, Al, and TiN nanospheres incorporated cells, as presented in Figure 3.5. Here $t_1=10$ nm and $t_2=250$ nm, as we calculated the optical property. No back reflector was used under the silicon layer. To avoid reflection at the top

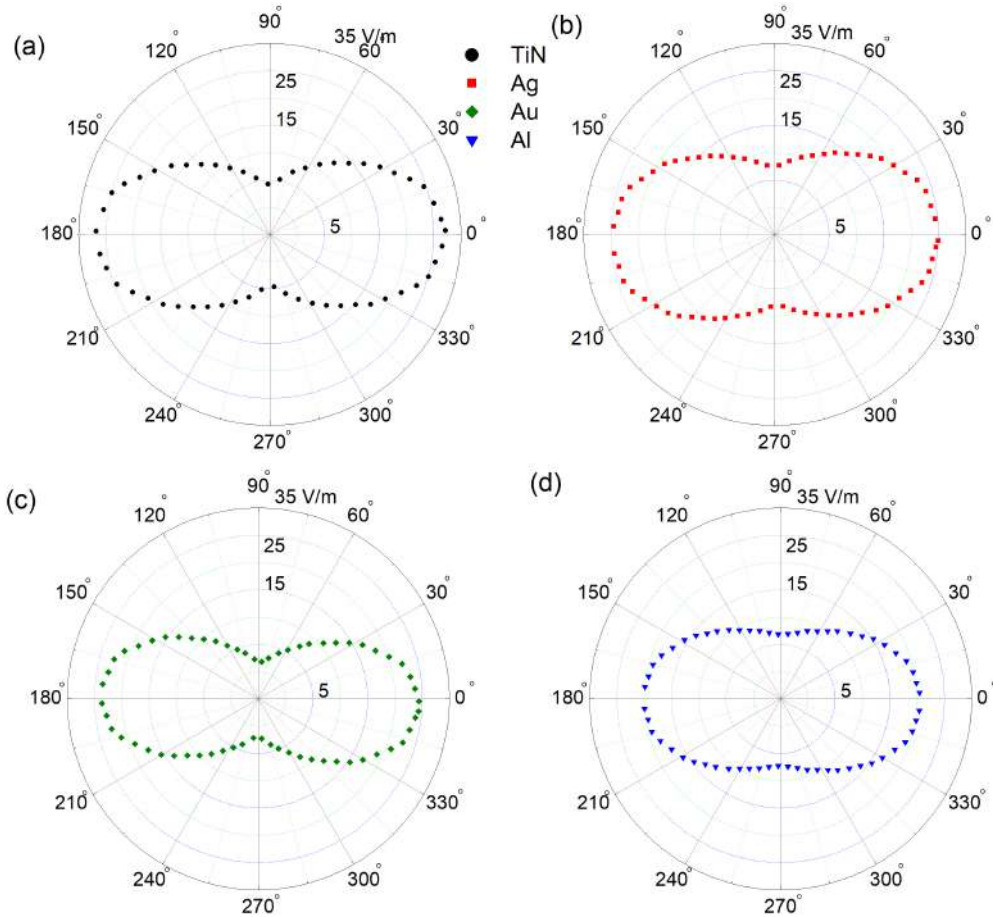


Figure 3.4: Polar plot for far-field spectra in xy plane depending on incident light for the 100 nm radius nanosphere consisting of (a)TiN(b)Ag, (c) Au, and (d) Al at 680 nm incident wavelength.

boundary, the PML condition was utilized. Moreover, PML was used at the bottom of Si layer. As a result, Fabry-Perot interference did not occur, and no oscillations were observed in the absorption power spectra. The absorption per unit volume can be calculated from the divergence of the Poynting vector. Silicon had average absorption power $\sim 19\%$ for the spectral range 400 nm to 1000 nm. The enhancement due to the addition of the Si_3N_4 layer is negligible, mainly observed in the 400-500 nm spectral range. As seen in Figure 3.5, the absorbed power for TiN was higher than those of Ag and Al. Compared to Au, TiN had greater absorbed power for 600 nm to 1000 nm. It was evident that TiN efficiently absorbed light for monomer shape, and the average absorbance power increased to $\sim 45\%$ for 400 nm to 1000 nm after adding TiN NP.

3.4 Exploring TiN NP and Core-shell TiN NP

Color map showing the xy, zx, yz distribution of $|E|$ for TiN nanosphere placed on top of thin Si_3N_4 on a Si substrate presented in Figures 2.10(a)-(c). These structures can create LSPR

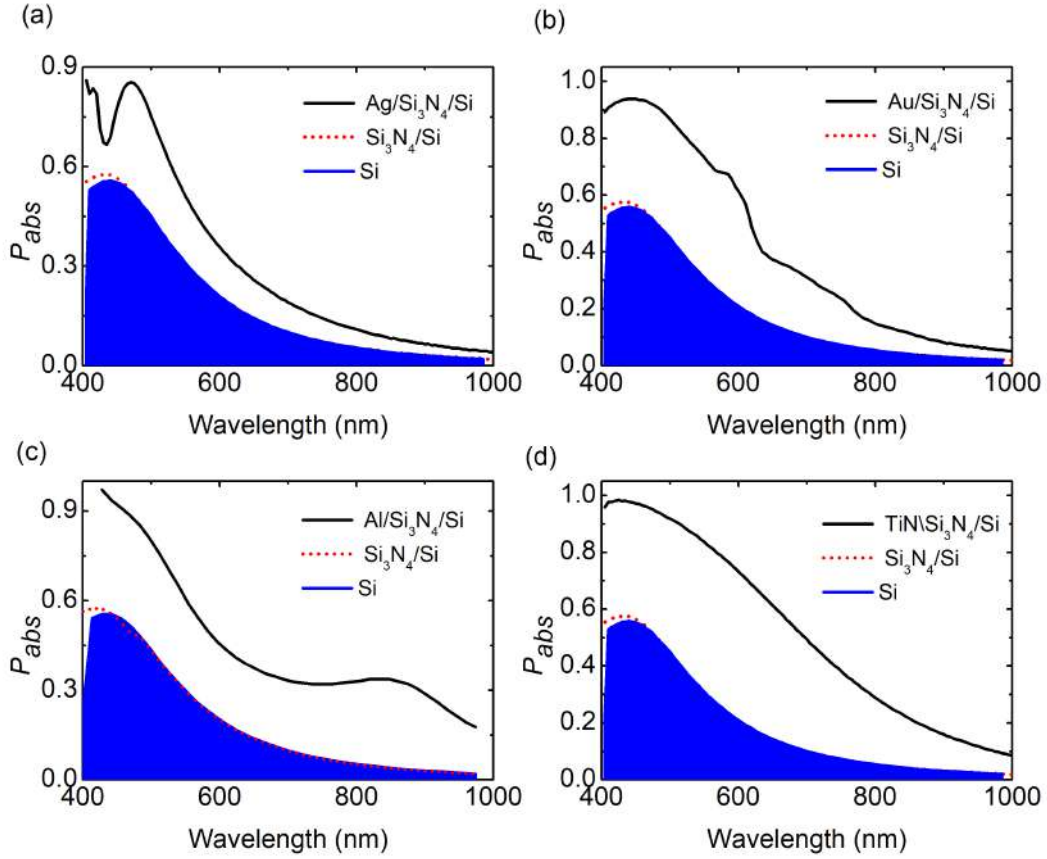


Figure 3.5: Percentage of power absorbed after addition of each layer of (a) Ag, (b) Au, (c) Al, (d) TiN NP incorporated Si absorber layer solar cells.

where free charges accumulate precisely at the sphere's surface [110]. In the xy plane at $z = 0$ free charge accumulation resulted in E-field enhancement and the charge density scatter along the surface as can be seen in Figure 2.10(a). Charge density accommodated strong surface plasmon coupling resulting in high charge distribution along the x direction. Electric field enhancement was observed along the x -direction, and there was no electric field enhancement along the y -direction, which was consistent with previous reports [57, 103]. In the zx plane at $y = 0$, charge accumulated along the surface of the sphere. However, the bottom of the sphere electric field enhancement was negligible. Electric field enhancement was highly observed along the upper side of the sphere in the zx plane. In the yz plane at $x = 0$, the charge accumulated, and electric field enhancement was observed. For the whole yz plane. charge accumulation resulted in strong surface plasmon coupling resulting in charge distribution equally around the sphere's surface.

We determined the performance of NPs comprised of various materials such as Au, Ag, Al, and TiN. And TiN was found to be a perfect candidate as alternative plasmonic material. Here, our main idea was to enhance the efficiency of TiN NP; therefore, we explored a core-shell configuration consisting of 80 nm radius TiN NP with 20 nm Si_3N_4 coating. In our

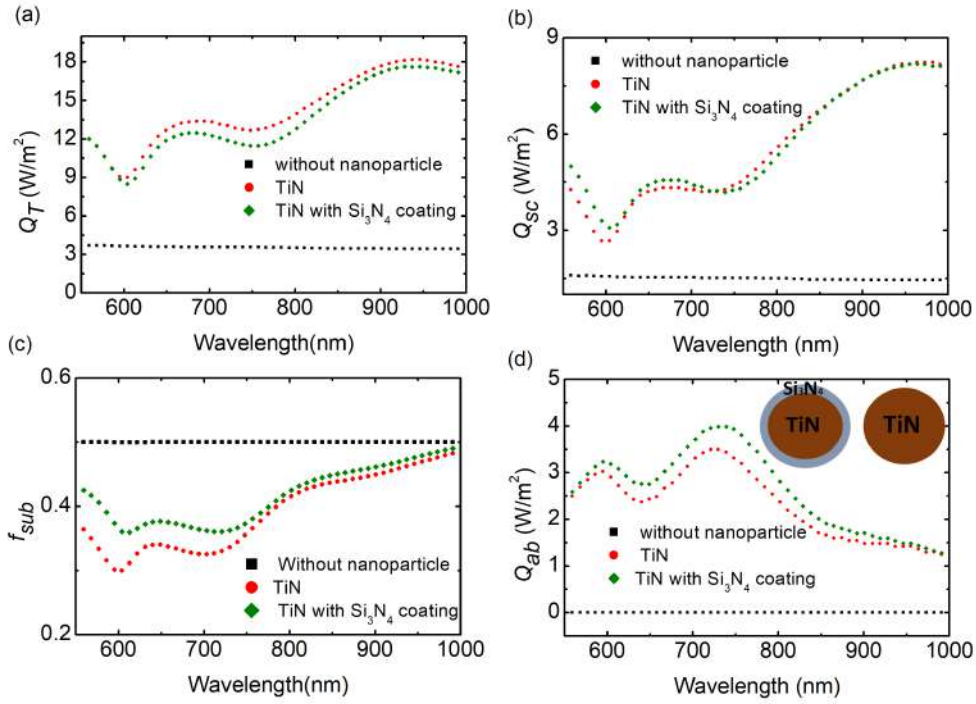


Figure 3.6: (a) Q_T (b) Q_{sc} (c) f_{sub} (d) Q_{ab} as a function of wavelength for 100 nm radius nanosphere no plasmonic NP, TiN NP, and TiN core with Si_3N_4 coating NP on a 30 nm thick Si_3N_4 underlayer on Si absorber layer.

photovoltaic system, we calculated the absorption across the nanosphere and the f_{sub} . As can be seen from Figure 3.6(c), the TiN had better f_{sub} when it is coated with Si_3N_4 compared to the TiN nanosphere. When the nanosystem was without plasmonic NPs, total scattering and scattered to the substrate decreased, but the ratio increased, hence f_{sub} increased. It can be seen from Figures 3.6(a)-(b) that the TiN NP had a better-scattering cross-section than the TiN core-shell NP. However, TiN sphere and TiN core-shell NPs had almost the same Q_{sc} value. As can be seen from Figure 3.6(d), the TiN shell surrounded by Si_3N_4 layer had better absorption than the TiN nanosphere [103]. The nanosystem performed poorly for scattering and absorption without TiN NPs.

We calculated the absorbed power of bare silicon Nanostructure. Afterward, we added our preferred TiN NPs to the nanosystem. As shown in Figure 3.7(a), the percentage of power absorbed increased largely. As there was no efficient change for longer wavelengths, we considered the observation from 400 nm to 1000 nm. The power absorption increased from $\sim 19\%$ to $\sim 45\%$ after the addition of TiN NP and further increased to $\sim 53\%$ after the replacement of TiN NP with core-shell NP for the 400 nm to 1000 nm wavelength. We calculated absorption enhancement, g for the different radii of TiN plasmonic dimer on a silicon substrate, as seen from Figure 3.7(b). The g decreased with the increase of r for wavelength 400 nm to 600 nm. This occurred due to the low absorption and strong forward scattering of light by plasmonic NPs. The forward scattering enhanced absorption, whereas

the backward scattering prohibited absorption. Spherical plasmonic NPs with larger radii usually have a larger cross-section area of scattering. For $r = 15$ nm, the absorption was greater than 1 for the whole wavelength range. For wavelengths longer than 600 nm, the g became greater than 1 for $r = 50$ nm. Similarly, g increased for all the radii of TiN plasmonic nanospheres for wavelengths longer than ~ 800 nm.

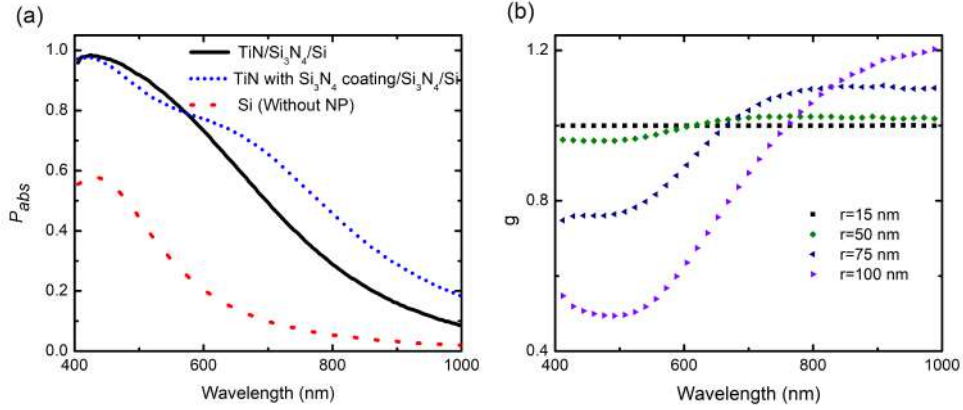


Figure 3.7: (a) Power absorbed in TiN and TiN core with Si₃N₄ coating NPs incorporated Si absorber layer for solar cells. (b) Absorption enhancement, g for TiN plasmonic nanosphere with different radii.

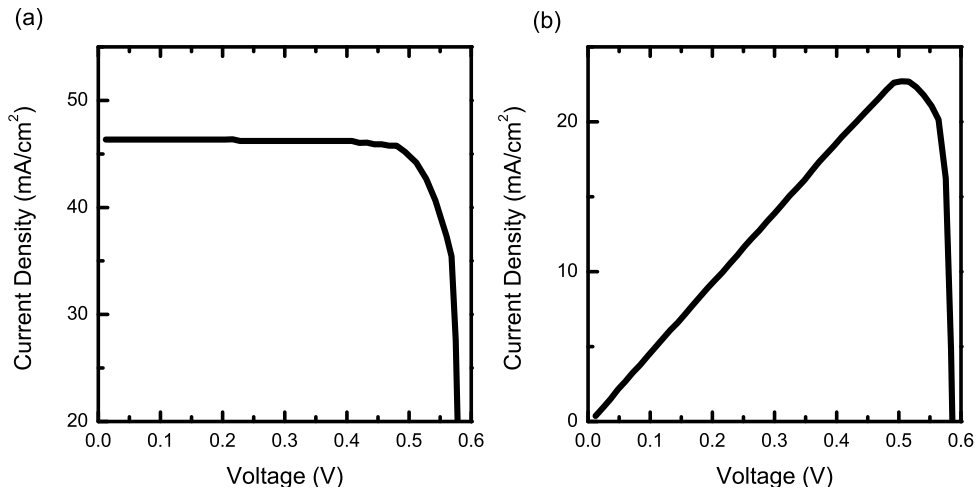


Figure 3.8: (a) power-voltage and (b) current density-voltage characteristic of 100 nm TiN monomer on si substrate layer.

We calculated power-voltage and current density-voltage characteristics for 100 nm TiN sphere on Si as shown in Figure 3.2(c). The electrical performance of the cell was calculated from (2.16) to (2.19) was presented in Figure 3.8. The maximum power, P_{max} can be calculated from Figure 3.8. The open circuit voltage, V_{oc} , short circuit current, J_{sc} can be seen from Figure 3.8(b). The calculated results are $V_{oc}=0.586$ V, $J_{sc} = 46.59$ mA/cm², $P_{max} = 22.62$ mW/cm², fill factor, $FF = 0.829$ and $\eta = \sim 22.62\%$. Adding TiN NP on Si with Si₃N₄ antireflecting coating improved the PV cell efficiency significantly.

Chapter 4

Light Trapping Using TiN Dimer of Spherical Nanoparticles

4.1 Introduction

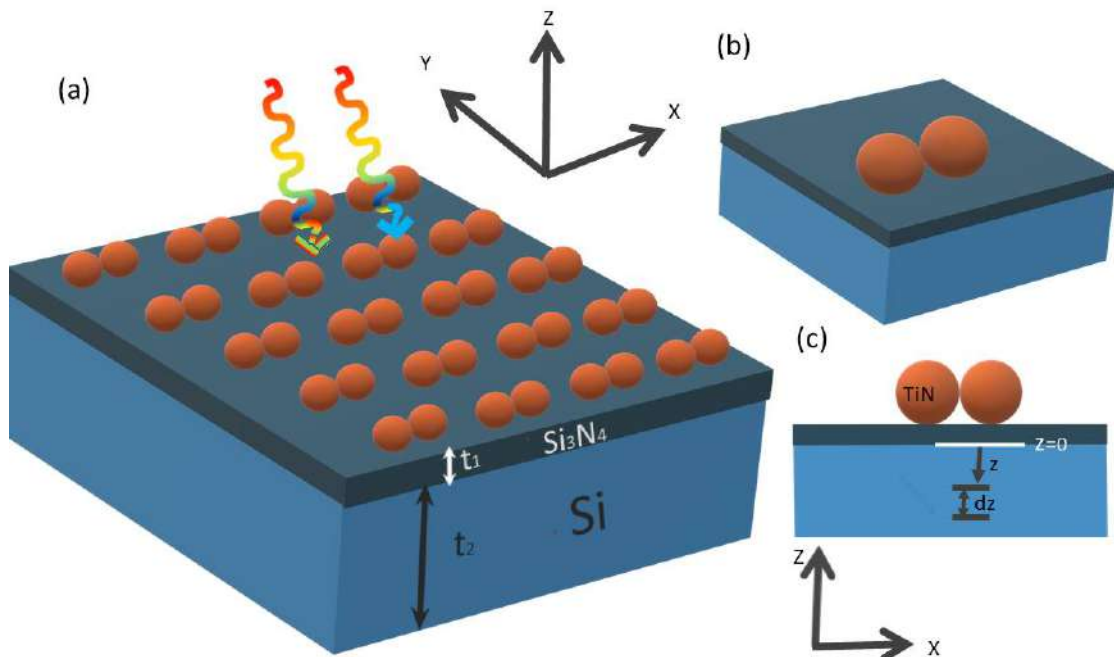


Figure 4.1: (a) Illustration of spherical dimer TiN nanoparticle on a 30 nm thin Si_3N_4 underlayer on Si substrate acting as the absorber layer of the photovoltaic cell. (b) Perspective view and (c) cross-sectional view of a single dimer of spherical nanoparticles.

In this chapter, we systematically investigate the scattering cross-section and absorption enhancement by spherical dimer TiN NPs for photovoltaic application. First, we designed and optimized the dimer of the spherical NPs to determine the total scattering cross-section, fraction of light scattered into the substrate, absorption cross-section, and spatial mapping of

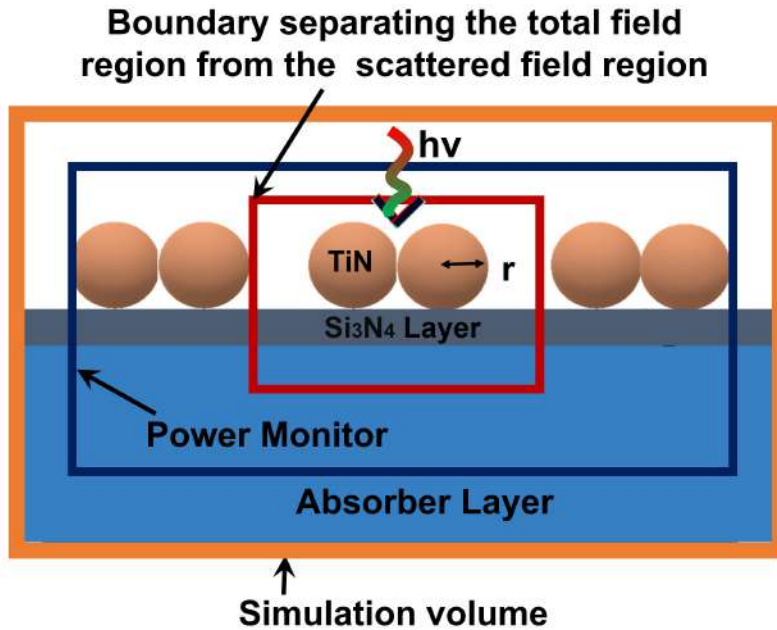


Figure 4.2: A cross-section of the simulation setup. Light from the source was incident on the particle in the negative z-direction.

the electric field in this plasmonic nanosystem. We further investigated the effect of polarization sensitivity on the source. We gained insight into how the shape of the NPs improved the performance of solar cells when the NPs were embedded into them. We investigated plasmonic core-shell configuration and analyzed the effect of dielectric coatings on NPs. Our study provided insights into using TiN in photovoltaic cells.

4.2 Structural Design and Simulation Methods

4.2.1 Structural Design

We designed an alternative plasmonic material, TiN-based spherical dimer NP on a semi-infinite crystalline silicon substrate, as can be seen in Figure 4.1. A cross-section of the TiN-based dimer-shaped nanosphere simulation setup was represented in Figure 4.2. Here we analyzed TiN dimer NPs comprised of 30 nm thin Si₃N₄ passivation layer on si substrate. TiN exhibits localized surface plasmon phenomenon and metallic properties in the visible and longer wavelengths [16, 17]. The plasmonic particles were separated from the semi-infinite silicon absorption layer by thin Si₃N₄ layer as surface passivation. We compared cross-sections of NPs based on conventional noble plasmonic metal with TiN alternative plasmonic NPs. The complex refractive of the Si, TiN [105] and Si₃N₄ were collected [106] and utilized in this study. To compare the performance of TiN with other noble metals the physical property of Ag, Au, and Al [105] were also used. The size of the particles

was varied, and their properties were analyzed. The thin film and substrate thickness were presented by t_1 and t_2 , respectively. The polarization angle of the source was represented by θ , r represented the radius of the sphere, and d represented the distance between the nanospheres of a dimer.

4.2.2 Simulation Methods

We applied the FDTD method based on Maxwell's equations, The simulation dimensions of the FDTD were $1.2 \mu\text{m} \times 1.2 \mu\text{m} \times 1.25 \mu\text{m}$. A mesh size of 0.4 nm was applied around the NPs. The source was adjusted for polarization perpendicular to the surface normal of the particles from the air side. The total-field scattered-field (TFSF) plane wave was incident to the particles along the z -axis. The incident source was a uniform wave with wavelengths predominantly between 550 and 1100 nm. To analyze the optical properties of NPs, a plane wave with a TFSF was used to separate the incident field from the scattered field. An external monitor was used to study the scattering properties. The spatial electric field mapping was performed by adjusting a frequency-domain power monitor. We used light scatterers to increase the light trapping efficiency, which improved the absorption in the absorber layer. We calculated the scattering and absorption cross-sections, and optimized values were achieved by varying different parameters for improved PV application. The electric and magnetic fields around the particle were measured by performing a Fourier transform of the time domain into a frequency domain. The radial Poynting vector, $S(\omega)$, was calculated from (3.2) and the electric field, $E(\omega)$ was calculated from (3.1) as a function of angular frequency, ω . The sum of power, P_s was calculated from (3.5) along $+x$, $+y$, $+z$, $-x$, $-y$, and $-z$ directions in the scattered field region calculated from (3.3). The total power per unit area scattered in all directions divided by the power per unit area of the incident beam is defined as the total scattering cross-section, $Q_T(\omega)$ and it can be calculated from,

$$Q_T(\omega) = \frac{P_s(\omega)}{I(\omega)}. \quad (4.1)$$

Here, $I(\omega)$ is incident power intensity with unit W/m^2 . Absorption cross-section is a measure of the probability of an absorption process. The total absorbed power divided by the power per unit area of the incident light was defined as absorption cross-section, Q_{ab} . It can be calculated from (2.11). dN/dz is the number of photons absorbed between the points z and $z+dz$, N is the number of photons penetrating to depth z , and n is the number of absorbing molecules per unit volume. The scattering cross-section is calculated by the monitors located outside the TFSF source [52, 111]. The absorption per unit volume with the incorporation of each layer was calculated from (3.6) to (3.8). The light absorption efficiency (LAE) was calculated by,

$$\text{LAE} = \frac{\int_{400}^{1100} I(\lambda)A(\lambda)d\lambda}{\int_{400}^{1100} I(\lambda)d\lambda}. \quad (4.2)$$

Here, $I(\lambda)$ is the incident solar light intensity AM 1.5 G. And, absorbance, $A(\lambda)$ was calculated by,

$$A(\lambda) = 1 - R(\lambda) - T(\lambda). \quad (4.3)$$

Here, $T(\lambda)$ and $R(\lambda)$ are the transmittance and reflectance of the structure. As the effective cross-sections changed for the region 400 nm to 1100 nm, we considered LAE for 400–1100 nm.

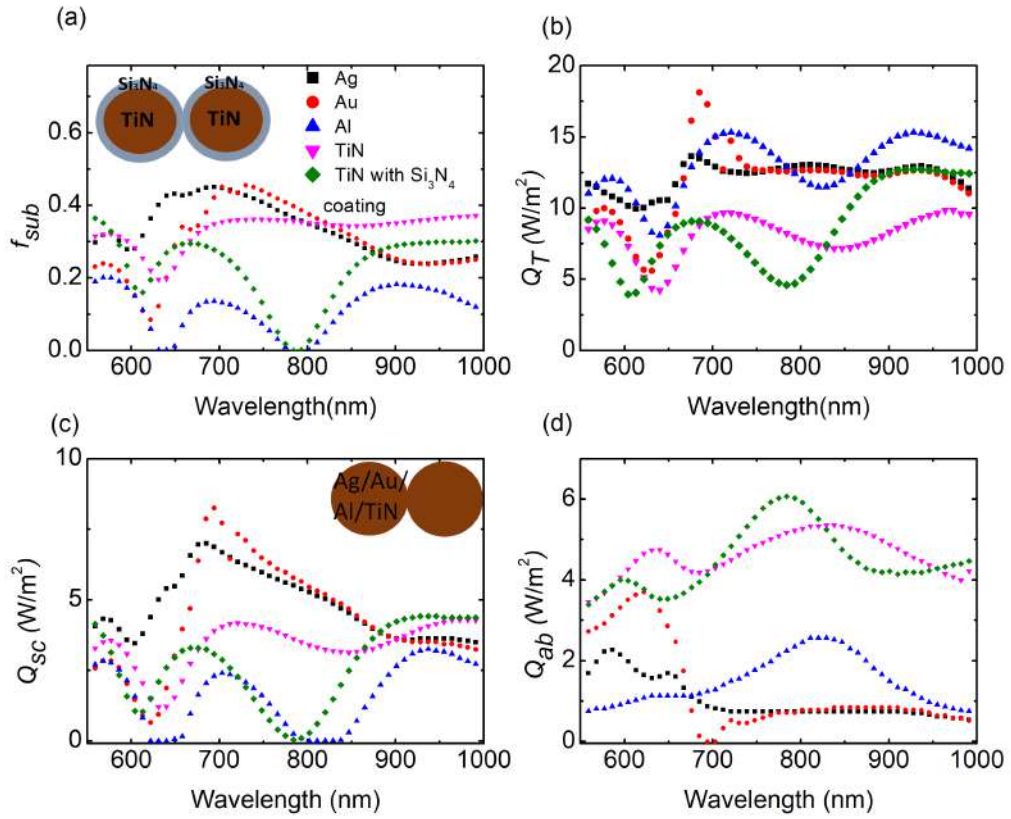


Figure 4.3: (a) f_{sub} , (b) Q_T , (c) Q_{sc} , and (d) Q_{ab} as a function of wavelength for 100 nm radius dimer NPs consisting of Ag, Au, Al, TiN, and TiN with Si₃N₄ coating on a 30 nm thick Si₃N₄ underlayer on Si substrate.

We methodically considered the impact of NPs' Q_T , the light scattered into the substrate Q_{sc} , the fraction of light scattered into the substrate, f_{sub} , and Q_{ab} by investigating their structural properties. We compared the effects of alternative plasmonic NPs to plasmonic metals and comprehensively considered the capacity to enhance absorption within an absorber layer by adding NPs. Moreover, to demonstrate the effectiveness of the dimer NPs in PV cells, we calculated the designed structure's absorption enhancement and light absorption efficiency.

4.3 Results and Discussion

4.3.1 Effect of Different Material-Based Plasmonic Spherical Dimer Nanoparticle

We simulated spherical dimer NPs for different materials and tracked their scattering and absorbance behavior. Here, t_1 , t_2 , and r were regarded as 30 nm, 250 nm, and 100 nm, respectively. We evaluated the performance of NPs made of different materials, including Au, Ag, Al, and TiN. Moreover, we explored a core-shell configuration consisting of TiN NP with Si_3N_4 coating to maximize the performance.

The foremost critical factor representing the path length enhancement of a scattering light-trapping structure is f_{sub} [112]. As can be seen in Figure 4.3 (a), the overall f_{sub} exhibited $\text{Ag} > \text{Au} > \text{TiN} > \text{TiN with Si}_3\text{N}_4 \text{ coating} > \text{Al}$ in this order. For 800 nm to 1100 nm wavelength, the f_{sub} of TiN NP was greater than those for Ag, Au, and Al-based NPs. When we varied the dimer materials, the peak value of Q_T was 19 W/m^2 for Au NP, and the values for Ag and Al were comparable to Au. TiN NP had comparable values of Q_T and Q_{sc} from 650 to 1000 nm wavelength. After adding Si_3N_4 coating on TiN NP the Q_T and Q_{sc} performed better for 850 to 1000 nm as can be seen Figure 4.3(b)-(d). For scattering applications, Si_3N_4 coating can be used for TiN NP. Q_{ab} increased for TiN and TiN with Si_3N_4 coating NPs. The Q_{ab} was negligible for Ag, Au, and Al NPs.

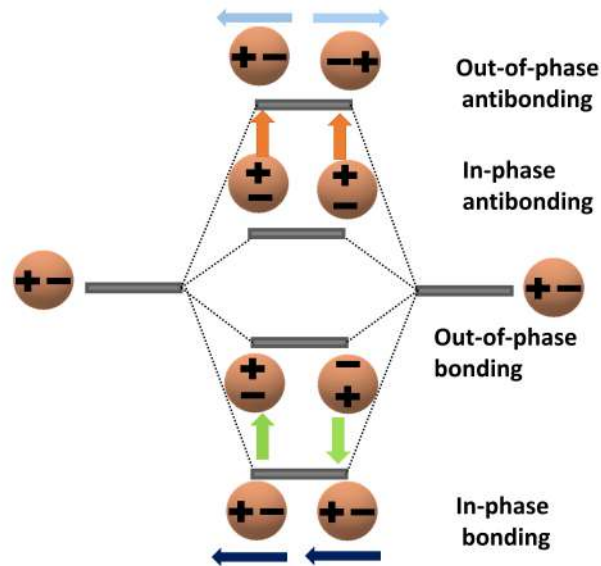


Figure 4.4: Schematic of the LSPR plasmon modes for NP dimers. The coupling of the dipoles in the two spheres of the dimer, created by the plasmon, can occur in the direction of the dimer axis or perpendicular to it.

When a plane wave collides with an object or scatterer, its energy is diverted in all directions. It is crucial to analyze the optical properties of NPs, including scattering cross-section

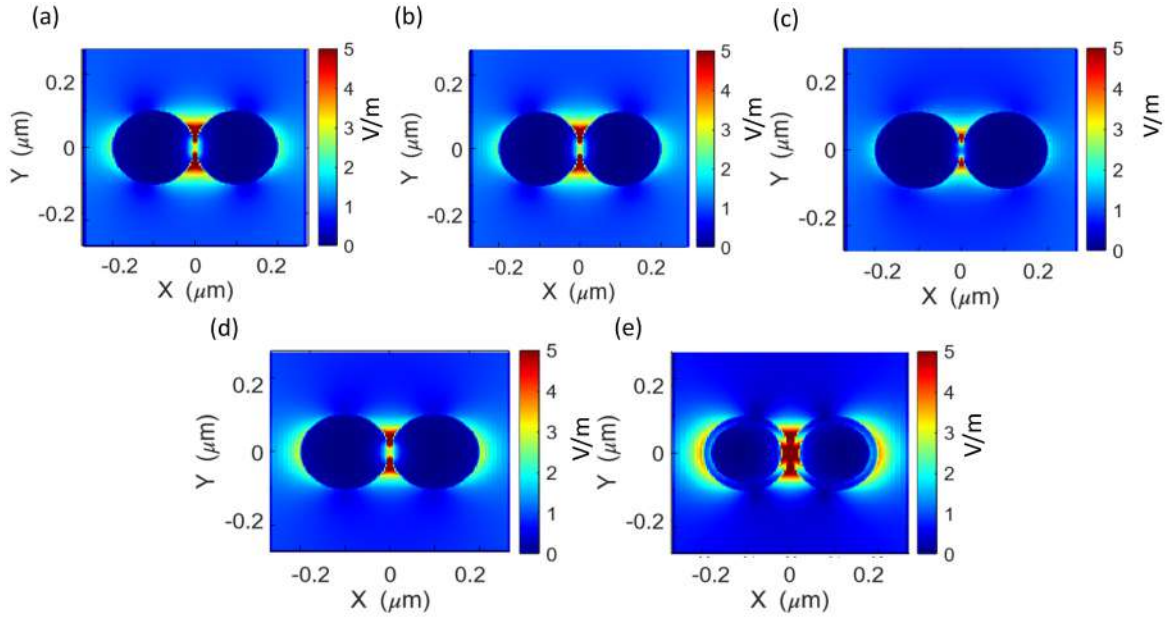


Figure 4.5: Color map showing the xy distribution of $|E|$ for (a) Ag, (b) Au, (c) Al (d) TiN (e) (d) TiN with Si_3N_4 coating dimer NP placed on top of a 30 thin Si_3N_4 on a Si substrate.

and electric field distribution. LSPR modes can be produced by these structures. The plasmonic NP dimers are the equivalent of two atoms sharing electrons by bonding molecular orbitals. The plasmon hybridization model of electromagnetic interaction between plasmonic nanoparticles predicts the emergence of lower energy "bonding" and higher energy "anti-bonding" modes, which is consistent with the quantum mechanical explanation of chemical bonding. In the hybridization model, optically permitted in-phase coupling of the dipole moments is predicted to produce bright "modes" for a metallic nanoparticle dimer excited by linearly polarized light, whereas out-of-phase coupling is predicted to be dark due to the cancellation of the dipole moments with the oppositely oriented orientations (in the quasistatic approximation). These brilliant modes are electric dipolar in nature and easily couple to scalar beams of light, such as those that are linearly or circularly polarized. A dimer's excited dipoles on its two spheres may couple in the direction of the dimer axis, which is analogous to σ -type orbital for atoms or perpendicular to it, which is analogous to π -type orbital for atoms. Four additional plasmon modes emerge for dimers, which are homonuclear diatomic molecules equal to molecular hydrogen (H_2), nitrogen (N_2), oxygen (O_2), or a halogen (X_2) [113]. When the charge of the dimers oscillates in the same direction, the charge accumulates, and electric field enhancement is observed. This phenomenon occurs both in bonding mode and anti-bonding mode, and they are in-phase antibonding with the highest energy and in-phase bonding with dipolar plasmon mode with the lowest energy (highest wavelength) (see Figure 4.4). Additionally, when the charge oscillates in different directions, there is no field enhancement, which is out-of-phase bonding and antibonding modes [110].

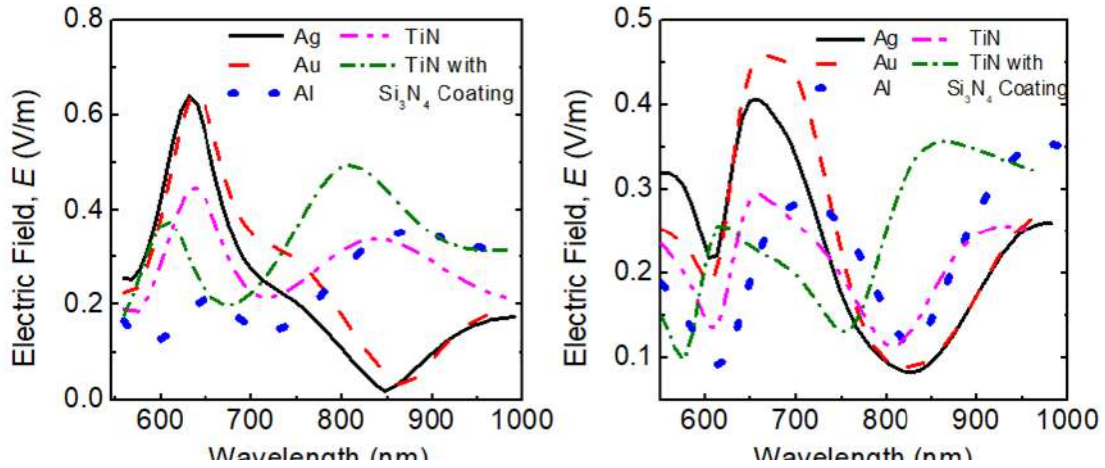


Figure 4.6: The E-field spectra at (a) yz, and (b) xy plane for spherical dimer NPs comprised of different materials placed on top of a 30 thin Si_3N_4 on a Si substrate.

As demonstrated in Figure 4.4, The in-phase bonding creates a bonding state with a red-shifted resonance when the incident beam is polarized along the dimer axis (Figure 4.4 parallel-in same direction navy blue arrows), and the out-of-phase bonding creates an anti-bonding state with a blue-shifted resonance (Figure 4.4, oppositely directed sky color arrows). When polarization is perpendicular to the dimer axis, the situation is exactly the opposite. In contrast to the out-of-phase bonding with red-shifted resonance, which is a "bonding" state (Figure 4.4, green arrows in opposite direction), the in-phase bonding is an "antibonding" state with a blue-shifted resonance. The bonding mode has a lower energy after coupling while the antibonding mode has a larger energy. Additionally, for polarization parallel to the dimer axis, the coupling is weaker. Therefore, in-phase bonding, out-of-phase bonding, in-phase antibonding, and out-of-phase antibonding, in that order from lower to higher energy, can result from plasmon coupling of a symmetric dimer. Due to the canceling of the opposing oriented dipole moments in near-field proximity and disregarding retardation, localized plasmon illumination of a symmetric dimer only permits excitation of in-phase bonding which is an x-polarized or antibonding state which is the y-polarized state.

By changing the spherical dimer NPs' material, shown in Figure 4.5 electric field maps in the xy plane were detected. The in phase bonding was observed in Figures 4.5(a)-(c), the light mode was observed due to electric field enhancement and the enhancement was negligible in the y direction. The electric field enhancement was more prominent for Ag and Au than Al. As can be seen in Figures 4.5(d)-(e), the scattering spectra TiN and TiN with a dielectric Si_3N_4 coating exhibited an unprecedented homogeneity for the two spheres. The in-phase bonding plasmon mode was observed for x-polarized light The induced dipole moments resulted in two bright modes. Therefore, the accumulation of high free charge distribution around the surface and center of the dimer resulted in the enhancement of the electric field.

The quasistatic dipole approximation was used to compute the electric field (E) enhance-

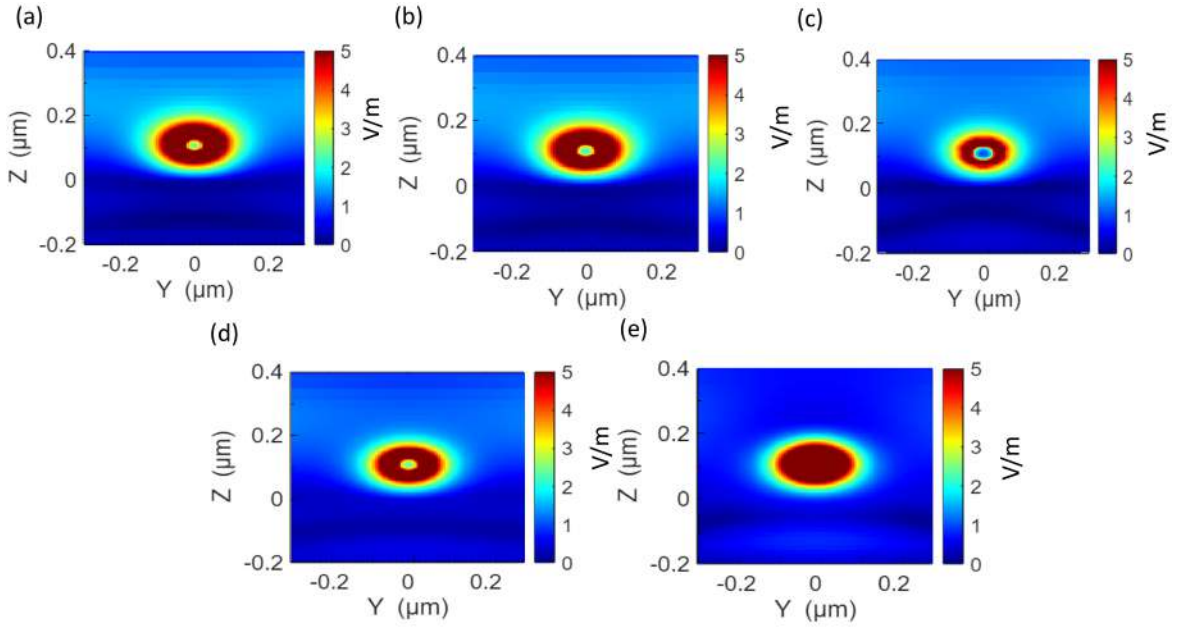


Figure 4.7: Color map showing the yz distribution of $|E|$ for (a) Ag, (b) Au, (c) Al (d) TiN (e) TiN with Si_3N_4 coating dimer NP placed on top of a 30 thin Si_3N_4 on a Si substrate.

ment at yz and xy plane around the surface of Ag, Au, Al, and TiN dimers were presented in Figure 4.6. Due to a lower real permittivity than Ag and Au, the magnitude of the magnetic field enhancement in TiN nanospheres was slightly smaller than those of Ag and Au. E-field intensity on the yz plane at $x = 0$, which is the center of the dimer, can be seen in Figure 4.7 for different material-based dimer nanosphere. For Ag and Au and TiN with Si_3N_4 coating, charge distribution was high at the center of the dimers as presented in Figures 4.7(a), (b) and (e). For Al and TiN, charge distribution at the center was less as compared to Ag and Au, as can be seen in Figures 4.7(c) and (d). Here, the charge oscillates in the same direction, so the charge accumulated and field enhancement occurred. Resulting LSPR modes were utilized in numerous detection applications [17]. The LSPR mode of TiN with Si_3N_4 coating in the core-shell configuration was blue-shifted, and the peak value of the electric field increased compared to the bare TiN dimer.

The range of electromagnetic energy that the sun emits, from the ultraviolet to the infrared spectrum, is known as the solar spectrum. It is made up of photons with different wavelengths, which determine the pattern and intensity of the spectrum. It can be explained using solar irradiance or solar radiation. Solar irradiance is the quantity of energy that reaches the Earth's surface, whereas solar radiation is the energy that the sun directly emits. The ultraviolet (UV), visible, and infrared (IR) spectrum of the sun can be split into three primary categories. Light with a wavelength of less than 400 nanometers (nm) is considered to be UV light. The energy of UV photons ranges from about 3 to 5 electron Volts (eV). The visible spectrum spans 400 to 700 nm.

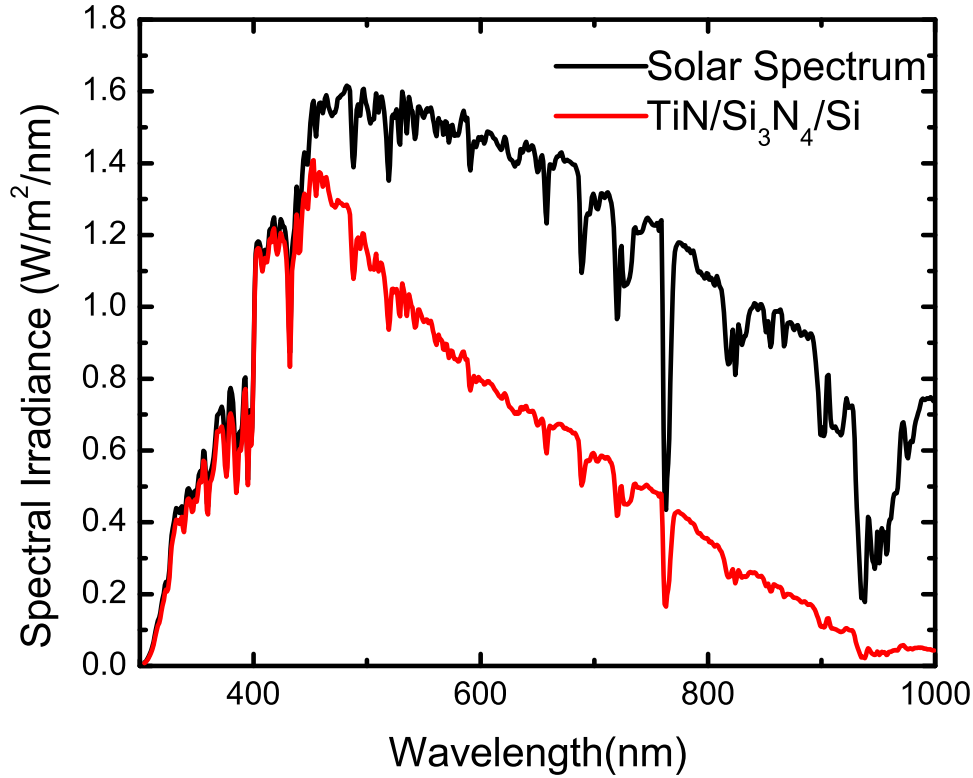


Figure 4.8: Absorption spectra of TiN dimer NP incorporated Si absorber layer and Solar irradiance spectra.

Photons in this area have energy between 1.8 and 3 eV. The IR area consists of light with wavelengths greater than 1000 nm and photon energies ranging from roughly 0.35 eV to 1.8 eV. The Earth-Sun distance, the angle at which the sun's rays enter the Earth's atmosphere, the weather, and the level of air pollution all have a significant impact on the intensity of the solar spectrum that is received on Earth. Sun cells are particularly sensitive to the shape of the sun's spectrum and the strength of the radiation because they use photovoltaic technology to convert solar radiation into electricity. Therefore, in order to produce as efficient as possible solar cells, researchers and engineers work on the solar spectrum. Therefore, when building and developing solar cells, it is crucial to take the solar spectrum into account. Standard 1.5 ATM solar spectrum and absorption of TiN NP-based solar cell are presented in Figure 4.8. Solar light absorption is very efficient for wavelengths from 300 nm to 500 nm. For longer wavelengths than 500 nm, the absorption decreased gradually.

To determine the effectiveness of the NP in the photovoltaic cells, we calculated the absorbed power of each layer of nanostructure consisting of dimer spherical NPs on a 30 nm thin Si_3N_4 underlayer on Si substrate. NPs were comprised of Ag, Au, Al, and TiN. The absorption was calculated from (3.6) to (3.8). Silicon had an average absorption power of $\sim 51\%$ over the 400-500 nm range and $\sim 19\%$ for the whole spectral range as presented in

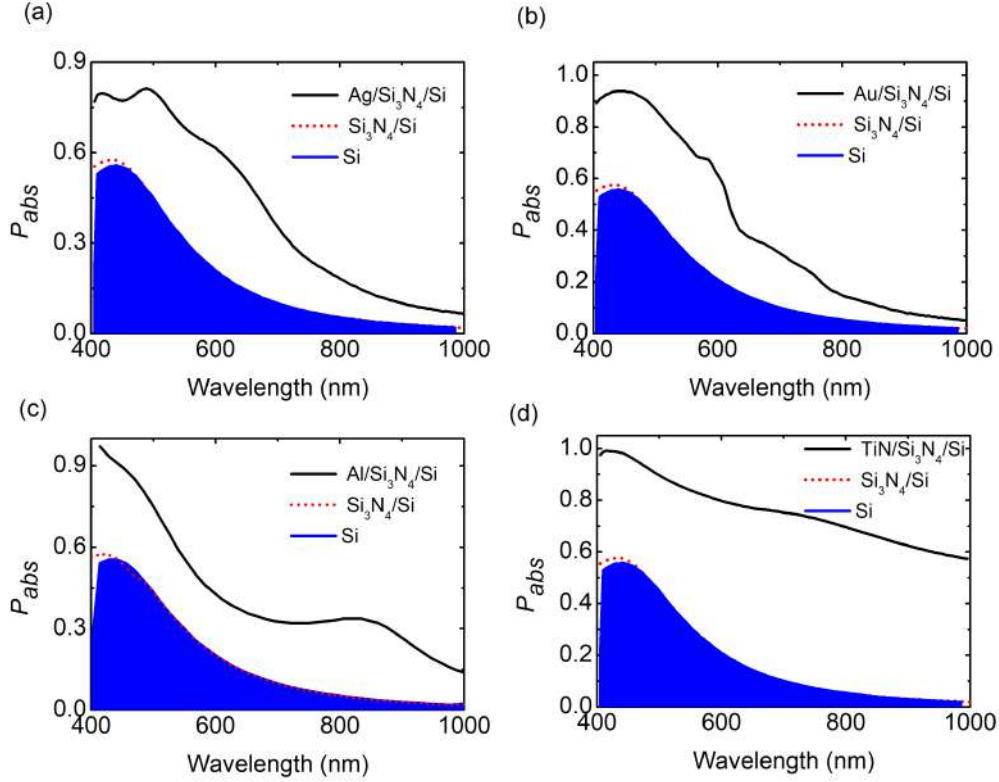


Figure 4.9: Percentage of power absorbed for (a) Ag, (b) Au, (c) Al, (d) TiN NP incorporated Si absorber layer for solar cells.

Figure 4.9. The Si_3N_4 layer enhanced the absorption for the 400-500 nm spectral range. After the incorporation of TiN NPs, the absorbed power increased significantly to $\sim 75\%$ over the whole spectral range as presented in Figure 4.9(d). In comparison to Ag, Au, and Al NPs, TiN NP integration had a substantially higher absorption power.

4.3.2 Absorption Enhancement by TiN-Based Dimer NP

The absorption enhancement defines the increased absorption by the addition of NPs in the solar absorber layer. The absorption enhancement spectrum, g was presented by,

$$g(\lambda) = \frac{EQE_{np}(\lambda)}{EQE_{bs}(\lambda)}. \quad (4.4)$$

Here, EQE_{np} is the device's external quantum efficiency when plasmonic nanoparticles were incorporated on top of a substrate and EQE_{bs} is the external quantum efficiency of a bare substrate. In this section t_1 , and t_2 were taken to be 30 nm and 250 nm, respectively, in this section. We simulated the spectra of g for Ag, Au, Al, and TiN plasmonic dimers on a silicon substrate for $r = 15$ nm, 25 nm, and 30 nm presented in Figures 4.10(a)-(c). TiN exhibited better absorption than Ag, Au, and Al dimers for $r = 15$ nm. For $r = 25$ nm the

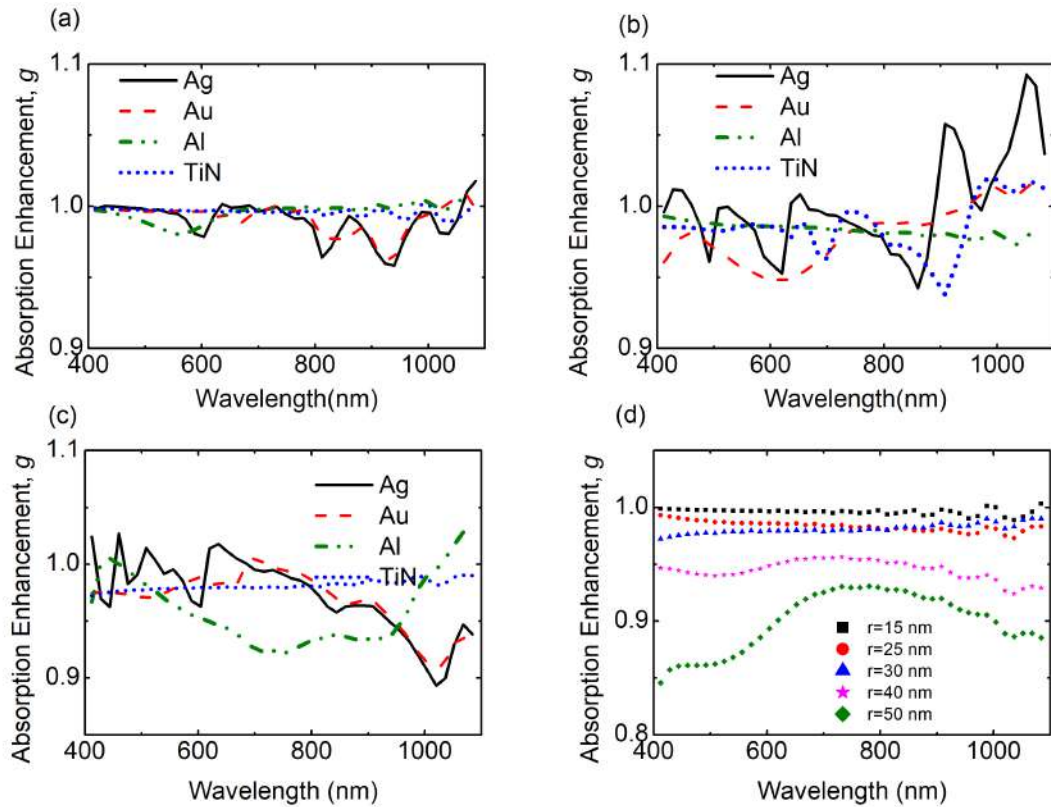


Figure 4.10: Absorption enhancement, g for the dimer of plasmonic spherical NPs for $r =$ (a) 15 nm, (b) 25 nm, and (c) 30 nm. (d) The g for TiN NPs with different radii.

g of TiN was ~ 1 for the whole spectral range which was better than Au and Al. For $r = 25$ nm, the g of TiN was between 0.9 to 1. For $r = 30$ nm the g of TiN was better than Al and comparable to Ag, Au for 400 to 800 nm and the g was greater than Ag, Au and Al for the range 800 nm to 1100 nm. For TiN, Al, Au, and Ag, the average enhancement, G , was discovered to equal 0.997, 0.991, 0.995, and 0.995, respectively.

We calculated LAE for TiN plasmonic nanosphere on a kesterite substrate from (4.2) to (4.3). The values of LAE for $r = 15$ nm were found to be 35.46% and 33.78% for TiN and Ag respectively.

We calculated g for different radii of TiN plasmonic dimer on a silicon substrate as can be seen from Figure 4.10(d). The g decreased with the increase of r for wavelength which agrees well with the previous study [103]. This happened as a result of plasmonic NP's strong forward scattering and weak absorption of light at various radii. While backward scattering prevented absorption, forward scattering promoted it. Spherical dimer plasmonic NPs with larger radii often have larger cross-sectional areas of scattering, this increase of metal NP and higher arrange mode excitation can control light scattering which improves or diminish the light absorbing productivity into the substrate [114].

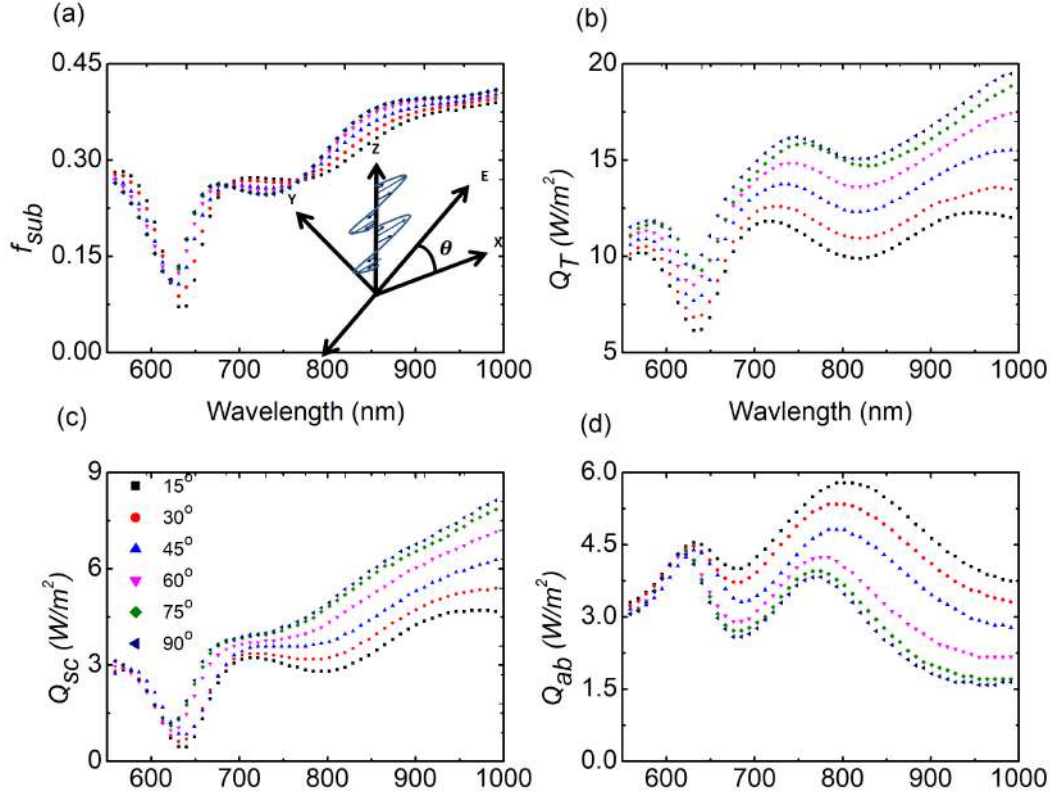


Figure 4.11: (a) f_{sub} , (b) Q_T , (c) Q_{sc} , and (d) Q_{ab} as a function of wavelength for TiN dimer shaped NP with varying the polarization angle of the source from $\theta=15^\circ$ to 90° .

4.3.3 Impact of Light Polarization

As the polarization of light influences light scattering or absorption, we varied the polarization angle of the light source to compute the optical characteristics of the NPs [103]. For the structure design with optimized scattering and absorption, we changed the source's polarization angle for dimer spherical TiN NPs and found the optimal polarization angle, θ . Here, t_1 and r were regarded as being 30 nm and 100 nm, respectively. The θ had been varied from 0° to 90° . For the wavelength ranging from 550 to 760 nm, the value of f_{sub} decreased with the increase of θ which is apparent from Figure 4.11(a). With a reduction in θ , f_{sub} remarkably dropped for the wavelength range of 760 nm to 1100 nm. As the θ was raised, it was evident from Figure 4.11(b) that Q_T increased significantly. The peak wavelength of Q_T had a red-shifted spectrum. As can be seen from Figure 4.11(c), Q_{sc} increased as the θ was increased and from Figure 4.11(d), Q_{ab} increased as the angle decreased from 90° to 15° .

Figures 4.12(a)–(f) represented E-field intensity for dimer NP with the variation of θ . The polarization angle defines the direction of the electric field and magnetic field. When the light was polarized in the x-direction (i.e., $\theta=0^\circ$), field enhancement was observed along the x-axis. As the angle changed, the induced dipole changed with θ and consequently, in-phase

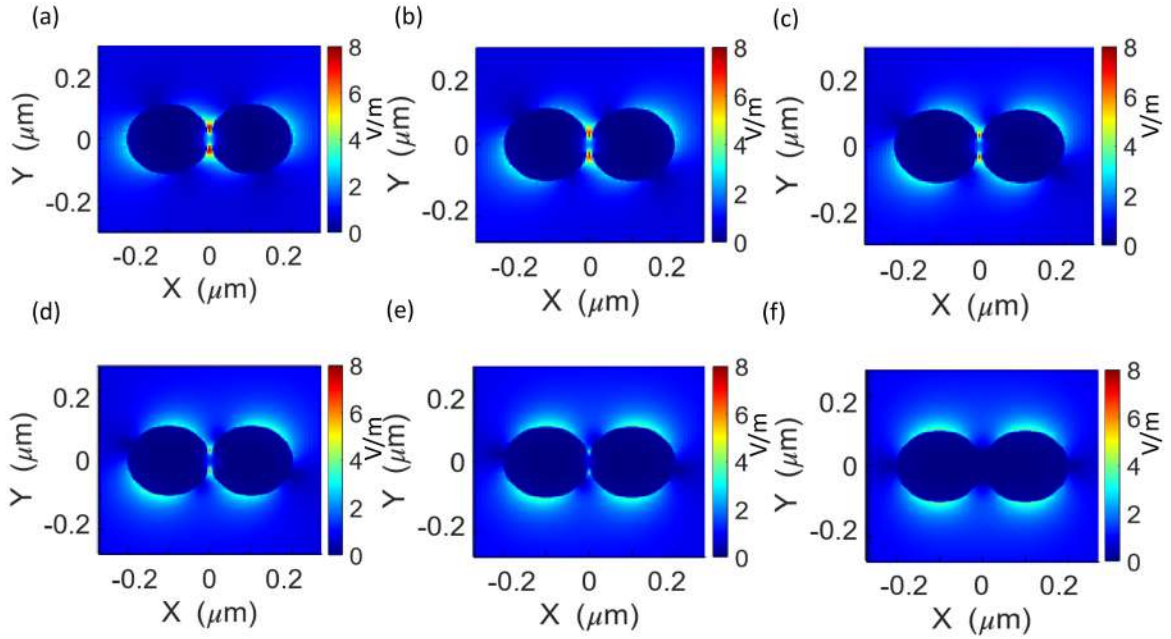


Figure 4.12: Color map showing the distribution of E-field in xy plane at $Z=0$ for TiN dimer NP placed on top of a 30 nm thin Si_3N_4 on a Si Substrate with varying the polarization angle of the source from $\theta = 15^\circ$ to 90° .

bonding and antibonding plasmon modes occurred accordingly [110,115]. When $\theta=15^\circ$ and the charge of the dimers oscillates in the same direction the charge accumulated, and electric field enhancement was observed at $\theta=15^\circ$. This phenomenon occurred both in bonding mode and anti-bonding mode when they are in-phase plasmon mode. The direction of charge oscillation changed along the θ producing an induced dipole moment [103]. Figure 4.12(a)-(c) illustrated the strong electric field enhancement that was observed in the x-direction when charge oscillation was increasingly aligned to the x-direction. As the polarized angle rose from 45° to 90° strong electric field enhancement was observed in the y-direction as charge oscillation alignment changed to y direction and the in-phase antibonding mode was observed as illustrated in Figures 4.12(d)-(f).

E-field intensity on the yz plane represented the center of the dimers, can be seen from Figures 4.13(a)-(f) with the variation of θ . When θ increased from 15° to 45° , the effective induced dipole moment decreased, which originated the in-phase antibonding mode, due to the E-field polarization alignment changed toward y direction presented in Figures 4.13(a)-(c). When θ increased from 60° to 90° , the charge was distributed along the y-direction, which was the polarization angle of the E-field. Consequently, the out-of-phase antibonding mode was apparent when θ was near 90° , as can be seen in Figures 4.13(d)-(f).

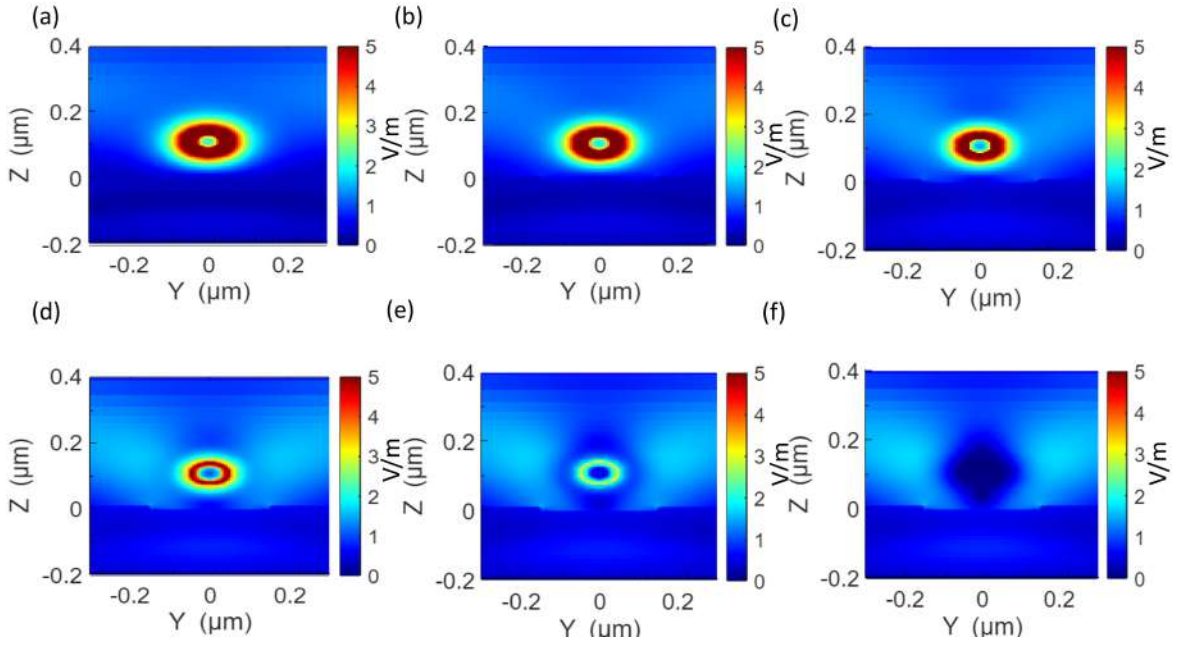


Figure 4.13: Color map showing the distribution of $|E|$ in the yz plane at $x=0$ for TiN dimer NP placed on top of a 30 nm thin Si_3N_4 on a Si Substrate with varying the polarization angle of the source from $\theta = 15^\circ$ to 90° .

4.3.4 Impact of the Distance Between the Spheres of Dimer

We studied the effect of variation of the distance between the spheres of TiN dimer spherical NP for 0° and 30° the light source polarization angle. We simulated dimer spherical NPs with various distances between the spheres as can be seen from Figure 4.14. We varied the distance, d from 0 nm to 50 nm to determine the structure for the optimized scattering cross-section. Here, t_1 and t_2 were considered 30 nm and 250 nm, respectively. The f_{sub} decreased with the increase of the d from $d = 0$ nm to 20 nm for 550 nm to 850 nm. When $d = 50$ nm the distance between the dimers increased, and they started to behave like a single sphere, As a result, f_{sub} increased Figure 4.14(a). When $d = 0$ nm, the Q_T spectrum was the lowest and increased as d increased. The Q_{sc} decreased as d increased from 0 to 20 nm for the 550 nm to 820 nm range. For longer wavelengths than 820 nm, Q_{sc} increased with the increase of d . Q_{ab} was highest when $d = 10$ nm. For the wavelength 550 to 750 nm, the Q_{ab} decreased with the increase of d . For the dimers with $d = 50$ nm, as the distance increased, it started to behave like two independent monomer nanospheres.

We simulated a spherical dimer NP for 30° the polarization angle of the source varying the distance between the spheres as can be seen in Figure 4.15. Here, t_1 and t_2 were considered 30 nm and 250 nm, respectively. The f_{sub} and Q_{sc} were comparatively higher for the whole spectral range for $d = 0$ nm and lowest for $d=20$ nm. When d was smaller than 50 nm the f_{sub} and Q_{sc} increased with the decrease of d , and Q_T increased with the increase of d . The Q_T was highest for $d = 10$ nm and performed better for the wavelength range 740 to 880

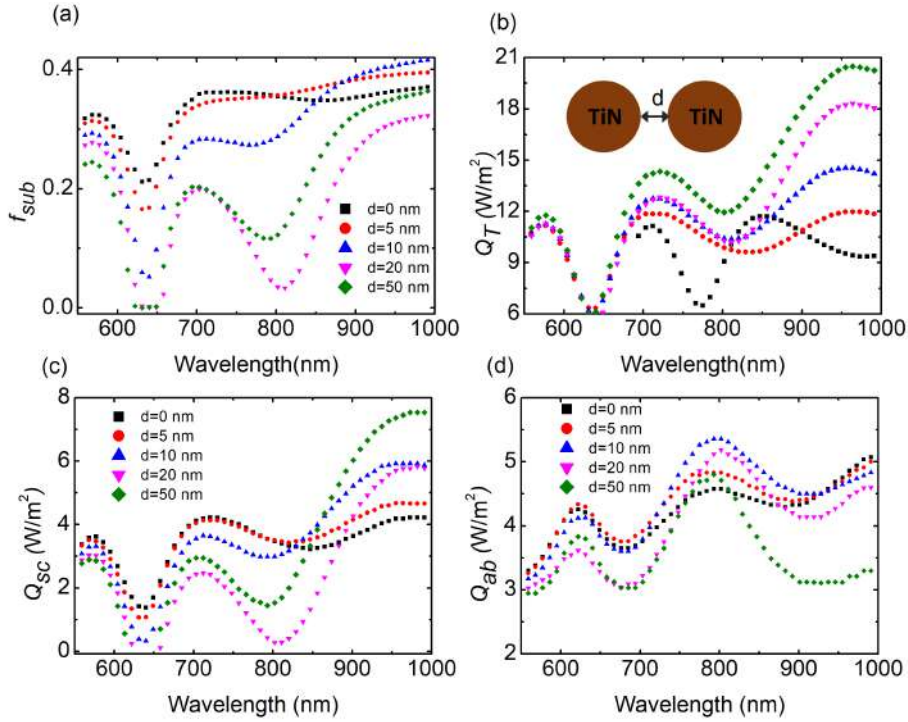


Figure 4.14: (a) f_{sub} , (b) Q_T , (c) Q_{sc} , and (d) Q_{ab} as a function of wavelength for TiN dimer spherical NP with distance, $d = 0, 20, 70,$ and 100 nm placed on top of a 30 nm Si_3N_4 on a Si substrate.

nm. Dimers performed better when there was no distance between the spheres. For the polarization angle from 0° to 30° , the scattering spectra red-shifted.

4.3.5 Dependency on the Radius of the Dimer Spherical NP

We simulated spherical dimer NPs with various radii and observed their optical characteristics, as seen from Figure 4.16. Here, t_1 and t_2 were considered 30 nm and 430 nm, respectively. We varied the r from 50 nm to 120 nm to determine an optimized structure for scattering cross-section. When the radius was 50 nm, Q_T was highest and the peak was almost 50 W/m^2 . Q_T and Q_{sc} decreased and Q_{ab} increased with the increase of radii. The foremost imperative factor for representing the path length enhancement of a light-trapping structure is f_{sub} [112]. As the radius increased, the value of f_{sub} decreased significantly [103]. At 50 nm and 70 nm thicknesses, f_{sub} did not change significantly. This made it possible to efficiently couple the part of the scattered light with a high in-plane wave vector that is transient in the air but engendered in silicon. As can be seen in Figures 4.16(b)-(c), Q_T and the Q_{sc} decreased as the r increased from 50 nm to 120 nm. For wavelength shorter than 700 nm, Q_{ab} decreased as the thickness increased, as can be seen from Figure 4.16(d). For wavelength longer than 700 nm, $r = 100$ nm exhibited the highest value of 5.5 W/m^2 . Consequently, the ideal thickness ought to be considered for good tunability of light.

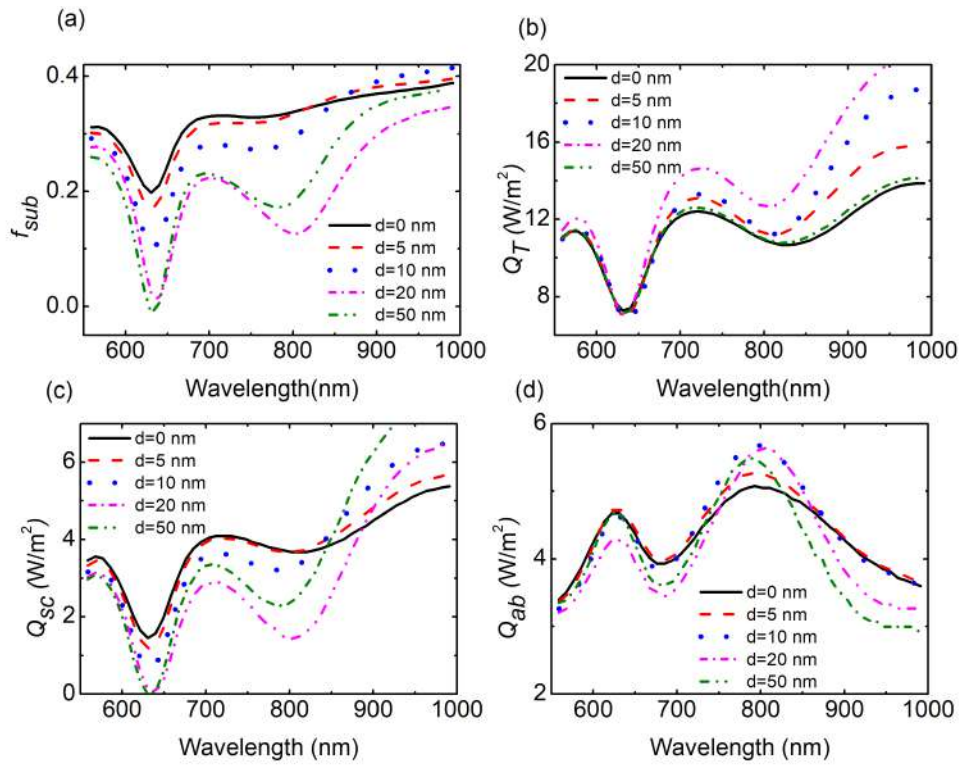


Figure 4.15: (a) f_{sub} , (b) Q_T , (c) Q_{sc} , and (d) Q_{ab} as a function of wavelength for TiN dimer spherical NP for 30° source polarization angle of the source with distance, $d = 0, 20, 70,$ and 100 nm placed on top of a 30 nm Si_3N_4 on a Si substrate.

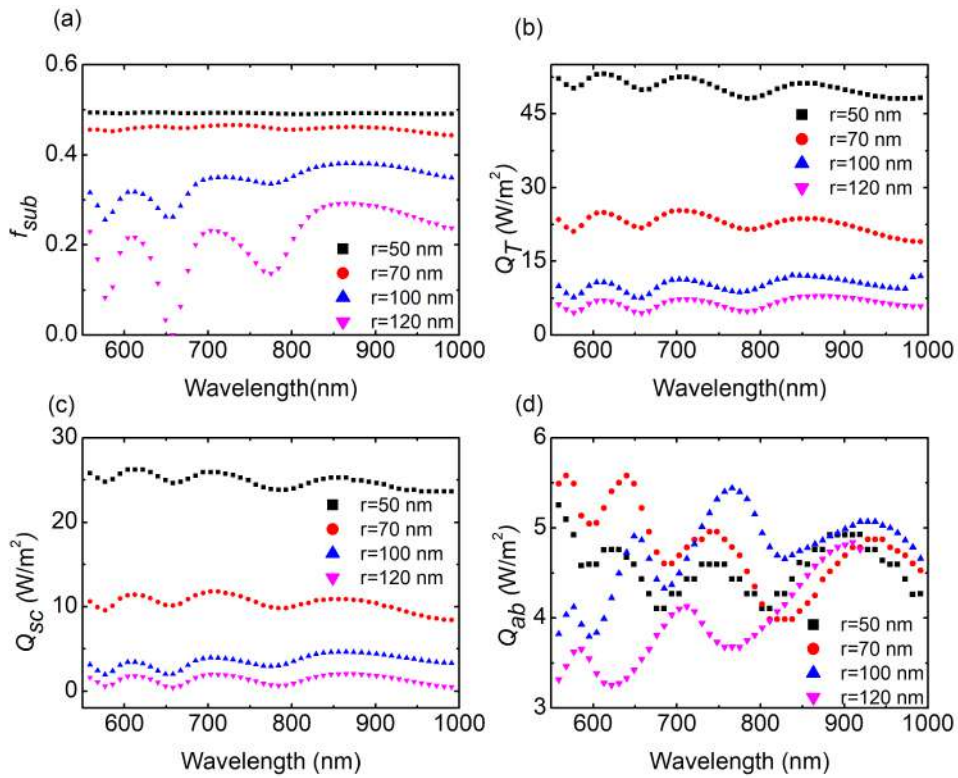


Figure 4.16: (a) f_{sub} , (b) Q_T , (c) Q_{sc} , and (d) Q_{ab} as a function of wavelength for dimer spherical TiN NPs with radius, $r = 50, 70, 100,$ and 120 nm placed on top of a 30 nm Si_3N_4 on a Si substrate.

Chapter 5

Efficient Light Trapping by TiN Plasmonic Bowtie Nanoparticles

5.1 Introduction

The plasmonic light trapping mechanism is an excellent way of improving light absorption in solar cells according to the analyses of the previous chapters. By controlling the size and shape of the metallic nanostructures, and the polarization angle of the source, the surface plasmon resonance or plasmon propagation can be tuned. In this chapter, We designed and assessed plasmonic nanosystems using bow tie-shaped TiN as an alternative material for photovoltaic application through theoretical simulations. To establish TiN's functionality as a plasmonic material we systematically studied the scattering cross-section of TiN NP using the finite-difference time-domain (FDTD) method. At first, we designed and optimized a bowtie-shaped plasmonic nanosystem, which consisted of two triangular nanoplates. Moreover, we determined the total scattering cross-section, the fraction of light scattered into the substrate, light scatter into the substrate, the absorption cross-section, and spatial mapping of the electric field in the plasmonic nanosystems. Additionally, we studied the polarization-sensitive performance of the bowtie nanosystem varying the polarization angle of the source. we conducted a comparative analysis utilizing TiN-based plasmonic nanostructures to show that the fraction of light scatter into the substrate can be tuned by varying the shape, size, thickness, dielectric thickness, and varying source angle. We examined the impact of the dielectric coating of the nanoparticles. Among the nanostructures, the bowtie shape showed a better light absorption cross-section. TiN nanostructures enhanced path length with a maximum scattering cross-section of 4.58 Wm^{-2} for bowtie-shaped nanoplate on 30 nm Si_3N_4 . Our study will be beneficial for utilizing TiN in a variety of plasmonic device applications.

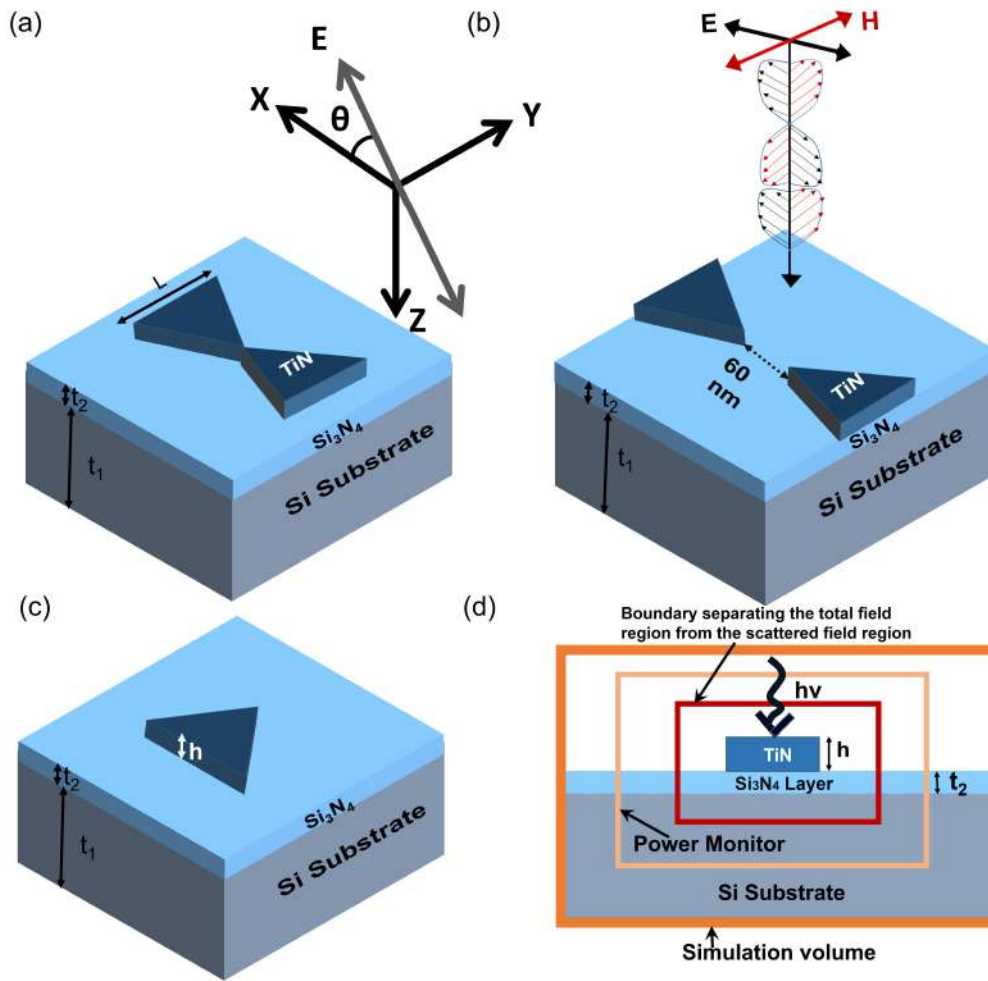


Figure 5.1: Visual representations of (a) a bowtie-shaped TiN nanoparticle, (b) a bowtie-shaped TiN nanoparticle with a distance of 60 nm between the two triangular plates, and (c) a triangle-shaped TiN nanoparticle. These nanoparticles were placed on top of a thin Si₃N₄ layer on a Si substrate. (d) A cross-section of the simulation set up. Light from the source was incident on the particle in the z-direction.

5.2 Structure and Simulation Method

5.2.1 Structural Design

Our designed nanostructure was composed of bowtie-shaped alternative plasmonic material, TiN-based nanoparticles on a semi-infinite crystalline silicon substrate as can be seen in Figure 5.1. TiN exhibits localized surface plasmon phenomenon and it is economically viable. Silicon, which is the most widely used semiconductor, was considered an absorber layer. The silicon was covered with a thin Si₃N₄ layer. The plasmonic particles were separated from the semi-infinite silicon absorber layer by this thin nitride layer. Such layers were present in solar cells for surface passivation. The shapes of nanoparticles considered

were triangular and bowtie-shaped nanoplates. In both cases, nanoplates were equilateral. In Figure 5.1, the thickness of the thin film and substrate were represented by t_1 and t_2 , respectively, and the polarization angle of the source was represented by θ . L denoted the side length, and h represented the thickness of the nanoparticle.

5.2.2 Simulation Method

We studied the mentioned nanosystems using the FDTD method where Maxwell's equations were solved numerically and simultaneously in both 3D space and time. A non-uniform mesh type was utilized for surrounding conditions. In the case of the nanoparticle, the mesh size was 4 nm. The TFSF source was polarized perpendicular to the surface normal on the particle from the air side as the nanoparticles ranged from 550 to 1100 nm, covering the effective irradiance of the solar spectrum (AM 1.5). The mapping of the near electric field intensity was calculated by a monitor at the desired spatial point. The electric and magnetic fields around the particle were calculated from (3.1). The absorption cross-section, Q_{ab} is the total absorbed power divided by the power per unit area of the incident beam. The monitors located inside the TFSF source measured the net power flowing into the particle and the Q_{ab} was calculated by normalizing it to the source intensity. Similarly, Q_T was calculated from the power measured in the monitors outside the TFSF source. Here, Q_{sc} is the cross-section of light scatter into the substrate. The fraction of light scattered into the substrate, f_{sub} is defined as the ratio of power in the scattered field region inside the Si substrate to the power in the scattered field region in air and in Si. As single particle simulations provide a good means of predicting the experimental behavior of random particle arrays [52, 111], we considered a single nanoparticle during our simulations. We systematically studied the effect of nanoparticles on Q_T , Q_{sc} , f_{sub} , and Q_{ab} by sweeping their structural properties. And, we comprehensively studied the ability to enhance the absorption inside the substrate due to the addition of nanoparticles. Moreover, the impact of the polarization angle of incident light was explored by varying incident light polarization from 0° to 90° .

5.3 Results and Discussion

To comprehend the impact of nanoparticles and the polarization angle of the source, we explored nanostructures by varying shapes of nanoparticle structure and polarization of light in subsequent subsections. Moreover, a detailed study of the structural variation of nanoparticles embedded in thin films was studied to study their prospects in solar cells.

5.3.1 Effect of the Variation of Bowtie Nanoparticle Thickness

We simulated bowtie-shaped nanoplates with various thicknesses and observed their scattering and absorbance behavior. We varied the thickness, h from 50 nm to 250 nm to determine an optimized structure for scattering cross-section. Here, t_1 , t_2 , and L were considered to be 10 nm, 250 nm, and 200 nm, respectively. When the thickness was 50 nm and 75 nm, Q_T was highest for the wavelength 550 nm to 900 nm as can be seen in Figure 5.2(b). As can be seen in Figures 5.2(c)-(d), Q_{sc} decreased and Q_{ab} increased with the increase of thickness. As the thicknesses of 50 nm and 75 nm were comparatively negligible, hardly any light was absorbed and all the light was scattered. Hence, as a tradeoff, we considered an optimum thickness between 100 nm to 200 nm thickness for a great performance.

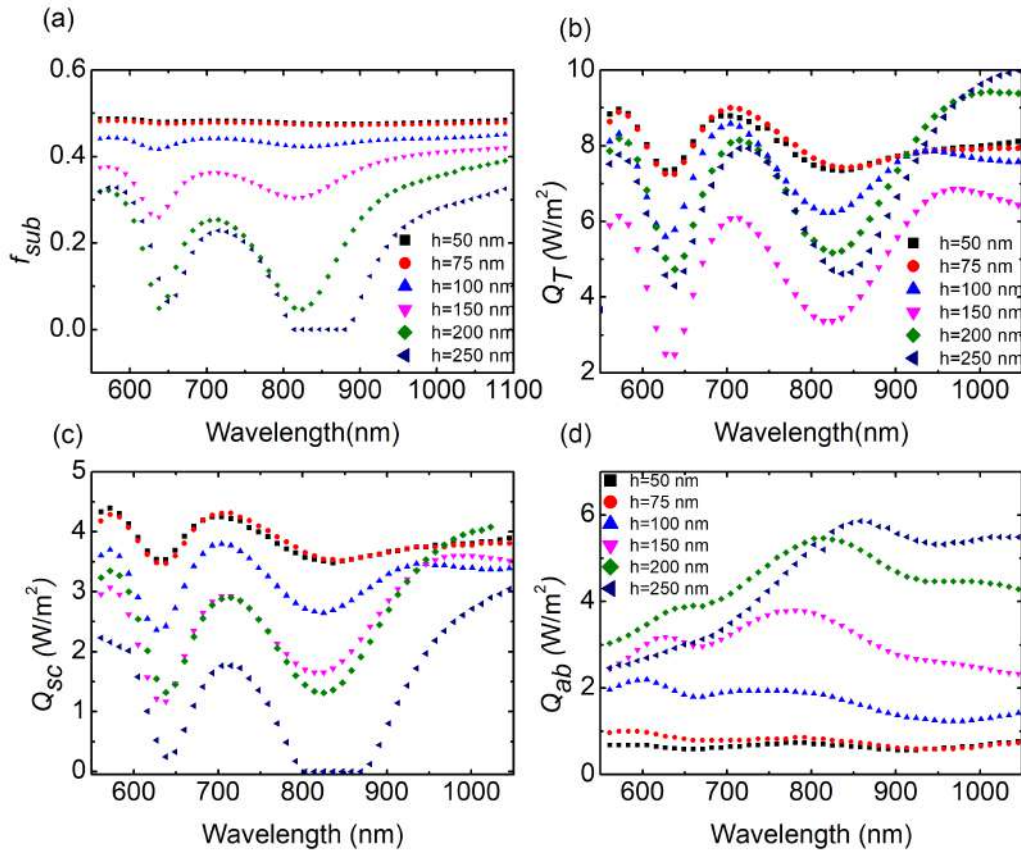


Figure 5.2: (a) f_{sub} , (b) Q_T , (c) Q_{sc} , and (d) Q_{ab} as a function of wavelength for Tin bowtie shaped nanoplate with thickness, $h = 50, 100, 150, 200,$ and 250 nm placed on top of a 10 nm Si_3N_4 on a Si substrate.

Again, the most important factor for the representation of the path length enhancement of a scattering light-trapping structure is f_{sub} [112]. As can be seen in Figure 5.2(a), the value of f_{sub} decreased significantly as the thickness was increased. For thicknesses 50 nm and 75 nm, f_{sub} did not vary significantly. This allowed efficient coupling of the portion of the scattered light that was high in-plane wave vector and was evanescent in the air but propa-

gated in silicon. As can be seen in Figure 5.2(b), Q_T decreased as the thickness increased from 50 nm to 150 nm. For h greater than 150 nm, it started to increase and the Q_T became highest for 250 nm thickness for 1100 nm wavelength. The Q_{sc} increased as the thickness decreased and Q_{ab} increased as the thickness increased as can be seen from figures 5.2(c) and (d). As the thickness of 50 nm was quite small, most of the light was scattered and the TiN nanoplates did not absorb light which is evident from Figures 5.2(b), (c), and (d). Hence, the optimum thickness should be considered for proper tunability of light.

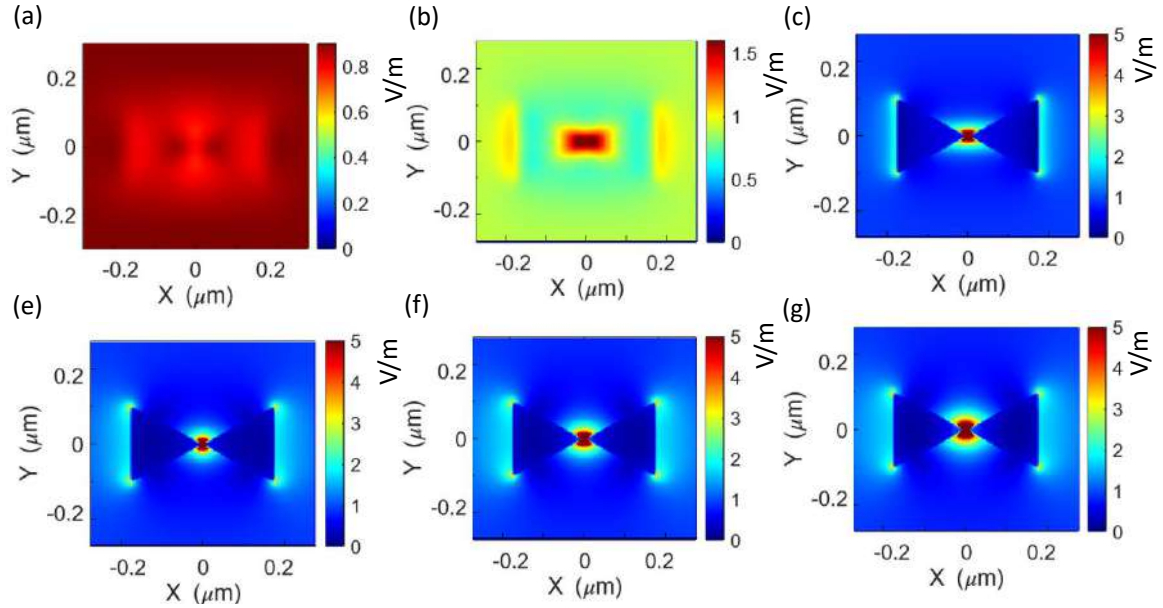


Figure 5.3: Color map showing the xy spatial distribution of $|E|$ for TiN bowtie-shaped nanoplate placed on top of a 10 nm thin Si_3N_4 on a Si substrate with varying thickness, $h =$ (a) 50, (b) 75, (c) 100, (d) 150, (e) 200, and (f) 250 nm.

As can be seen in Table 5.1, Q_T had the highest peak value of 10.89 Wm^{-2} at $h = 250 \text{ nm}$, it had the lowest value of 6.85 Wm^{-2} at $h = 150 \text{ nm}$, and the wavelength was redshifted. Q_{sc} decreased with the increase of h and redshifted. Q_{ab} increased with the increase of h and had a large absorption cross-section at $h = 250 \text{ nm}$. The peak wavelengths for Q_{ab} redshifted as h increased from 75 nm to 250 nm.

Table 5.1: Dependency of the cross-sections on bowtie thickness

Bowtie thickness	Q_T		Q_{sc}		Q_{ab}	
	Peak Value (Wm^{-2})	Wavelength (nm)	Peak Value (Wm^{-2})	Wavelength (nm)	Peak Value (Wm^{-2})	Wavelength (nm)
50 nm	8.96	572	4.3	561	.77	1078
75 nm	9	704	4.3	715	0.97	561
100 nm	8.58	704	3.77	715	2.2	605
150 nm	6.85	968	3.6	1000	3.8	780
200 nm	9.43	1012	4	1000	5.46	814
250 nm	10.89	1012	3.33	1090	5.86	858

When a plane wave impinges on an object or a scatterer, the energy carried by the plane wave

is deflected to other directions. The analysis of optical features such as the scattering cross-section, the electric field distribution as well as the E-plane and H-plane radiation patterns, provided a systematic near and far field characterization of the nanoparticles. The electric field map was observed in the xy zx and yz planes for the incident wavelength 1100 nm by varying the thickness of the TiN bowtie nanoplates which is presented in Figures 5.3-5.5. These structures can create LSPR where free charges accumulate precisely at the edges of the nano-gap.

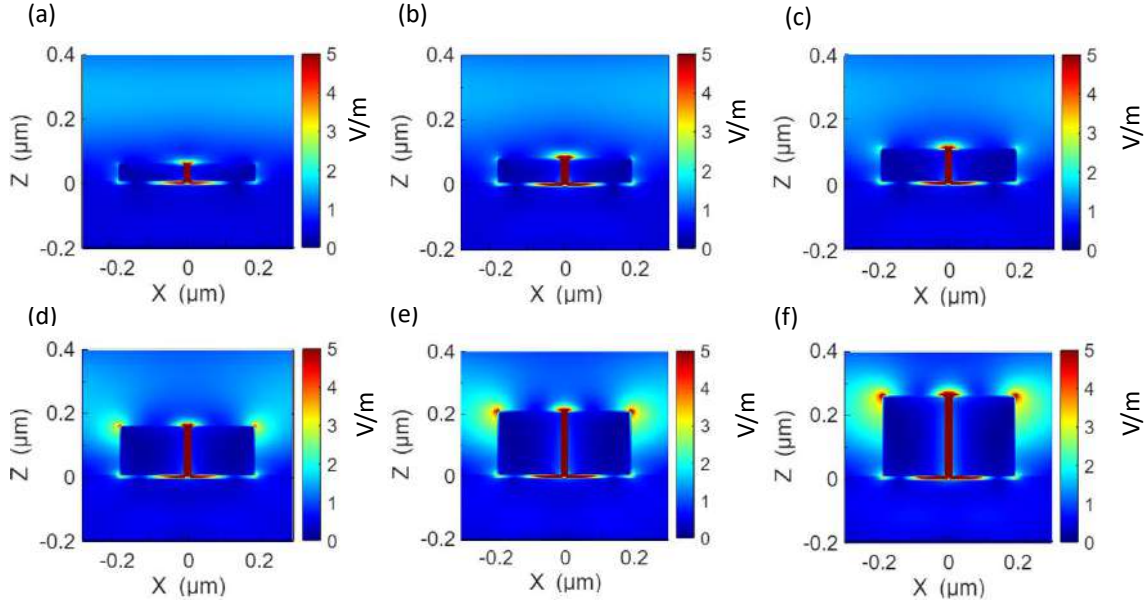


Figure 5.4: Color map showing the zx spatial distribution of $|E|$ for TiN bowtie-shaped nanoplate placed on top of a 10 nm thin Si_3N_4 on a Si substrate with varying thickness, $h =$ (a) 50, (b) 75, (c) 100, (d) 150, (e) 200, and (f) 250 nm.

When $h = 50$ nm and 75 nm, free charge accumulation resulted in minimal E-field enhancement and the charge density scatter along the surface as can be seen in Figures 5.3(a) and (b). Charge density accommodated strong surface plasmon coupling resulting in high charge distribution along the edges and the center of the bowtie nanoplate as can be seen in Figure 5.3(d). Charge localization near the edges and the center of the metal surface fell rapidly for increasing the thickness of TiN metal film as presented in Figures 5.3(e) and (f) which agreed well with the previous report [57]. For 50 nm thickness, the light was almost scattered and there was no absorption. Hence, the thickness increased charge accumulation and the far-field pattern increased.

Moreover, we investigated E-field intensity on the zx -plane as can be seen in Figure 5.4. When $h = 50$ nm, 75 nm and 100 nm, a small amount of free charge accumulated and resulted in minimal E-field enhancement at the top and bottom edges of the material surface which was consistent with the xy and yz planes. When h increased from 150 to 250 nm, charge density accommodated strong surface plasmon coupling resulting in high charge

distribution along the bottom and top corners, and the center of the bowtie nanoplate as can be seen in Figures 5.4(d)-(f).

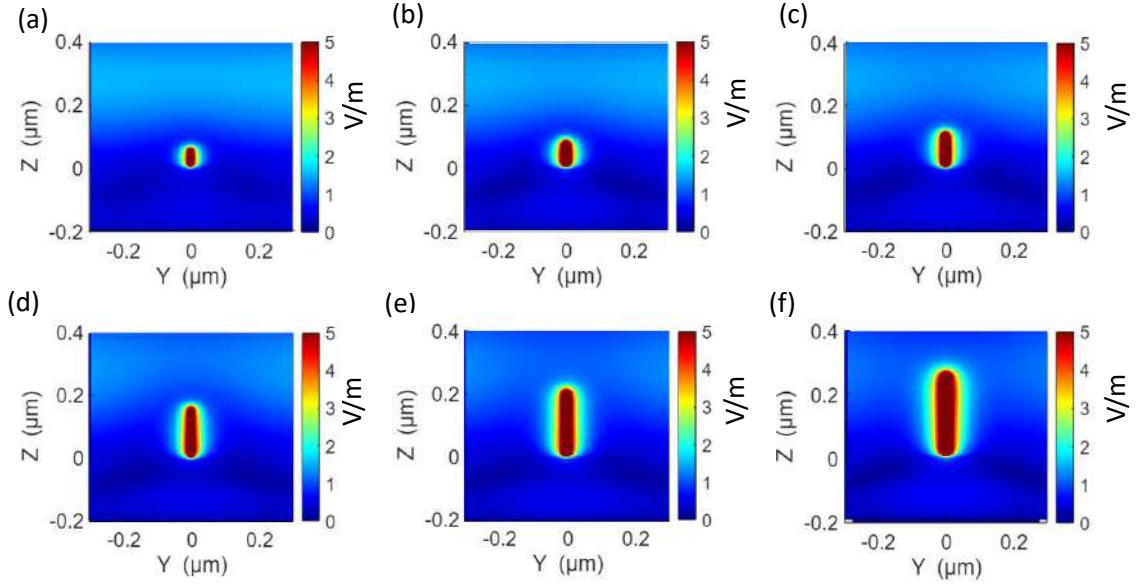


Figure 5.5: Color map showing the yz spatial distribution of $|E|$ for TiN bowtie-shaped nanoplate placed on top of a 10 nm thin Si_3N_4 on a Si substrate with varying thickness, h of (a) 50, (b) 75, (c) 100, (d) 150, (e) 200, and (f) 250 nm.

E-field intensity on the yz plane can be seen from Figure 5.5 for bowtie nanoplate with the variation of thickness. Charge density accommodated strong surface plasmon coupling with the increase of thickness resulting in high charge distribution along the surface of the bowtie nanoplate as can be seen in Figure 5.5.

5.3.2 Impact of Light Polarization

We varied the polarization angle of the light source and calculated the optical characteristics of the nanoparticles. For the structural design with the optimized scatterings and absorption, we considered a bowtie-shaped TiN nanoparticle and varied the polarization angle of the source, and detected the optimized polarization angle, θ . Here, t_1 , t_2 , L , and h were considered to be 10 nm, 250 nm, 200 nm, and 100 nm, respectively. The θ was varied from 0° to 90° . As the θ was increased, the Q_T , Q_{sc} and Q_{ab} increased and the peak wavelength of Q_T was blue-shifted.

For the wavelength ranging from 550 to 650 nm, the value of f_{sub} decreased significantly as the θ was increased as apparent from Figure 5.6(a). For the wavelength longer than 650 nm, f_{sub} decreased significantly as θ was decreased. It can be seen from Figure 5.6(b) that Q_T increased significantly as the θ was increased. As can be seen from Figure 5.6(c) and (d) the Q_{sc} increased significantly as the θ was increased. As can be seen from Figure 5.6(d),

Q_{ab} increased as the angle increased for wavelength ranged from 550 to 780 nm. For wavelengths longer than 780 nm, Q_{ab} decreased as the θ was increased. When the contributions from horizontal and vertical polarization are equal, resulting in a vanishing net polarization. The quantitative calculation of the scattering light of the polarized fraction has been carried out assuming that the scattering of each small volume of the nanoplate is isotropic in the bowtie nanoplate and scattering at the edges and corners was higher. By changing θ , the degree of polarization which is the quantity of the portion of an electromagnetic wave that is polarized can be controlled.

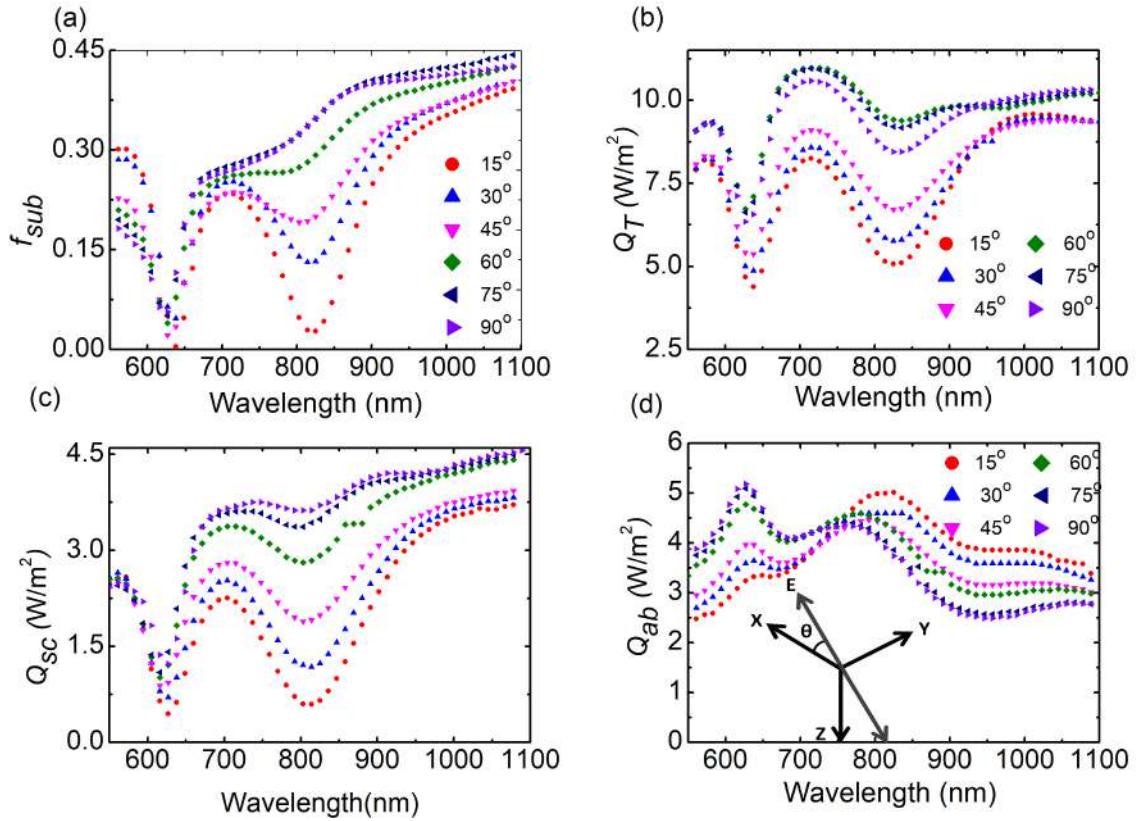


Figure 5.6: (a) f_{sub} , (b) Q_T , (c) Q_{sc} and (d) Q_{ab} for various polarization angle of the source from $\theta=15^\circ$ to 90° .

Power absorption spectra can be seen in Figure 5.7 for various θ from 0° to 90° . The absorption power spectra increased with the increase of θ till around 700 nm wavelength and for the longer wavelengths, decreased as θ increased as can be seen in Figure 5.7.

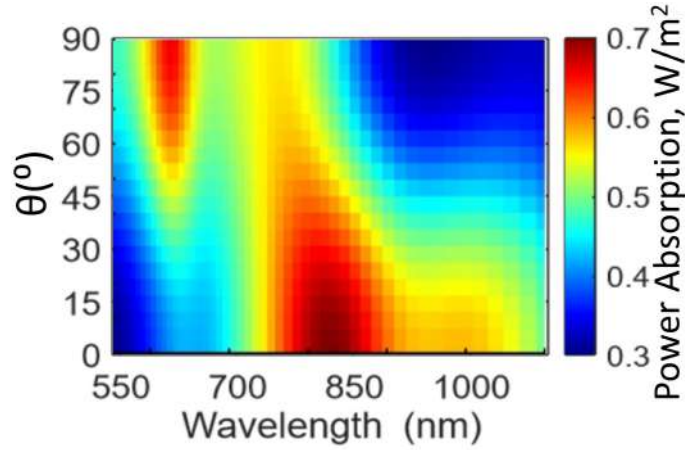


Figure 5.7: Absorbed power spectra for various polarization angle of the source from $\theta=15^\circ$ to 90° .

As can be seen in Table 5.2, the peak value of Q_T , and Q_{ab} increased as the θ increased. The peak wavelength for Q_{sc} was independent of the polarization angle. Peak wavelength for Q_T and Q_{ab} were blueshifted.

Table 5.2: Effect of polarization of incident light on cross-sections

Polarization angle	Q_T		Q_{sc}		Q_{ab}	
	Peak Value (Wm^{-2})	Wavelength (nm)	Peak Value (Wm^{-2})	Wavelength (nm)	Peak Value (Wm^{-2})	Wavelength (nm)
15°	9.55	1034	3.5	1085	5	825
30°	9.47	1034	3.75	1085	4.6	825
45°	9.39	1056	3.97	1085	4.46	792
60°	10.97	715	4.20	1090	4.76	627
75°	10.95	715	4.32	1090	5	627
90°	10.58	715	4.31	1090	5.18	627

Figures 5.8(a)–(f) show E-field intensity on the xy -plane for bowtie nanoplates with the variation of θ . When θ was smaller, charge accumulation and E-field were enhanced at the centers as can be seen in Figures 5.8(a)–(c). As θ increased, the charge accumulation increased for strong surface plasmon coupling resulting in high charge distribution at the corner of the edges of the bowtie nanoplate as can be seen in Figures 5.8(d)–(f).

The spatial distribution of E-field intensity on the zx plane (at $y=0$) can be seen from Figures 5.9 (a)–(f) for bowtie nanoplates with the variation of θ . When $\theta = 15^\circ, 30^\circ$, and 45° , a large amount of free charge accumulated resulting in E-field enhancement at the top and bottom edges of the material surface. At the corners that were along or nearby the E-field direction, charge accumulation was higher than other corners as is apparent in Figures 5.9(a)–(c). When θ increased from 60° to 75° charge distribution of the corner mentioned earlier started to decrease and other corners started to increase as can be seen in Figures 5.9(a)–(c). For $\theta = 90^\circ$, charge density accommodated and surface plasmon coupling resulting in charge

distribution equally along the corners and the center of the bowtie nanoplate as shown in Figure 5.9(f).

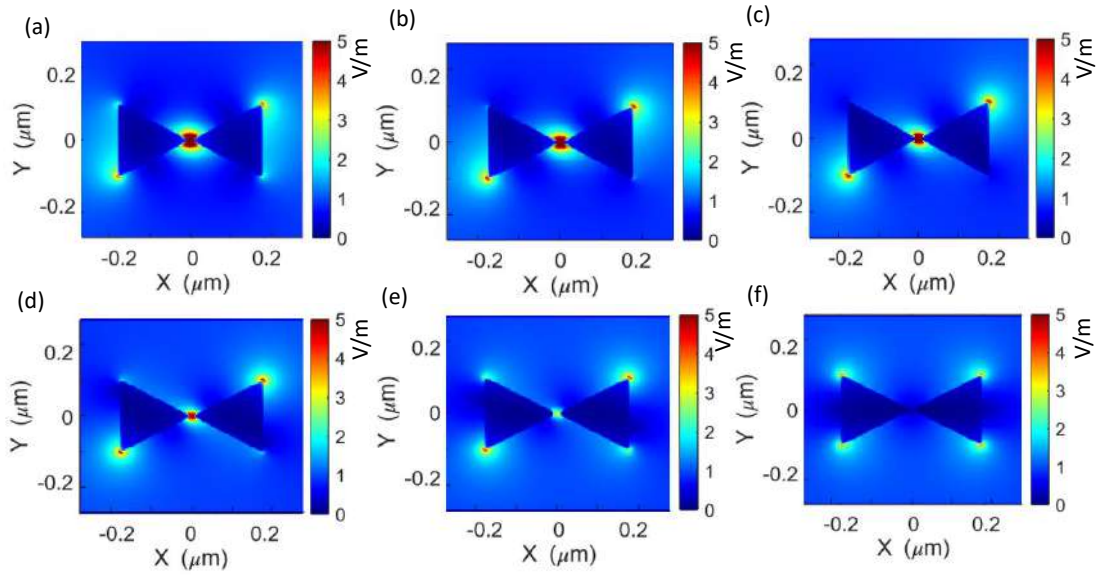


Figure 5.8: Color map showing the xy distribution of $|E|$ for TiN bowtie-shaped nanoplate placed on top of a 10 nm thin Si_3N_4 on a Si substrate with varying the polarization angle of the source from $\theta=15^\circ$ to 90° .

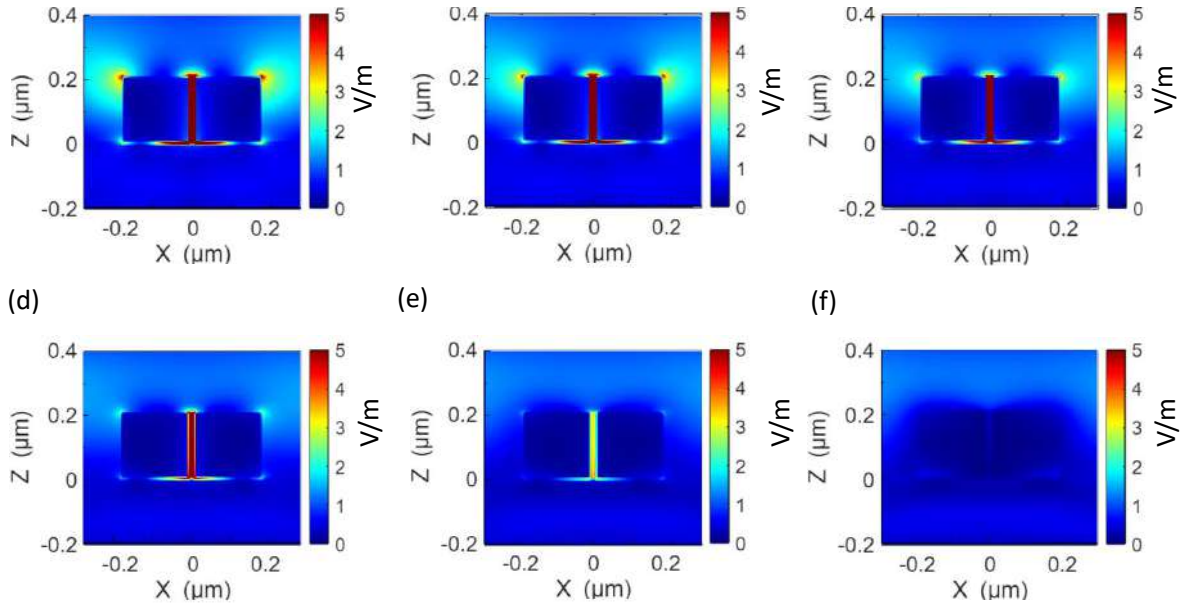


Figure 5.9: Color map showing the zx spatial distribution of $|E|$ for TiN bowtie-shaped nanoplate placed on top of a 10 nm thin Si_3N_4 on a Si substrate with varying the polarization angle of the source from $\theta=15^\circ$ to 90° .

The E-field intensity distribution in zx plane at $y=100$ nm for bowtie nanoplate with the variation of θ can be seen in Figure 5.10. When θ increased from 15° to 45° a large amount of free charge accumulated at the edges of bowtie and the charge accumulations were significantly higher at the corner. However, charge accumulation was higher in the corners,

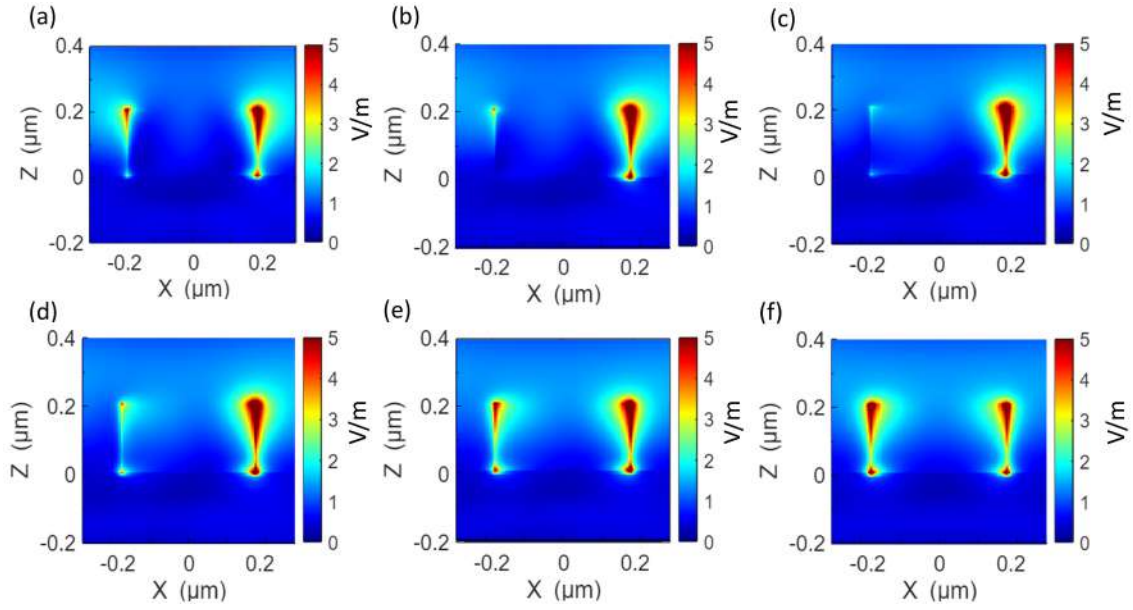


Figure 5.10: Color map showing the zx distribution of $|E|$ for a cross-section at $y=100$ nm for TiN bowtie-shaped nanoplate placed on top of a 10 nm thin Si_3N_4 on a Si substrate with varying θ from 15° to 90° .

which were along or nearby the E-field direction, than in other corners as presented in Figures 5.10(a)-(c). When θ increased from 60° to 90° charge distribution started to become equally distributed in all corners of the bowtie nanoplate as can be seen in Figures 5.10(d)-(f). The center of the bowtie had a large charge accumulation.

Color map showing the yz distribution of E-field for bowtie nanoplate with the variation of θ placed on top of a 10 nm thin Si_3N_4 on a Si substrate presented in Figure 5.11. When $\theta = 0^\circ, 15^\circ, 30^\circ$ and 45° , free charge accumulation resulted in high E-field enhancement and accommodated strong surface plasmon coupling resulting in high charge distribution at the center of bowtie as can be seen in Figures 5.11(a)-(d). Charge localization near the surface of the material decreased and distributed equally with the increase of θ as presented in Figures 5.11(e) and (f).

Color map showing the yz distribution of E-field for bowtie nanoplate with the variation of θ placed on top of a 10 nm thin Si_3N_4 on a Si substrate presented in Figure 5.11. When $\theta = 0^\circ, 15^\circ, 30^\circ$ and 45° , free charge accumulation resulted in high E-field enhancement and accommodated strong surface plasmon coupling resulting in high charge distribution at the center of bowtie as can be seen in Figures 5.11(a)-(d). Charge localization near the surface of the material decreased and distributed equally with the increase of θ as presented in Figures 5.11(e) and (f).

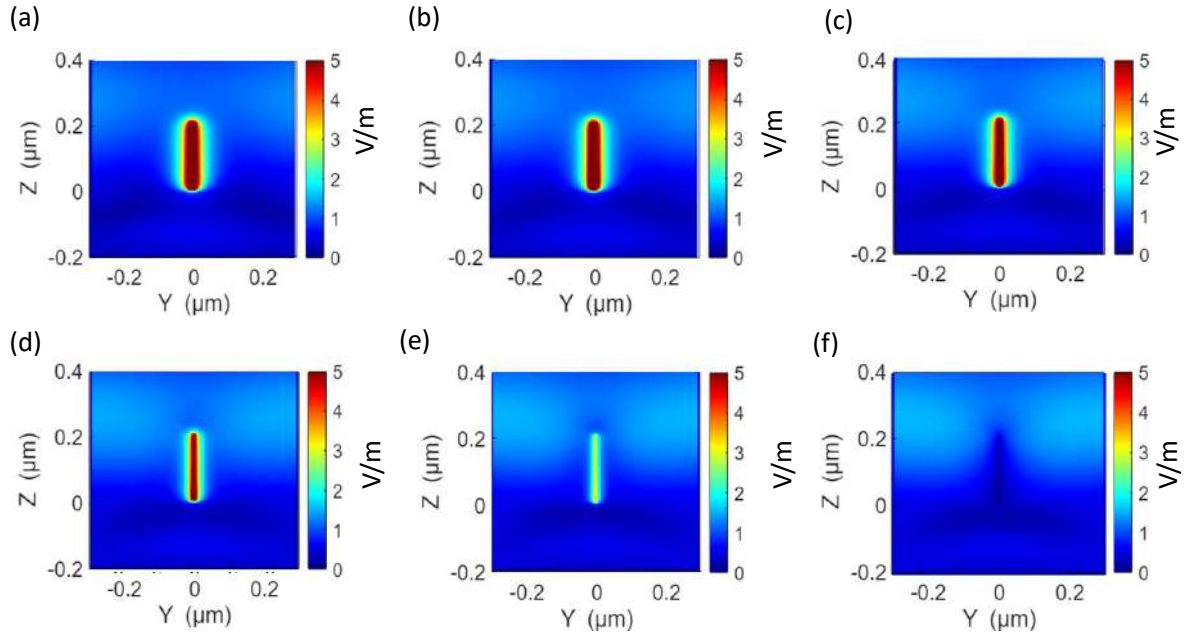


Figure 5.11: Color map showing the yz distribution of $|E|$ at $x=0$ nm for TiN bowtie-shaped nanoplate placed on top of a 10 nm thin Si_3N_4 on a Si substrate with varying θ from 15° to 90° .

5.3.3 Dependency on the Gap Distance Between the Triangles of the Bowtie

We varied the gap distance, d between triangles to discover the optimum distance and further use it for cross-section calculation. As can be seen in Figure 5.12(a) the f_{sub} increased with the increase of distance and it was highest for $d=60$ nm and 70 nm. Q_T and Q_{sc} mostly increased with the increase of d observed in Figure 5.12(b)-(c). The Q_{ab} had the highest value for $d=60$ nm and decreased as the d decreased, however, Q_{ab} had the lowest value for $d=70$ nm as can be seen in Figure 5.12(d). Therefore to achieve the best result we considered the distance of 60 nm and further used the shape with 60 nm distance.

5.3.4 Effect of Varying the Shape and Thickness of Dielectric Material

The shapes of TiN-based nanoparticles that we investigated were a bowtie shape, a bowtie shape consisting of two triangles with a 60 nm distance from each other, and a triangular shape. The thickness of dielectric material Si_3N_4 was varied to evaluate the optical performance. Here, t_2 , L , and h were considered to be 250 nm, 200 nm, and 100 nm, respectively. We varied the thickness of dielectric thin film Si_3N_4 from 5 nm to 40 nm and observed the spectra of f_{sub} , Q_T , Q_{sc} and Q_{ab} for nanoparticles as can be seen in Figure 5.13 and Figure 5.16. The f_{sub} remained unchanged for variation of the thin film. The Q_T and Q_{sc}

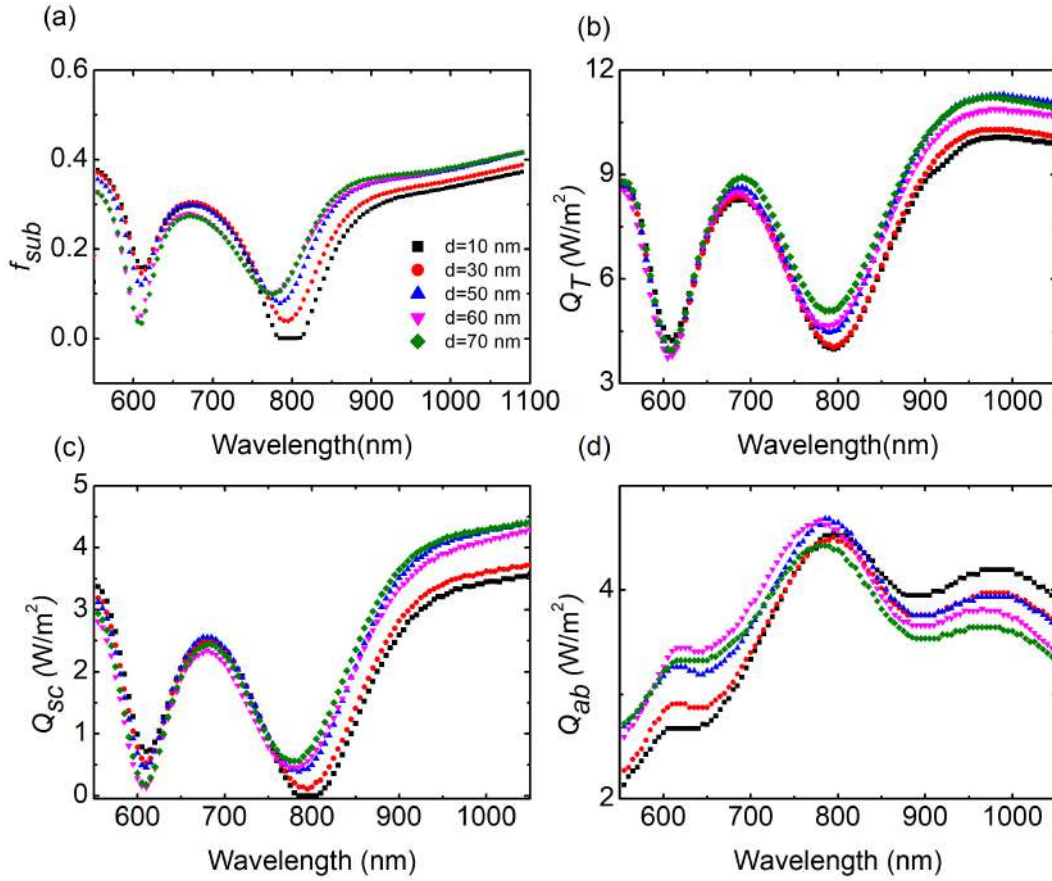


Figure 5.12: (a) f_{sub} , (b) Q_T , (c) Q_{sc} , and (d) Q_{ab} as a function of wavelength for Tin bowtie-shaped nanoplate with varying distance, d between the triangles. $d= 10, 30, 50, 60,$ and 70 nm placed on top of a 30 nm Si_3N_4 on a Si substrate.

increased as the thickness of the dielectric increased showing consistent results deduced from Figures 5.14(b)-(c). As can be seen from Figures 5.13(d), the nanoparticle had maximum absorption for 30 nm dielectric thickness. The optimum thickness of Si_3N_4 thin film is necessary as a large amount of hydrogen, originating from plasma gas dissociation, incorporated in the Si_3N_4 film is driven into silicon during the metallization step, leading to excellent bulk passivation for multi-crystalline silicon solar cells. The driving force was the surface passivation effect. Silicon nitride provides very low surface recombination velocities both on p-type and n-type cells. Moreover, the anti-reflective properties of the nitride layer reduce considerably the light reflection.

We calculated cross-sections for TiN particles on 30 nm and 10 nm thick Si_3N_4 on semi-infinite silicon with bowtie shaped NP as can be seen Figure 5.14 and Figure 5.15. Structures with 30 nm thick Si_3N_4 performed better. For 30 nm Si_3N_4 film, Q_T had the highest value of 11 Wm^{-2} when the shape was triangular nanoplate and Q_{ab} had the highest value of 4.76 Wm^{-2} for bow tie-shaped nanoplate. The maximum Q_{sc} of 4.58 Wm^{-2} and 5.23 Wm^{-2} were obtained for bowtie-shaped and triangular shaped nanoplate respectively. As can be seen in Figure 5.14, for the entire wavelength range, the f_{sub} was much higher for triangle

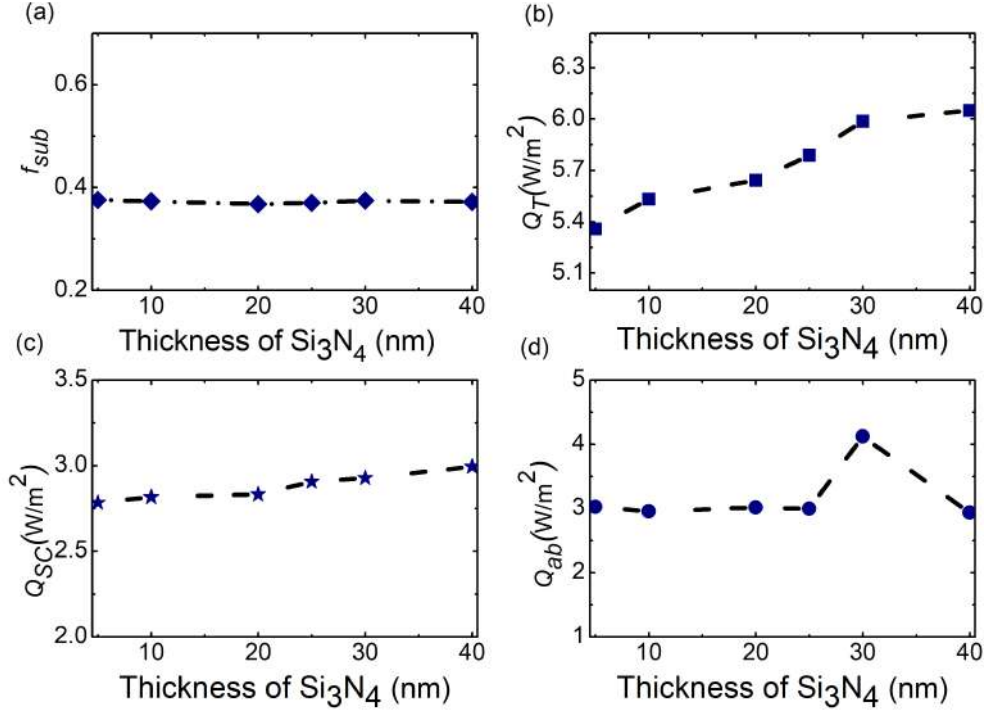


Figure 5.13: Average (a) f_{sub} , (b) Q_T , (c) Q_{sc} , and (d) Q_{ab} for TiN bowtie-shaped nanoplate for various thickness of dielectric material, Si₃N₄ on a Si substrate.

and bowtie than that for bow tie with a distance of 60 nm. It can be seen from Figure 5.14, Q_T and Q_{sc} had the highest value for triangular-shaped nanoplates, and Q_{ab} had the highest value for bow tie-shaped nanoplate. Bowtie-shaped TiN nanoparticles had a peak value of 0.42. Hence, light trapping using a triangular shape or a bowtie shape nanoparticle will be efficient.

We calculated f_{sub} , Q_T , Q_{sc} and Q_{ab} for TiN triangular and, bowtie shaped nanoplates on a 10 nm thin Si₃N₄ on the semi-infinite silicon substrate. As can be seen in Figure 5.15, the f_{sub} was much higher for triangle and bowtie than that for bow tie with a distance 60 nm for the entire wavelength range. For 10 nm Si₃N₄, it can be seen from Figures 5.15(b), (c), and (d) that Q_T and Q_{sc} had the highest value for triangular shape and Q_{ab} had the highest value for bow tie-shaped nanoplate with 60 nm distance.

In addition to the results presented in the article, we varied the thickness of dielectric thin film Si₃N₄ from 5 nm to 40 nm and observed the result of f_{sub} , Q_T , Q_{sc} and Q_{ab} for triangular shaped nanoplate as presented in Figure 5.16. The f_{sub} was independent of the variation of thickness of the dielectric and showed promising results. The Q_T and Q_{sc} increased as the thickness of the dielectric increased showing consistent results as shown in Figures 5.15(b)-(c). The triangular nanoplate had a higher scattering cross-section than the bowtie-shaped nanoplate. As can be seen from Figure 5.16(d), the Q_{ab} showed constant absorption for the 5 nm to 40 nm range. Triangular nanoplate had poor absorption characteristics than other shaped nanoplates which were consistent with results presented in Figure 5.15.

Table 5.3: Cross-section comparison for different shapes of the nanoparticles

Shape and dielectric thickness	Q_T		Q_{sc}		Q_{ab}	
	Peak Value (Wm^{-2})	Wavelength (nm)	Peak Value (Wm^{-2})	Wavelength (nm)	Peak Value (Wm^{-2})	Wavelength (nm)
Bow Tie (30 nm Si_3N_4)	9.35	990	4.58	1100	4.76	840
Bow Tie (10 nm Si_3N_4)	9.03	1025	3.53	1055	3.33	985
Bow Tie with 60 nm distance (30 nm Si_3N_4)	10.87	990	4.51	1100	4.67	780
Bow Tie with 60 nm distance (10 nm Si_3N_4)	10.01	1015	4.12	1095	4.16	795
Triangular (30 nm Si_3N_4)	11	1100	5.23	1000	2.3	725
Triangular (10 nm Si_3N_4)	10.4	1100	4.93	1090	2.3	650

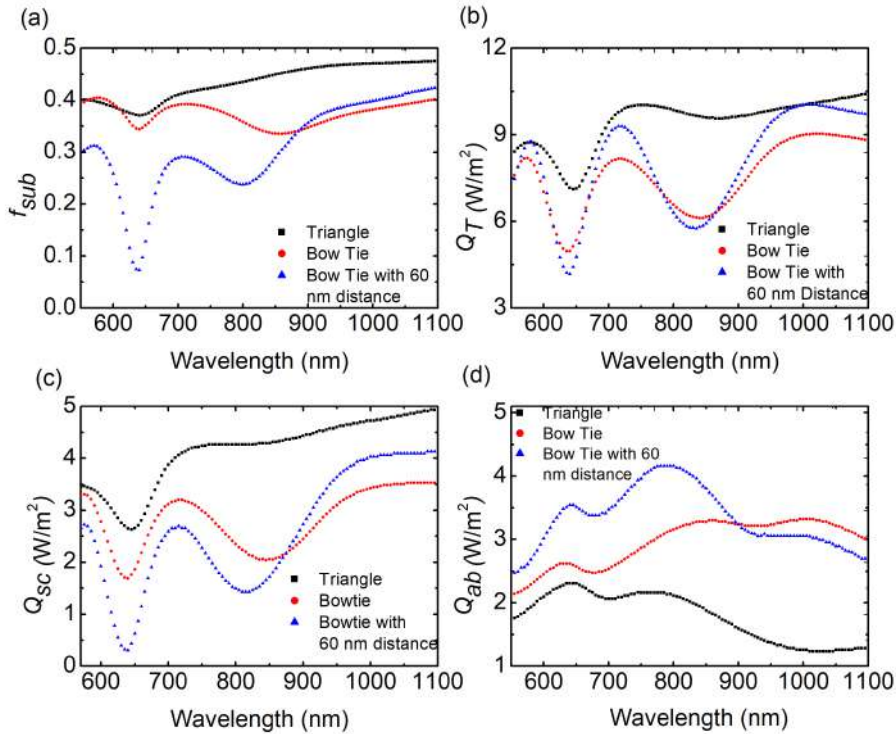


Figure 5.15: (a) f_{sub} , (b) Q_T , (c) Q_{sc} , and (d) Q_{ab} as a function of wavelength for TiN bow tie-shaped nanoparticle placed on top of a 10 nm thin Si_3N_4 on a Si substrate.

As can be seen in Table 5.3, the 30 nm thin films performed better as silicon nitride provided very low surface recombination velocities both on p-type and n-type cells. Hence, 30 nm thin silicon nitride had better performance for Q_{ab} for all nanoplates with the shapes of triangle, bowtie, and bowtie with 60 nm gap at the center. Among the shapes 30 nm Si_3N_4 film had highest Q_T of 11 Wm^{-2} for triangular and Q_{ab} had highest value of 4.75 Wm^{-2} for bowtie shaped nanoplate. Hence, optimizing the thickness of dielectric material improved the scattering and absorption characteristics.

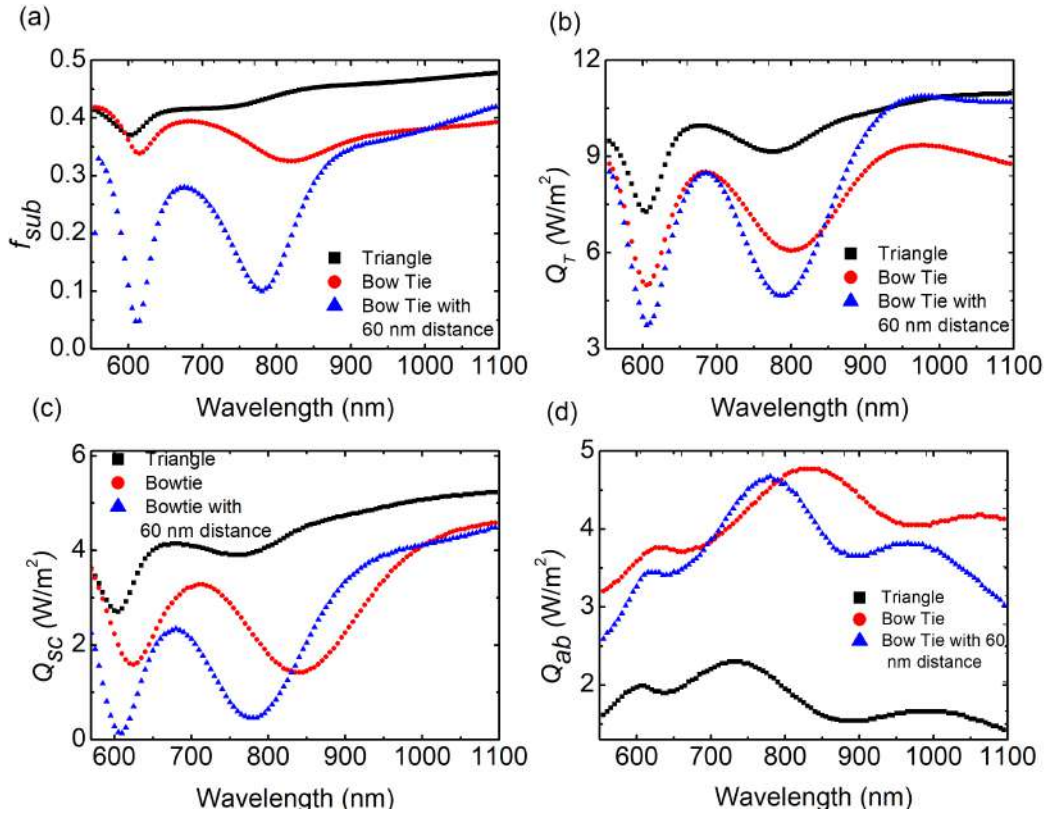


Figure 5.14: (a) f_{sub} , (b) Q_T , (c) Q_{sc} , and (d) Q_{ab} as a function of wavelength for TiN bowtie-shaped nanoparticles placed on top of a 30 thin Si_3N_4 on a Si substrate.

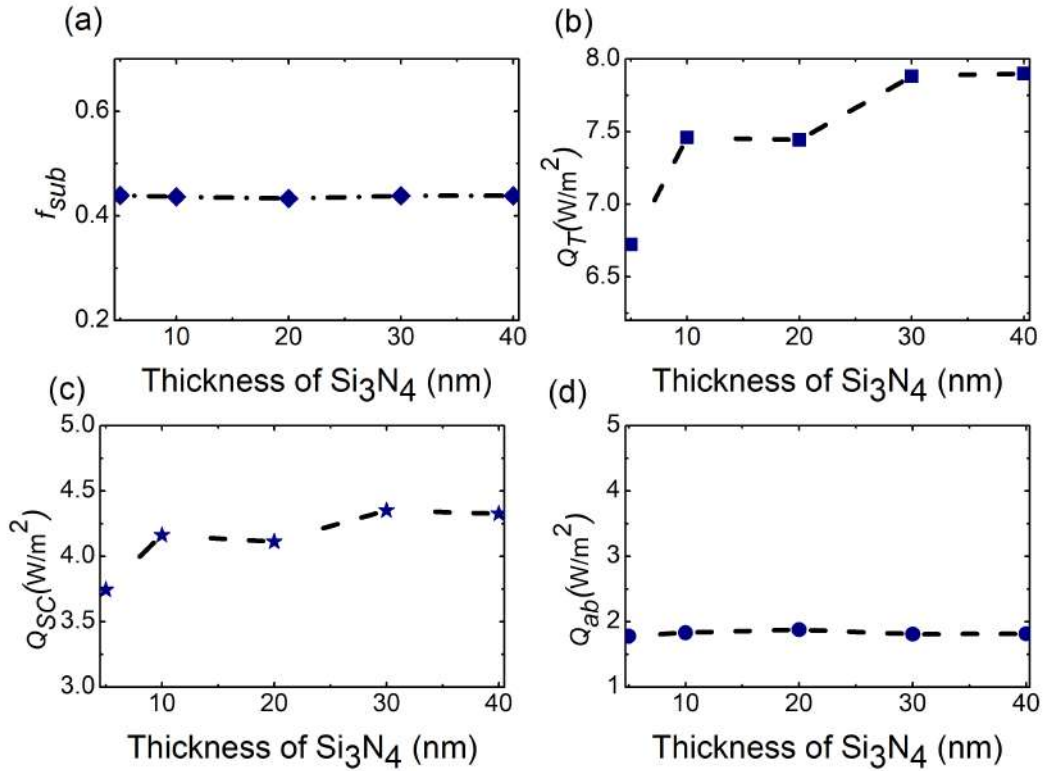


Figure 5.16: Average (a) f_{sub} , (b) Q_T , (c) Q_{sc} , and (d) Q_{ab} as a function of wavelength for TiN triangle shaped nanoparticle varying the thickness of dielectric material, Si_3N_4 on a Si substrate.

Chapter 6

Titanium Nitride Bowtie Nanoparticle Incorporated Kesterite Solar Cell

6.1 Introduction

Thin film PV has lightweight features and compatibility with tuning the light spectrum response for single-junction and tandem devices, and support for opaque and semitransparent structures which are all suitable and efficient as a result, it provides greater versatility than Si PV. [43, 116]. Kesterite $\text{Cu}_2\text{ZnSn}(\text{S},\text{Se})_4$ (CZTSSe) materials have emerged as the most successful thin film among Se, SnS, Cu_xS , FeS_2 , Cu_2SnS_3 , Cu_2O , and $\text{Sb}_2(\text{S},\text{Se})_3$ due to the components that are earth-abundant and toxic-free. Kesterite belongs to the adamantine family of chalcogenides but is free from toxic components [7, 38]. High absorption coefficient and adjustable band gap energy between optimal regions from 1.0 to 1.5 eV are inherited in kesterite-based materials. To create a compatible photovoltaic technology, less harmful and less expensive materials must be used. [10] while maintaining the advantages of the chalcopyrite and CdTe materials are desirable. Kesterite-based Thin-film solar cells made of $\text{Cu}_2\text{ZnSn}(\text{S},\text{Se})_4$ (CZTSSe) offer suitable direct band gap tunability over the solar spectrum, good device performance, and compatibility with low-cost production [5, 42]. Due to harmful deep-level defects, defect clusters with low formation energy, often occurring horizontal grain boundaries, and band gap/electrostatic potential fluctuation, the kesterite absorber exhibits non-radiative recombination and band gap contraction. Various methods have been developed to address the aforementioned issues and prepare high-efficiency kesterite solar cells such as plasmonics, adding an up-down converter layer as an additional absorber, doping/ alloying, defects regulation, thermal treatment, crystallization pathway intervention, and band gap manipulation [41, 43]. With the use of metamaterials in transformation optics, nanophotonics has demonstrated astounding performance during the past decade [45, 47, 117]. This additional tunability in particle array design allows us to employ

the entire spectrum of solar cells since the scattering cross-section of the particles is sensitive to the thickness of a spacer layer at the substrate [52, 84]. Alternative materials can be a promising nanoparticle to overcome the shortcomings of the metals [16, 17, 89]. Tantalum and titanium nitrides are well known metal nitrides that exhibit metallic characteristics at longer and visible wavelengths [17, 18].

In chapters 3, 4, and 5 we studied the optical properties of photovoltaic for different plasmonic shapes on Si substrate. In this chapter, we analyzed the optical and electrical properties of varying plasmonic shapes on kesterite solar cells. In this chapter, we systematically studied current density-voltage (I-V) and power-voltage (P-V) characteristic curves and absorption enhancement of kesterite (CZTS) substrate by incorporating TiN nanoparticles using the drift-diffusion and poisson equations. Our primary focus was to design and develop an alternative plasmonic (TiN) embedded Kesterite thin film solar cell by adding an up-conversion layer for better spectra utilization and comparing their performances by varying different parameters of the model. At first, we performed a comparative analysis of the performance of sphere and bow-tie-shaped TiN nanoplates. Afterward, we designed an optimized solar cell model, which was composed of alternative plasmonic material titanium nitride (TiN) based nanoparticle embedded on a semi-infinite crystalline CZTS solar cell and cascaded an up-converter layer added CZTS solar cell. TiN shows localized surface plasmon phenomenon and cost-effectiveness and CZTS is an intensively used semiconductor. The plasmonic particles and the semi-infinite kesterite absorber layer will be separated by this thin nitride layer. Moreover, we determined the efficiency and compared the performance of solar cell absorption efficiency with and without plasmonic, CZTS film. Our study will be beneficial for improved light trapping efficiency and proper spectra utilization in photovoltaic applications.

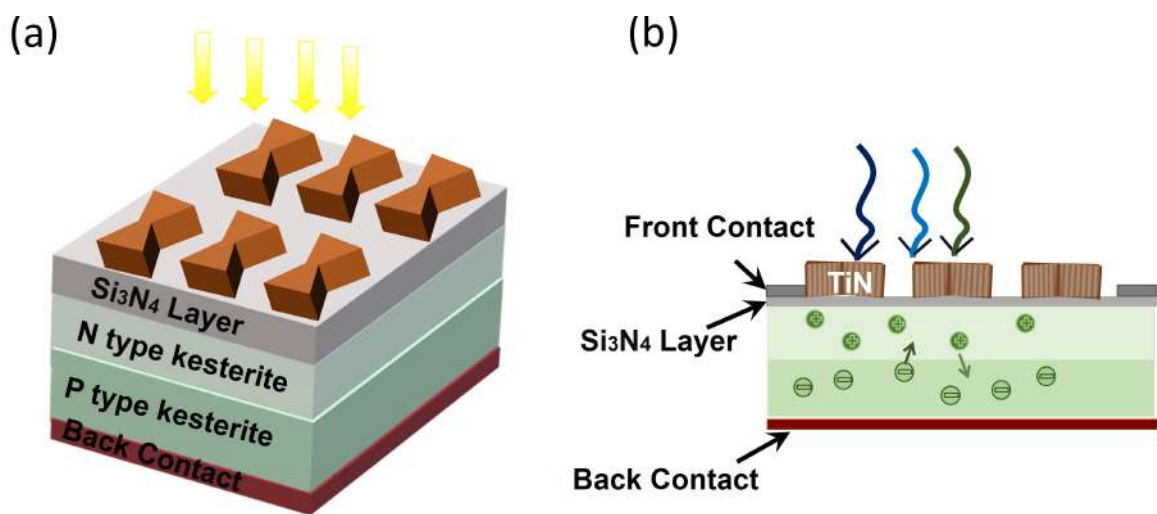


Figure 6.1: (a) Illustration of different shapes TiN nanoparticle on a 10 nm thin Si_3N_4 under-layer on kesterite solar cell.

6.2 Photovoltaic Nanostructure Design and Simulation Methods

6.2.1 Structural Design

We designed a solar cell embedded in TiN NP atop a layer of kesterite absorber with an additional layer of upconverter presented in Figure 6.1. TiN is a leading candidate for an alternate plasmonic material because of its metallic characteristics and localized surface plasmon events. The earth-abundant and environmentally safe component known as the absorber layer Kesterite (CZTS) has been hailed as a promising solar energy collecting material for cost-efficient and environmentally friendly photovoltaic applications. The physical properties of the CZTS were collected [118] and utilized in this study, To separate the absorber and NP a passivation layer Si_3N_4 has been used. To discover the efficient performances of the NP the shape and size of the particles were varied and their properties were analyzed. We analyzed dimer and monomer nanospheres and bow-tie-shaped nanoplates. The thickness of the thin film and absorber layer was presented by t_1 and t_2 , respectively and t_1 was considered to be 10 nm. L denoted the side length, and h represented the thickness of the triangles of the bowtie nanoplates. The polarization angle of the source was defined by θ , and r represented the radius of the dimer or monomer sphere.

6.2.2 Simulation Methods

We studied the aforementioned nanosystems for semiconductor devices and numerically solved the drift-diffusion and Poisson models in three dimensions. For electrons and holes (carriers), the drift-diffusion equations are provided by (2.26) to (2.28) Each carrier (hole or electron) moves as a result of two opposing processes: random thermal diffusion caused by the density gradient and drift caused by the applied electric field. As a function of temperature, impurity or doping concentration, carrier concentration, and electric field, mobility is a key component of the material model.

For evaluation of electrical properties, we simulated from the center of the emitter to the center of the absorbing CZTS, assuming the electrical period was $20 \mu\text{m}$, which was optimized to have optimal output power with the giving optical absorption. The simulated illuminated CZTS region was $9 \mu\text{m}$ wide, centered at $x=5.5\mu\text{m}$. We simulated the CZTS centered at $z=-1.5\mu\text{m}$ to import and position the generated electron data collected from the FDTD method for the solar spectrum (AM 1.5). The surrounding conditions were represented by a non-uniform mesh. The mesh size used for the nanoparticle was $0.05 \mu\text{m}$. A Si_3N_4 anti-reflection coating layer was applied in front of the surface to increase absorption,

and the absorption was noticeably improved in shorter wavelength areas. The quantity of photons absorbed per unit volume can be calculated by dividing the absorption as a function of frequency and space, P_{abs} , by the energy per photon, represented as,

$$G = \frac{P_{abs}}{\hbar\omega}. \quad (6.1)$$

The integration of G over the simulated spectrum determines the generation rate. The photo-generation current, I can be obtained assuming that all absorbed photons produce electron-hole pairs.

$$I = eG. \quad (6.2)$$

The quantum efficiency of a solar cell, $QE(\lambda)$, is defined by,

$$QE(\lambda) = \frac{p_{abs}(\lambda)}{P_{in}(\lambda)}. \quad (6.3)$$

where $P_{in}(\lambda)$ and $p_{abs}(\lambda)$ are the powers of the incident light and absorbed light within the CZTS solar cell, respectively, at a wavelength λ . We calculated the absorbed power after adding each layer, p_{abs} , power-voltage ($P - V$), and current density-voltage ($J - V$) characteristics to compare the suitable shape and size for better performances. We undertook different shapes and finally reached the conclusion to further explore bowtie-shaped NP. For the selection of suitable nanoparticle geometry with an appropriate plasmonic material in kesterite-based solar cells to enhance path length and consequently, to improve absorption, a comprehensive study of kesterite-based plasmonic solar cells is crucial. For different design parameters, we collected data for kesterite [118] and Si [105] from literature.

6.3 Results and Discussions

6.3.1 Current Density-Voltage and Power-Voltage Characteristics for Different Shaped NP

We considered monomer spherical, dimer spherical, and bowtie-shaped TiN NPs on CZTS thin film-based solar cells and found that bowtie-shaped had the best electrical performance. Afterward, we varied the thickness of the nanoplates from 50 nm to 150 nm and compared the $J - V$ and $P - V$ characteristics as can be seen in Figure 6.2(a)-(b). As can be seen in Figure 6.2, when there was no nanoparticle, the bare solar cell had the lowest efficiency and lowest J_{sc} and maximum power, P_{max} . After the incorporation of bowtie-shaped TiN

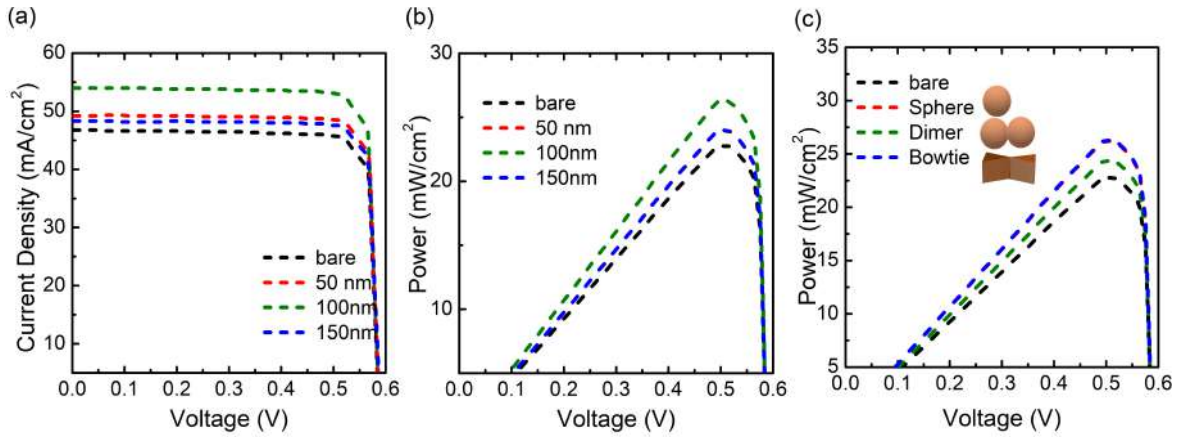


Figure 6.2: (a) Current density-voltage characteristic and (b) Power-voltage of bowtie-shaped TiN NP on CZTS solar cells. (c) Comparative power-voltage characteristics curves for the bare, spherical, dimer of spherical, and bowtie-shaped NP incorporated CZTS solar cells.

NPs, the J_{sc} and P_{max} increased. As we increased the h from 50 nm to 100 nm, the J_{sc} and P_{max} increased. When we further increased the value of h to 150 nm, the J_{sc} and P_{max} decreased. Due to the large area occupied by 150 nm thick NP, it absorbed a portion of the light that could not reach to absorber layer, and the total scattering decreased. Therefore, light absorption decreased, and electron-hole (e-h) generation decreased, resulting in J_{sc} decrement. As an optimal size of NP of 100 nm, it had the highest efficiency and highest J_{sc} and the optimum thickness for bowtie-shaped NPs in solar cells.

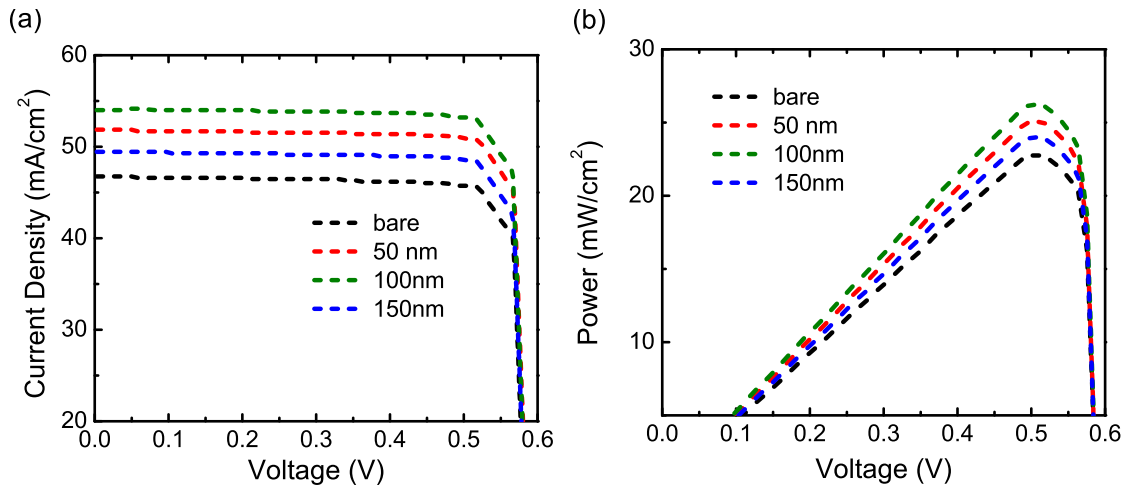


Figure 6.3: (a) Current density-voltage and (b) power-voltage characteristic of monomer shaped TiN NP on CZTS cell.

We calculated the electric properties of monomer spherical, dimer spherical, and bowtie-shaped TiN NPs on CZTS thin film-based solar cells varying the size. As can be seen in Figures 6.3(a)-(b) After the incorporation of TiN NP the J_{sc} and P_{max} increased. As we increased the r from 50 nm to 100 nm the J_{sc} and P_{max} increased. When r increased from

100 nm to 150 nm the J_{sc} and P_{max} decreased. Due to the increase of the radius of 150 nm NP, it absorbed a portion of the light that cannot reach to substrate layer and the light scattered into the substrate decreased, therefore, electron-hole (e-h) generation decreased and the J_{sc} decreased. Therefore 100 nm radius monomer had the highest efficiency.

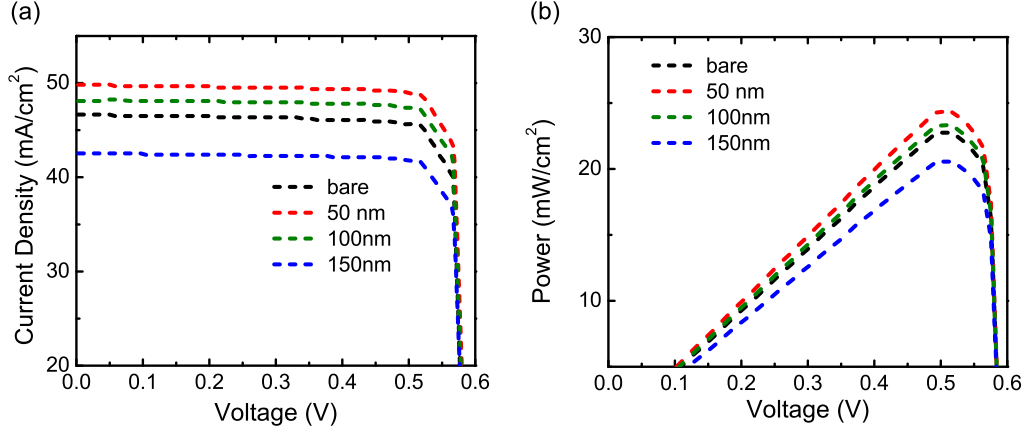


Figure 6.4: (a) Current density-voltage and (b) power-voltage characteristic of dimer shaped TiN NP on CZTS substrate cells.

With the incorporation of dimer NPs the P_{max} increased. As the radius of the dimers increased J_{sc} and P_{max} decreased observed in Figures 6.4(a)-(b). As the radius increased from 50 nm to 100 nm and 150 nm the total area increased and total scattering decreased and field enhancement decreased Therefore J_{sc} decreased. When $r = 150$ nm the scattering decreased largely and e-h pair generation decreased so much that the J_{sc} and P_{max} had less value than that of CZTS solar cell without any dimer NPs. The 50 nm radius dimer NP is optimum for kesterite solar cells.

Table 6.1: Comparison of electrical Properties of various shape and size of kesterite solar cells

Shape	Size (nm)	V_{oc} (V)	J_{sc} (mA/cm ²)	FF	η (%)
Bowtie	50	0.586	49.33	0.828	23.96
Bowtie	100	0.588	54.01	0.826	26.27
Bowtie	150	0.586	49.36	0.828	23.98
Sphere	50	0.587	51.51	0.827	25.04
Sphere	100	0.588	53.87	0.826	26.20
Sphere	150	0.586	49.36	0.828	23.98
Dimer	50	0.586	50.11	0.827	24.35
Dimer	100	0.586	48.02	0.828	23.32
Dimer	150	0.584	42.40	0.829	20.56

The electrical performance of the cell for different shapes and sizes was calculated from (2.16) to (2.19) was presented in Figure 6.2(c) Table 6.1 respectively. 100 nm thick bowtie, 100 nm radius monomer and 50 nm radius dimers were the optimum choice for kesterite

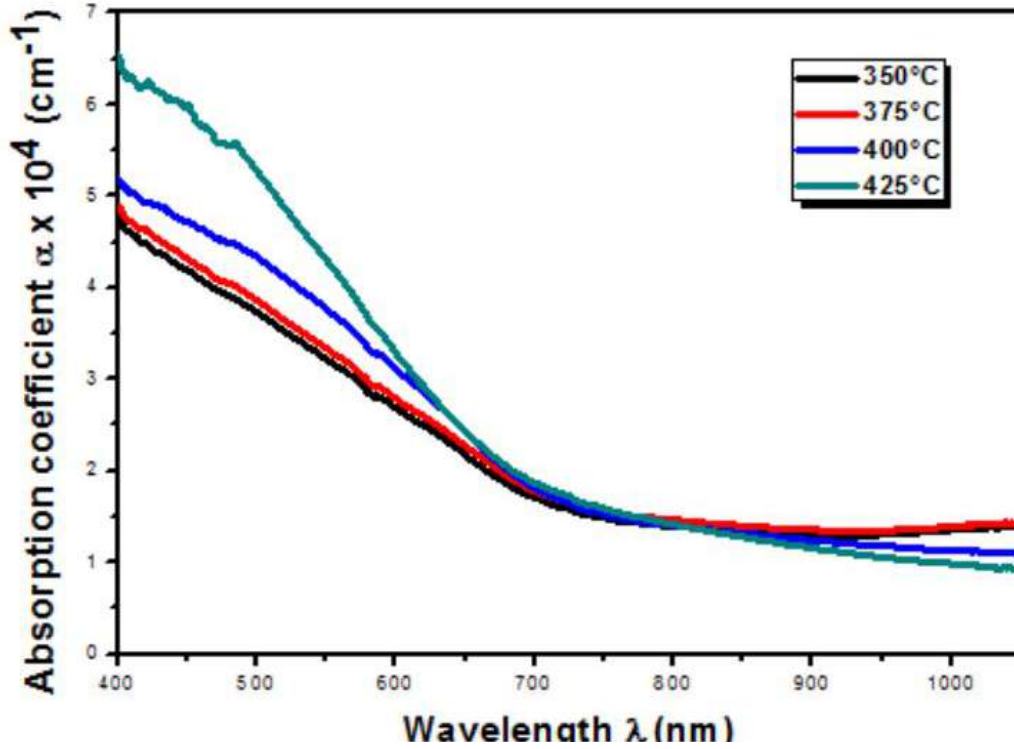


Figure 6.5: Absorption data versus wavelength λ for CZTS absorber material [119]

solar cells as they had the highest efficiency. For $h=100$ nm bowtie NP incorporated CZTS solar cell, open circuit voltage, $V_{oc} = 0.588$ V, $J_{sc} = 54.01$ mA/cm², maximum power, $P_{max} = 26.27$ mW/cm², fill factor, FF = 0.826, power conversion efficiency, $\eta = 26.27$ %. For 100 nm monomer incorporated cell, $V_{oc} = 0.588$ V, $J_{sc} = 53.87$ mA/cm², $P_{max} = 26.20$ mW/cm², FF = 0.826, $\eta = 26.20$ % and for 50 nm dimer incorporated cell, $V_{oc} = 0.586$ V, $J_{sc} = 50.11$ mA/cm², $P_{max} = 24.35$ mW/cm², $\eta = 24.35$ %, FF = 0.827. 100 nm radius monomer and 100 nm thick bowtie-shaped NP had comparable efficiency, V_{oc} and J_{sc} . Therefore to maximize the performance, we further explored CZTS cells with bow-tie-shaped nanoplate and monomer-shaped NPs.

We considered the bandgap 1.5 eV for the CZTS absorber layer. Our calculated open circuit voltage is 0.588 V, and the experimental open circuit voltage for CZTS solar cell carried from 0.4 V to 0.7 V [120]. Our calculated results i.e., open circuit voltage, agreed well with the experimental reports. The calculated open circuit current was slightly larger than the solar cell limit current based on only above bandgap absorption. This occurred due to the fact that the kesterite has absorption for wavelength longer than 1100 nm and it does not become zero. As can be seen in Figure 6.5 after 80 nm wavelength it reaches a saturation point and does not decrease. Because of the presence of the long tail in the absorption and n , κ graph (presented in Fig.6.6) the calculated current exhibit the solar cell limit. The electrical parameters used for the simulation are presented in Table 6.2 and 6.3

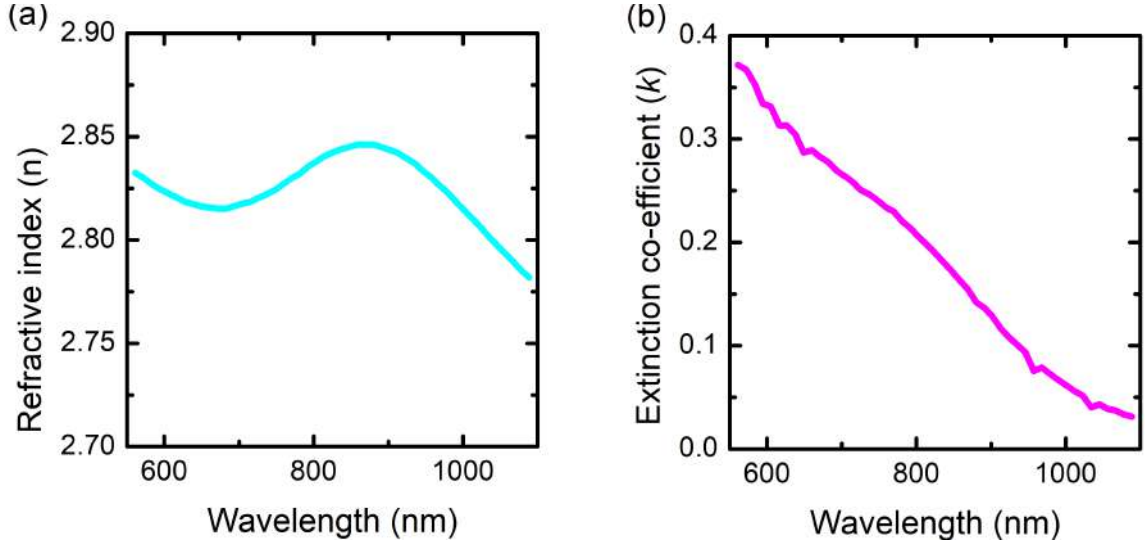


Figure 6.6: (a) Refractive index and (b) extinction co-efficient of CZTS [118]

Table 6.2: Electrical parameters of materials used in simulation

Material	Bandgap (eV)	DC Permittivity	Electric Conductivity (s/m)
Silicon	1.05	11.7	3.11×10^{-4}
Si_3N_4	5.09	7.5	1×10^{-13}
TiN	3.4	8	4×10^6
CZTS	1.5	10	18.3

6.3.2 Light Absorption Enhancement in Photovoltaic Cells by the NPs

We calculated the absorbed power and fraction of light scatter into the substrate, f_{sub} for different thicknesses of the bow tie and different radii of the sphere on Si and kesterite PV cells. Our other focal point was to estimate the performance of the kesterite absorber layer compared to the Si absorber layer. We simulated the optical properties of both cells and discovered a better-embedded system with maximum efficiency.

Path length enhancement is crucial for measuring the effectiveness of light trapping in the absorber layer. The path length enhancement largely depends on the fraction of light scattered into the substrate, f_{sub} , which is the ratio of the power in the scattered field region inside the substrate of the absorber layer to the power in the scattered field region in the air and the absorber layer. The effect of diagonal propagation through the device, d_{av} , is the ratio of the optical path length over one pass of the device to the device's thickness, averaged over the angular distribution of light. The d_{av} was determined by performing a weighted integral of $\frac{1}{\cos\theta}$ over the angular distribution of the scattered power, with θ as the angle with the normal. The maximum path length enhancement can be calculated from (3.9). From this equation, we calculated the path length enhancement for 100 nm thick TiN bowtie-shaped

Table 6.3: Electrical parameters used in simulation in the proposed solar cell

Parameters	Unit	Value
Electron Velocity	cm/s	1×10^7
Hole Velocity	cm/s	1×10^7
P-type constant doping	cm^{-3}	2×10^{16}
P-type diffusion doping	cm^{-3}	2×10^{20}
P-type diffusion junction width	μm	0.02
N-type diffusion doping	cm^{-3}	1×10^{19}
N-type diffusion Junction width	μm	0.04

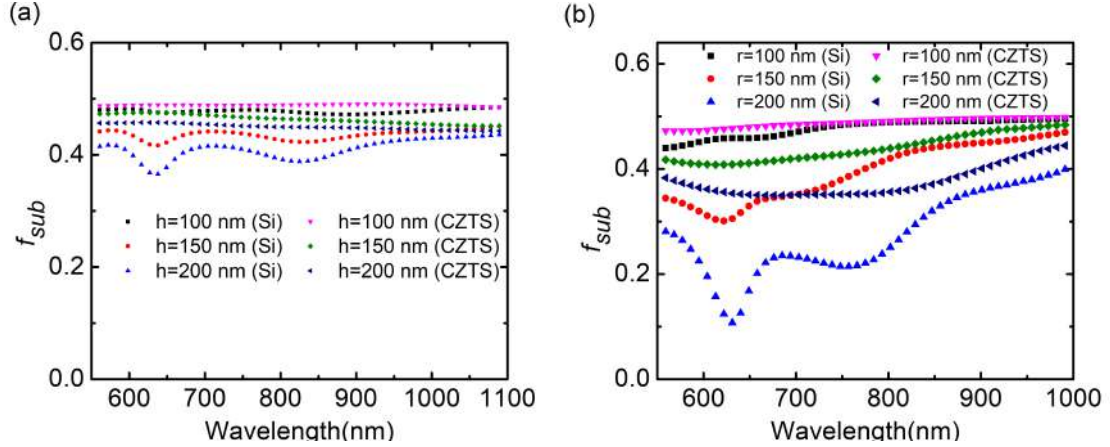


Figure 6.7: f_{sub} as a function of wavelength for (a) TiN bowtie NPs varying the thickness, $h = 100, 150,$ and 200 nm, (b) TiN monomer-spherical NPs with radius, $r = 100, 150,$ and 200 nm placed on top of a 10 nm Si_3N_4 on a Si and CZTS cells.

NP and 100 nm radius monomer, which were 2.48 and 2.38 , respectively.

We calculated the f_{sub} varying the thickness, h of the bowtie-shaped NP in both silicon and kesterite solar cells as can be seen in Figure 6.7(a). When the h increased, the f_{sub} decreased for both absorber layers. For $h = 150$ nm and 200 nm, there is a significant difference in the f_{sub} values for the Si and CZTS cells. The CZTS solar cell has better f_{sub} . We varied the radius of the TiN monomer on the Si and CZTS cells and compared the f_{sub} values. Similar to Figure 6.7(a), the kesterite cells performed better and with the increase of radius f_{sub} decreased as observed in Figure 6.7(b). We further compared the performance of the TiN monomer-shaped nanosphere and bowtie-shaped nanoplate, and bowtie-shaped nanoplate had a higher average f_{sub} of 0.49 for $h=100$ nm than that of the monomer-shaped nanosphere.

We calculated the absorbed power of each layer of nanostructure consisting of monomer spherical NP and bowtie-shaped nanoplate embedded on 10 nm Si_3N_4 layer on top of the absorber layer [103, 121]. Here, $L = 200$ nm, $h = 100$ nm and $r = 100$ nm. To compare the performance of the kesterite (CZTS) cell with the silicon cell, we presented the absorbed power of each layer as can be seen in Figure 6.8. The divergence of the Poynting vector was

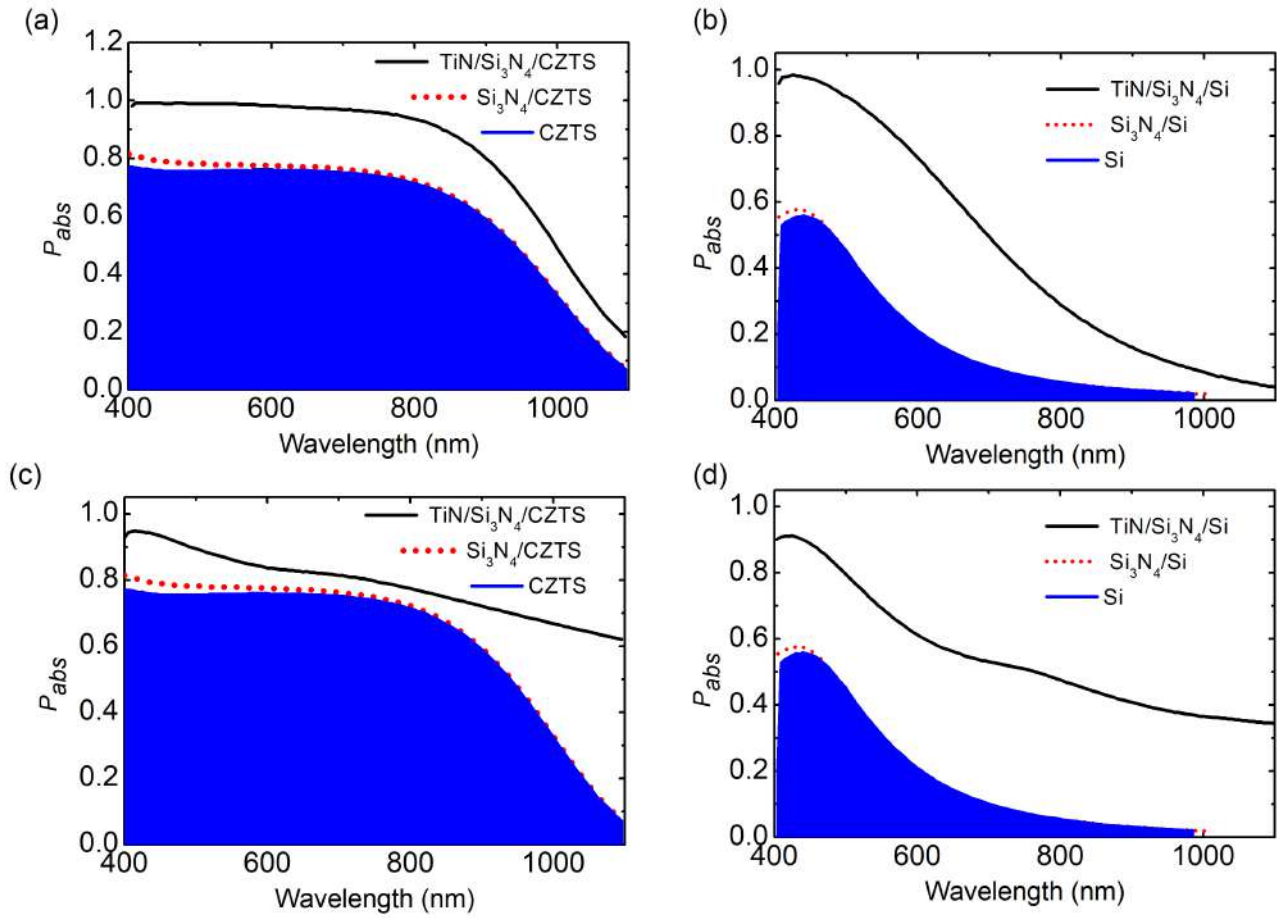


Figure 6.8: Percentage of power absorbed in each layer of TiN nanosphere on (a) CZTS, (b) Si, substrate. Percentage of power absorbed in each layer of TiN bowtie-shaped nanoplate on (a) CZTS, (b) Si substrate.

used to compute the absorption per unit volume. We calculated from (3.6) to (3.8). Bare silicon cells had an average absorption power of $\sim 19\%$, whereas bare kesterite cells had an average absorption power of $\sim 61\%$. The Si_3N_4 layer enhanced the absorption barely over the spectral range. After the incorporation of TiN NPs, the absorbed power increased significantly over the whole spectral range. The absorbed power for TiN NP incorporated kesterite cells was enhanced the average absorption from $\sim 61\%$ to $\sim 88\%$ for bowtie-shaped NPs and $\sim 78\%$ for monomer NPs Whereas, the absorbed power increased from $\sim 19\%$ to $\sim 54\%$ for bowtie shaped NPs and $\sim 45\%$ for monomer NPs incorporated Si cells. As shown in Figures 6.7, and 6.8, the bowtie shape NP had better scattering performances and power absorption than monomer-shaped NP. Therefore, we further explored bowtie-shaped NP-incorporated kesterite cells.

The absorption enhancement, g , light absorption efficiency, LAE are defined to show how a solar cell with metal particles performs in comparison to a bare solar cell. The g can be calculated from (4.4). We calculated g for the different h of TiN plasmonic bowtie on a

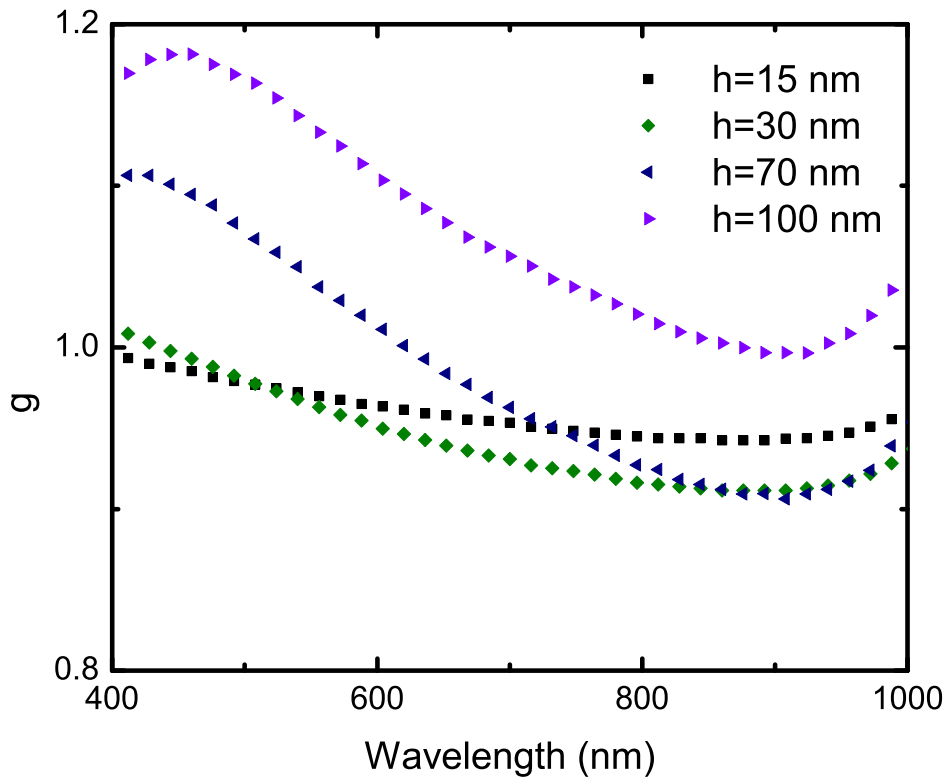


Figure 6.9: Absorption enhancement, g for bowtie-shaped TiN plasmonic nanoplates with $h = 15, 30, 70$ and 100 nm.

kesterite substrate as shown in Figure 6.9. The g increased with the h for wavelength from 400 nm to 700 nm. This occurred due to the strong forward scattering of light, the forward scattering enhanced absorption, whereas the backward scattering prohibited absorption. For $h = 15$ nm, the absorption was greater ~ 0.95 for the whole wavelength range. When h was increased to 30 nm, the g increased for 400 - 500 wavelength range and it decreased for longer wavelengths. For $h = 70$ nm, the enhancement was 1.1 for 400 nm to 780 nm. As we further increased h to 100 nm, the g was greater than 1 for the whole spectral range, and the maximum value was ~ 1.2 . The average enhancement, G , was estimated to be 1.13 for $h = 100$ nm. The light scattering and enhancement results are presented in Table 6.4

We calculated the normalized reflection, R , transmission, T and absorption, A spectra for $L = 200$ nm and $h = 100$ nm bowtie-shaped nanoplate on a CZTS absorber layer presented in Figure 6.10 (a). Here the fraction of light transmitted to the substrate is 38% , absorption is greater than transmission and reflection is negligible. Standard 1.5 ATM solar spectrum and absorption of TiN NP-based solar cell are presented in Figure 6.10(b). Solar light absorption is very efficient for wavelengths shorter wavelength till 450 nm. For longer wavelengths than 500 nm, the absorption decreased gradually. This phenomenon affects the efficiency of the

Table 6.4: Light absorption enhancement on 100 nm bowtie-shaped NPs incorporated cells

Performance Parameter	Unit	Value
Average f_{sub}		0.49
Path length enhancement		2.48
Average absorption of kesterite cell	%	88
Average absorption of Si cell	%	54
g_{max}		1.2
G		1.13
LAE	%	76.92

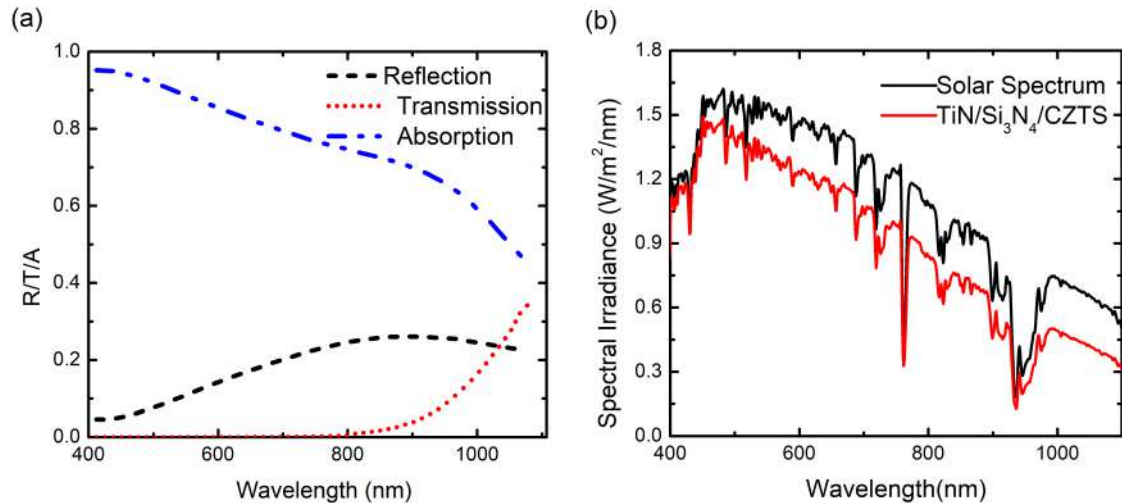


Figure 6.10: (a) Reflection, transmission, and absorption of TiN bowtie-shaped nanoplates based CZTS solar cell. (b) Absorption spectra of bowtie-shaped TiN NP incorporated CZTS absorber layer and Solar irradiance spectra.

solar cell. The thin film solar cell can not trap light efficiently for the higher wavelength and causes transmission loss. To overcome the loss we added up a converter layer solar cell to improve the light trapping for larger wavelengths and overall improve the efficiency of the solar cell.

The light absorption efficiency was calculated from (4.2) to (4.3). For the TiN plasmonic bowtie nanoplates on a kesterite cell, we determined LAE. The value of LAE for 100 nm thick bowtie-shaped NP was found to be 76.92 %.

6.3.3 Light Polarization Sensitivity of Bowtie-shaped NP Incorporated CZTS Solar Cells

The bowtie-shaped TiN NPs showed light polarization sensitivity [103, 121]. Therefore, we calculated the optical properties of bowtie-shaped TiN NPs by varying the polarization angle of the light source, θ as can be seen in Figure 6.11. The θ was varied from 0° to 45° and $L=200$ nm and $h=100$ nm on both silicon and kesterite cells. When TiN NP was embedded

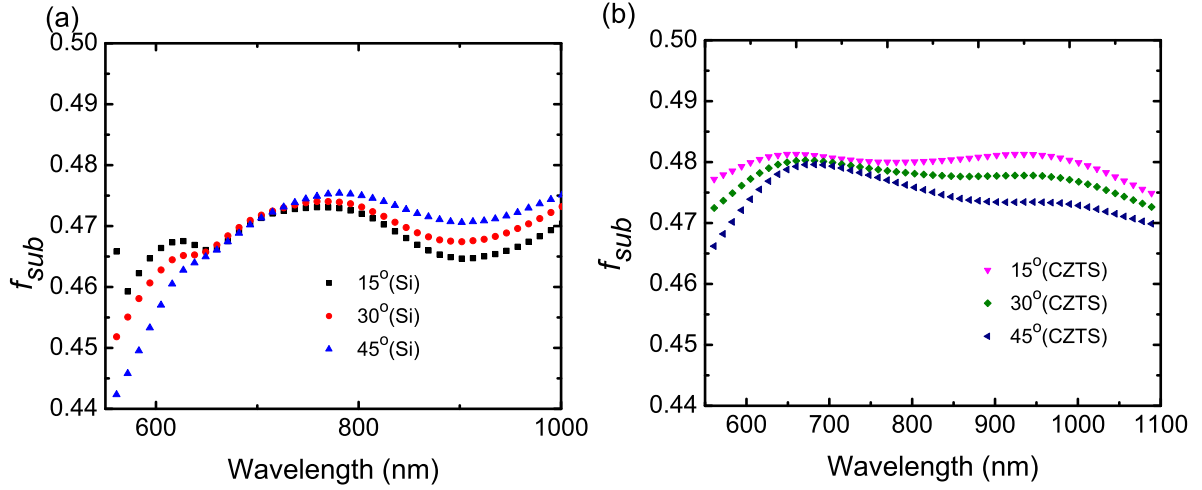


Figure 6.11: f_{sub} for TiN bowtie-shaped nanoplates varying the polarization angle of the source for from $\theta=15^\circ$ to 90° on a 10 nm Si_3N_4 on top of (a) Si and (b) CZTS solar cells.

in the CZTS cell, the f_{sub} decreased with the increase of θ . On the other hand, the f_{sub} increased with the increase of θ for Si cells. For the comparison of f_{sub} for kesterite and Si solar cells, the kesterite solar cell had better light-trapping properties.

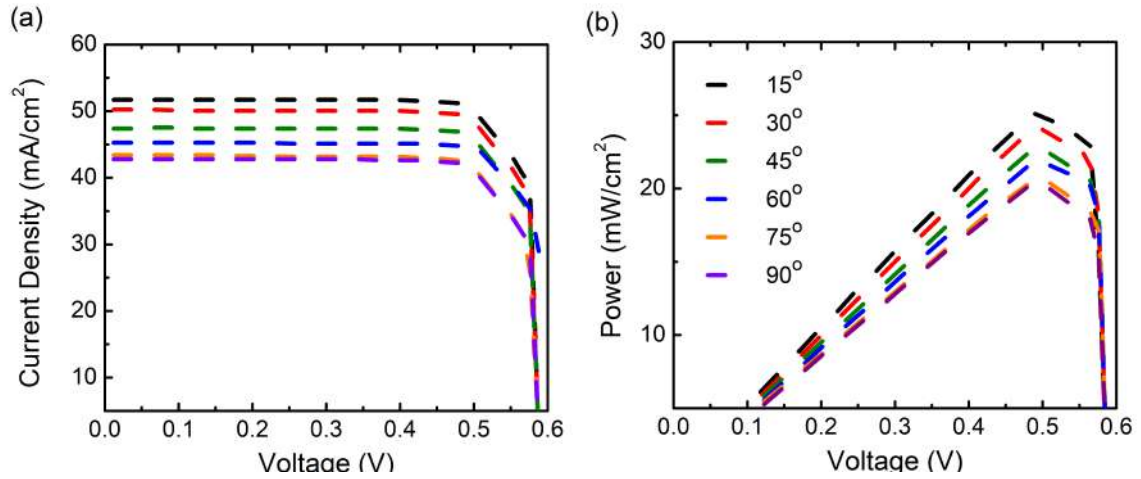


Figure 6.12: (a) Current density-voltage and (b) power-voltage characteristics of bowtie-shaped TiN NP on CZTS solar cells for various θ . The θ was varied from 15° to 90° .

We calculated the current density-voltage and power-voltage characteristics varying the polarization angle of the light source presented in Figure 6.12. As θ increased from 0° to 90° the current density decreased, and maximum power and efficiency decreased, keeping consistency with Figure 6.11. As the polarization angle increased, the light scatter into the substrate decreased in the CZTS absorber layer, and the e-h generation decreased, and consequently, current density decreased. As a result, maximum power and efficiency decreased as evident in Figure 6.12. For improved efficiency, the polarization angle should be kept to 0° .

Chapter 7

Upconverter Solar Cell

7.1 Introduction

Different strategies have been proposed in the literature to raise solar cell efficiency above the 30% theoretical ceiling set by Shockley and Queisser for conventional solar cells. Figure 7.1 illustrates the many losses that might occur in a normal solar cell due to reflection, recombination, resistive, and thermal losses. The most frequent loss occurs when photons with energies larger than the band gap of the material are absorbed, which causes the charge carriers to thermalize. Downconversion (DC) materials can be used to stop the thermalization of charge carriers. On the other hand, loss caused by photons with energy lower than the materials' band gap can be addressed with the aid of upconversion materials.

The conversion efficiency of solar cells is negatively impacted by the thermalization of high-energy photons and the transmission of low-energy photons in the solar spectrum. By modifying the solar spectrum via up-conversion and down-conversion processes, these issues can be solved. A further absorber layer called an up-down conversion layer can make it easier to achieve breakthroughs, which may be brought on by the interference of several different approaches [123]. By absorbing one visible photon with higher energy and producing two near-infrared photons with lower energy, upconversion continued the promising route in the area of light trapping of the solar spectrum [124]. Transmission or sub-bandgap losses refer to the inability of incident photons with energy below the threshold to contribute to the creation of electrons in the solar cell. Numerous types of up-converter materials based on luminescent ions or organic molecules are being investigated to improve the efficiency of up-conversion solar cells. By converting low-energy infrared photons, upconversion materials like Ln^{3+} ions doped glasses, glass ceramics, and phosphor can alter the incident solar spectrum to produce high energy near-infrared or visible photons with energies that are close to or equal to the energy gap of a Si solar cell [22]. Up-converter materials may be combined

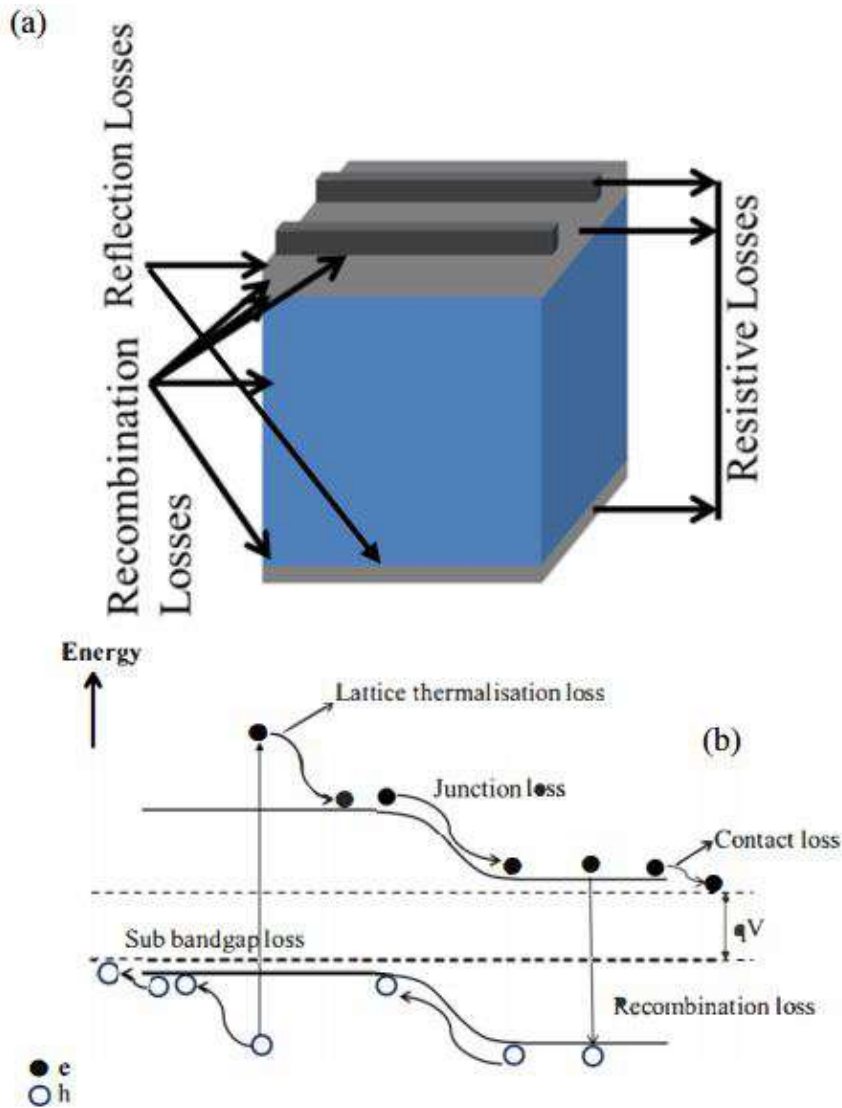


Figure 7.1: Different losses in a solar cell, (a) schematic diagram of a solar cell and (b) band diagram of a solar cell.

[122]

with plasmonic particles to increase light conversion efficiency and increase the viability of effective commercial solar cells.

The up-down conversion process, the up-down conversion layer in solar cells, suitable materials for up and down conversion solar cells, and the up converter's light absorption mechanism were all covered in this chapter. The design and development of an alternative plasmonic (TiN) embedded Kesterite thin film solar cell with an up-conversion layer for improved spectral utilization was our main goal. As described in Chapter 6, we considered bow-tie-shaped TiN nanoplates for the best efficiency. Afterward, we designed an optimized solar cell model, which was composed of alternative plasmonic material titanium nitride (TiN) based nanoparticle embedded on a semi-infinite crystalline CZTS solar cell and cascaded an up-converter layer added CZTS solar cell presented in Figure 7.2. More-

over, we determined the efficiency and compared the performance of solar cell absorption efficiency with plasmonic, CZTS film, and upconverter (UC) layer-incorporated cells.

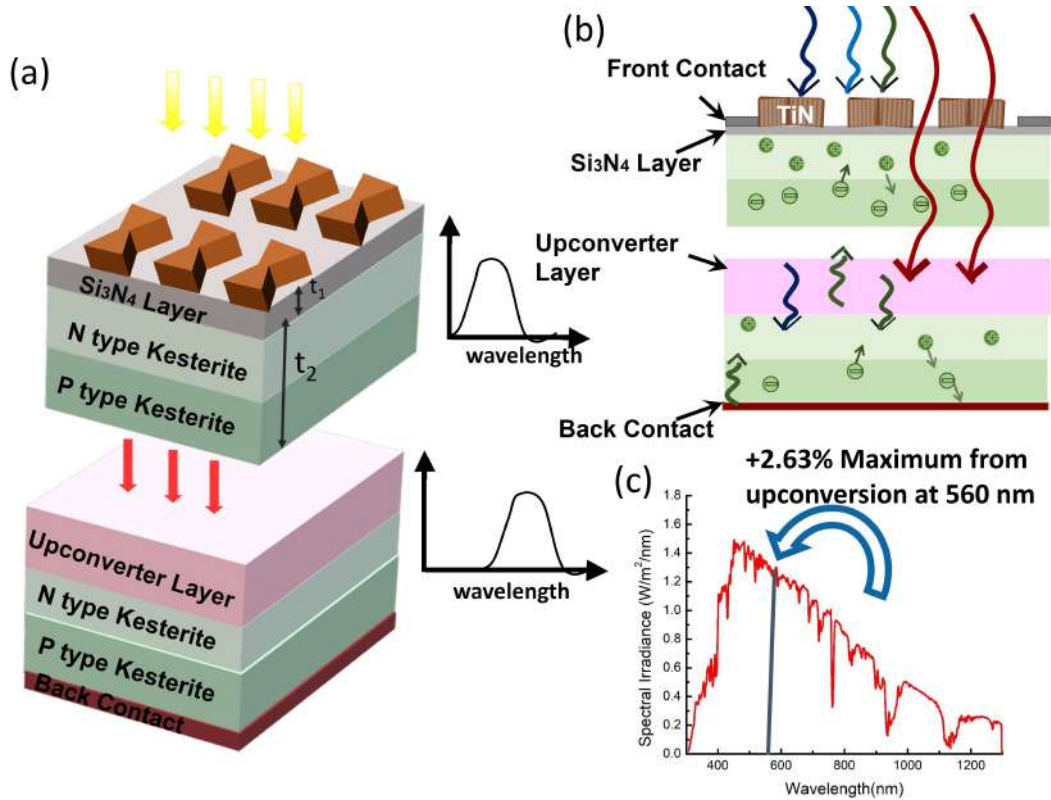


Figure 7.2: (a) Illustration of different shapes TiN nanoparticle on a 10 nm thin Si_3N_4 under-layer on kesterite solar cell incorporated with upconverter solar cell. (b) An illustration of the concept of a UC-enhanced device harvesting sub-bandgap photons via a UC layer located on a kesterite solar cell. (c) Absorption spectra of TiN dimer NP incorporated kesterite absorber layer in the air-mass 1.5 global (AM 1.5G) solar spectra, indicating the wavelength by a UC layer.

7.2 Upconversion Materials

The non-linear optical process known as upconversion converts a minimum of two low-energy photons (in the near-infrared region) into a high-energy photon (in the visible region). The best upconversion materials are those that work with large band-gap solar cells. Upconversion materials are used in a variety of applications, including light harvesting, displays, temperature sensors, solid-state lighting, optical data storage, and medicinal therapy. All types of solar cells such as crystalline, thin-film, and hybrid can use upconversion components. Figure 7.3 shows the energy diagram and the typical schematic structure of a solar cell with UP conversion materials. In general, the most prevalent two available material classes are taken into consideration when low-energy photons are subsequently absorbed to produce higher energy emission: (1) Metal ions, primarily lanthanide and transition metal

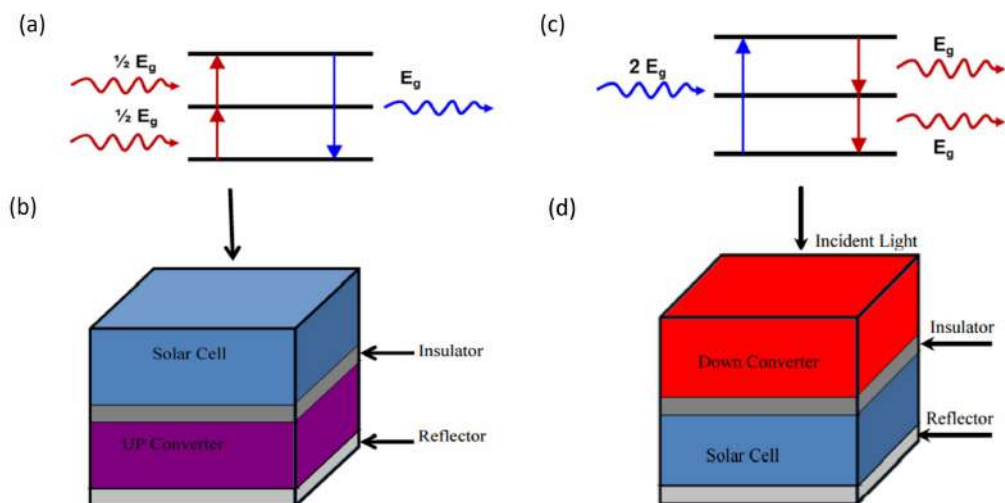


Figure 7.3: Upconversion process; two photons with energy $1/2 E_g \leq h\nu \leq E_g$ generate a photon with energy $h\nu \geq E_g$, where E_g denotes the band gap of the material and (b) A schematic diagram of a solar cell with UP converter. (c) Down conversion process; one photon with energy $h\nu \geq 2E_g$ yields two photons with $h\nu \geq E_g$ and (d) A schematic diagram of a solar cell with down converter.

[122]

ions, in inorganic host materials [71] and (2) extended conjugated organic chromophores with the π system [69].

7.2.1 Lanthanides

The group of elements known as lanthanides are those for which the 4f inner shell has up to 14 electrons. Lanthanide ions are typically trivalent (Ln^{3+}) and have a $4f^n 5s^2 5p^6$ electron configuration with $n=0-14$. The distinct optical and magnetic characteristics of lanthanide ions are a result of the partially filled 4f shell. There are 14 over n potential configurations for n electrons in the 14 accessible orbitals, and each configuration is capable of having a different energy. This gives rise to a rich energy level structure with energy levels in the NIR, VIS and UV spectral range. The 4f inner shell is protected by the outer 5s and 5p shells, thus the electronic transitions are not affected by the host materials around them. Depending on the application, the trivalent ions may be doped in a variety of host materials, ranging from fluorides to oxides.

The absorption lines are sharp and the transitions between various $4f^n$ states are parity prohibited (no change in dipole moment). The mixing of opposing parity states by odd-parity crystal field components or vibrations results in a modest opening of the transitions. The poor connection with the vibrations is what gives the spectral lines their sharpness. Optical transitions do not experience Stokes' shift, which dramatically reduces vibrational energy losses. Due to their wide range of absorption and emission wavelengths, independence from

host materials, and little vibrational energy losses, lanthanides are suitable ions for spectral conversion. As a result, the main source of emission in almost all artificial light sources is lanthanide ions. Lanthanides are doped into a variety of solids, such as crystals, fibers, and glass ceramics, to give them the required optical properties. To reduce multi-phonon relaxation between closely spaced energy levels, the ions are buried in hosts with low phonon energies. Low phonon host examples include fluorides, chlorides, iodides, and bromides, while high phonon host examples include oxides such as silicates, borates, and phosphates. Potential non-radiative transitions are influenced by the phonon energy, but the energy level structure is unaffected by the host materials. Although weak, coupling with phonons produces a non-radiative channel between energy levels that opposes radiative transitions. In general, nonradiative multiphonon relaxation will predominate when energy levels are separated by less than five times the host's maximum phonon energy, while radiative decay will predominate when there are energy disparities of five times or more.

7.2.2 Organic Molecules

Organic and organo-metallic chromophores are a second class of materials for which efficient upconversion has been proven. Recently, there has been a resurgence in interest in upconversion research in these chromophores. Organometallic complexes act as the sensitizer in the upconverters, which are composed of organic molecules with conjugated π systems acting as the acceptor. The sensitizer molecules feature a metal ion core and are characterized by metal-to-ligand charge transfer (MLCT) transitions. The activator molecules are composed of high fluorescence quantum yield organic compounds. The MLCT absorption band of the metal complex sensitizer is frequently in the green and red spectral region.

As can be seen in Figure 7.4 the photon upconversion in organic molecules is based on the triplet-triplet annihilation (TTA). Among other crucial requirements, the triplet and singlet excited states of the sensitizer must be nested between the triplet and singlet excited states of the activator. The sensitizer should therefore have a significantly smaller singlet-triplet splitting than the activator for MLCT transitions on the sensitizer and an aromatic hydrocarbon activator, which normally has a large singlet-triplet splitting. During the upconversion process, a sensitizer is initially excited to the lowest singlet state (strong absorption), and then it relaxes by intersystem crossover (ISC) to the triplet state. This approach, which is quicker than spontaneous emission from the singlet state, efficiently excites the triplet state. The long-lived triplet state of the sensitizer transfers its energy to the long-lived triplet state of the activator. Two activator molecules in the triplet state are destroyed, leaving one activator in the ground state and one activator in the high energy singlet state. We see upconverted emission coming from the activator's singlet state. Numerous energy relaxation mechanisms occur throughout the upconversion process, which reduces the blue shift of the upconverted

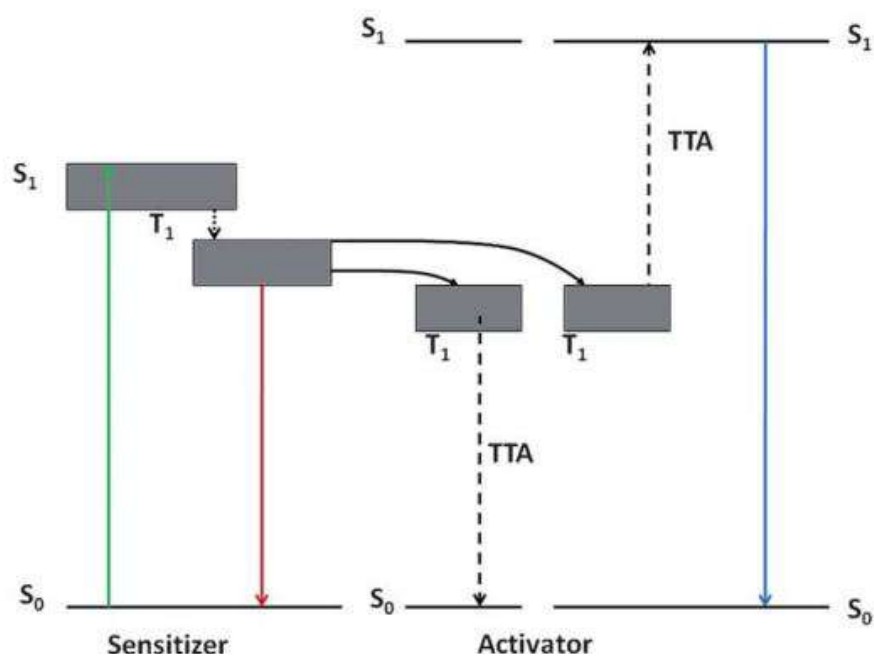


Figure 7.4: Energy scheme for upconversion in organic molecules. The singlet state of the sensitizer is excited and relaxes through a fast intersystem crossing to the triplet state of the sensitizer.

[69]

emission with respect to the excitation wavelength compared to what is seen for lanthanide upconverters. Usually, blue shifts between 100 and 200 nm are seen.

7.3 Downconversion Materials

A high-energy photon is divided into two lower-energy photons during down-conversion (DC). A high-energy photon is split into two lower-energy photons during this process, which is also referred to as quantum cutting. Smaller band gap solar cells are best suited for DC materials. Smaller band gap solar cells are best suited for DC materials. The energy diagram and the usual schematic layout of a solar cell made of DC materials are shown in Figure 7.3. DC materials are frequently used on the front side of solar cells, whereas the back side demands the use of a bifacial solar cell. Down conversion techniques provide 32% more spectral irradiance for Si solar cells. The Dy^{3+} -doped GdVO_4 , YF_3 : Pr^{3+} , Yb^{3+} , LiGDF_4 : Eu^{3+} are a few examples of the down-conversion materials. The Er-Yb co-dopen glass ceramics with a variable ratio of Er/Yb have been reported. They are simple to synthesize and offer the needed control over the material properties. By increasing the external quantum efficiency, they have discovered a material that is appropriate for solar cell applications. Different methods, including combustion, sol-gel emulsion, and sovothermal, have been utilized to synthesize these compounds in the down-conversion. Recently luminescence

rare earth ion doped materials are used for down-conversion.

7.4 Efficiency Improvement by Integration of Upconverter Layer

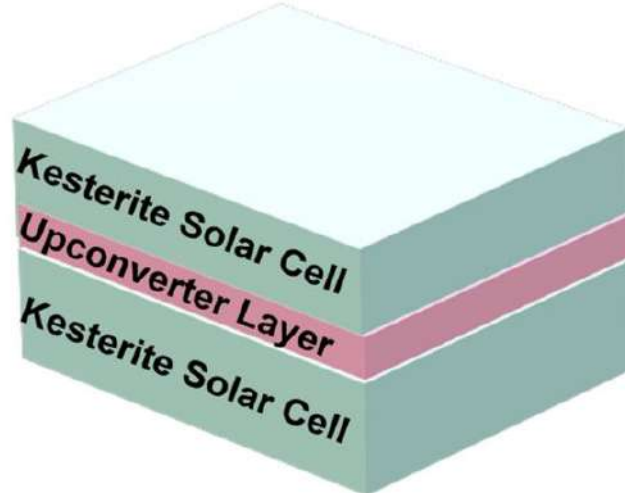


Figure 7.5: A schematic illustration of the system for upconversion.

We proposed an improved photovoltaic system involving an upconverter layer presented in Figure 7.5. The proposed model is based on plasmonic NPs on kesterite cell with the incorporation of upconverter layer and with another kesterite layer tandem cell presented in Figure 7.5. The upconverter layer, which partially transformed the sub-bandgap photons transmitted from the solar cell into high-energy photons, was the key component of this system.

Here we considered a kesterite absorber cell incorporating a yttrium aluminum garnet (YAG) upconverter. The photon current density absorbed in the solar cell without the upconverter layer can be calculated from,

$$N = \frac{A\Omega}{4\pi^3\hbar^2c^2} \int_{E_g}^{\infty} (\hbar\omega)^2 [\exp(\frac{\hbar\omega - \mu}{KT}) - 1]^{-1} d\hbar\omega. \quad (7.1)$$

Here, E_g is the band gap of the cell, T was the temperature of the emitter, K is the Boltzmann constant has a defined value of 1.380649×10^{-23} joule per kelvin and $\hbar\omega$ is the energy of the photon. The symbol $A\Omega$ signifies the etendue that depends on the square of the refractive index, n , and the half angle θ into which radiation can be emitted. The solar disk's small solid angle, which allows for the receipt of direct sunlight, is described by $A\Omega_s = 6.8 \times 10^{-5}$ for non-concentrated sunlight which is the incident photon. For the emission by a blackbody into the air and into a sphere $A\Omega = 4\pi$.

The UC system included the contribution of the external layer implementing spectral splitting. Since the UC layer is a standalone system, it can be studied independently of the solar cell beneath it. We presume that a UC layer was applied to the solar cell to enhance photon absorption. In turn, the photons that the solar cell collects are modified to include the external splitting of higher energy photons, and this modification can be described as,

$$N_{uc} = (1 + f_{uc}\theta) \frac{A\Omega}{4\pi^3\hbar^2c^2} \int_{E_g}^{\infty} (\hbar\omega)^2 [\exp(\frac{\hbar\omega - \mu}{KT}) - 1]^{-1} d\hbar\omega. \quad (7.2)$$

The modified spectrum appears as an additional fraction of $f_{uc} \times \theta$, where f_{uc} is the efficiency of UC, ranged from 0 to 1, and θ denotes the fraction of photons below E_g , it can be presented as

$$\theta(E_g) = \frac{\int_0^{E_g} (\hbar\omega)^2 [\exp(\frac{\hbar\omega - \mu}{KT}) - 1]^{-1} d\hbar\omega}{\int_{E_g}^{\infty} (\hbar\omega)^2 [\exp(\frac{\hbar\omega - \mu}{KT}) - 1]^{-1} d\hbar\omega}. \quad (7.3)$$

Table 7.1: Electrical performance of the nanoparticle and upconversion layer incorporated kesterite solar cell

Performance parameter	Unit	Value
V_{oc}	V	0.588
J_{sc}	mA/cm ²	54.01
FF		0.826
η_{NP}	%	26.27
η_{NP+CL}	%	28.90

We calculated the efficiency of the kesterite solar cell, then we inserted the upconverter layer and calculated the efficiency. We inserted erbium-doped YAG into kesterite cell. The percentage of upconversion layer efficiency, f_{uc} for this UC layer was reported to be 11% for the spectral range 400 nm to 1100 nm for 1.5 AM G [125]. The calculated results are presented in Table 7.1. YAG upconversion layer has the applications of upconversion from infrared (790 nm) to green (560 nm). For the whole solar spectrum, the incident number of photons was fixed. We calculated the efficiency of photon flux absorption increased by the incorporation of the upconverter layer from (7.1) and (7.5). The overall efficiency increased for the incorporation of the YAG upconverter layer was 2.63 % which increased the absorption of light with a wavelength of 790 nm and increased the efficiency of kesterite solar cells. The electrical parameter are presented in Table 7.1

7.5 Designing Different Absorber Layer for Tandem Solar Cell

We calculated the absorption power for the solar cell for different bottom tandem absorber layers. With the incorporation of an upconverter layer, the absorption enhancement increased. Ge had the highest absorption power with 0.66 eV bandgap energy; the absorption power decreased when Ge was replaced with Si and InAs. When we considered the second CZTS layer in the tandem cell, it performed better than the Si and InAs layer and very close to the Ge layer, as presented in Figure 7.6.

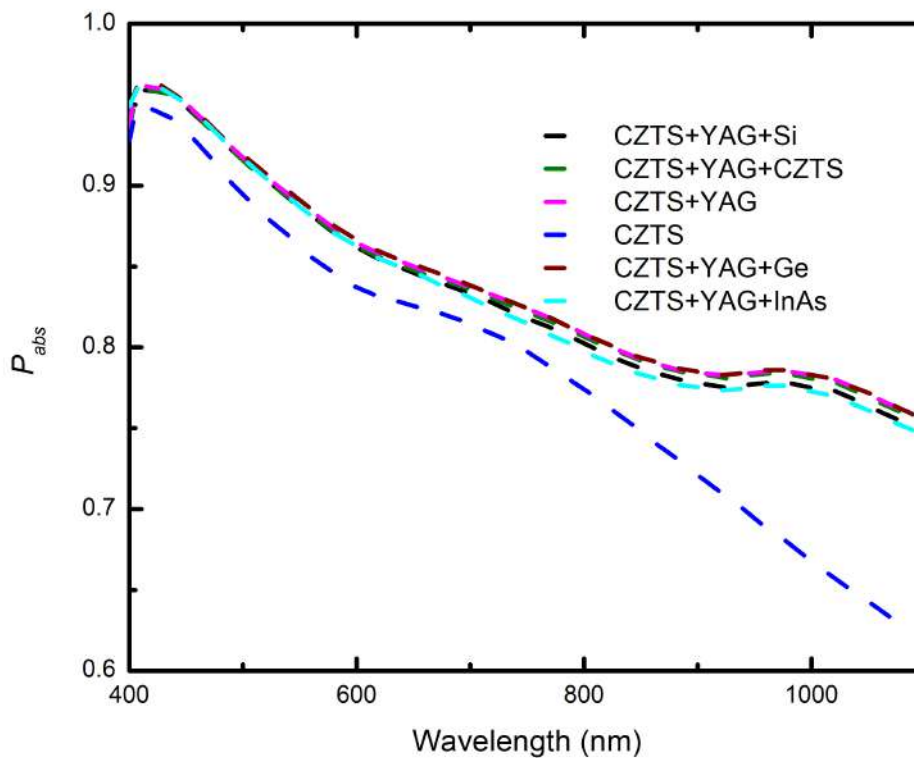


Figure 7.6: Absorption power for bowtie-shaped TiN plasmonic nanoplates with upconverter layer tandem solar cell for different absorber materials. The black line represented the absorbed power for the tandem cells with kesterite in the top layer, a YAG upconverter layer, and Si in the bottom layer. The green line represented the absorbed power for the tandem cells with kesterite in the top layer, a YAG upconverter layer, and kesterite in the bottom layer. The pink line represented the absorbed power for the kesterite in the top layer with a YAG upconverter layer. The blue line represented the absorbed power for the tandem cells with kesterite in the top layer, a YAG upconverter layer, and kesterite in the bottom layer. The wine color line represented the absorbed power for the tandem cells with kesterite in the top layer, a YAG upconverter layer, and Ge in the bottom layer. The cyan color line represented the absorbed power for the tandem cells with kesterite in the top layer, a YAG upconverter layer, and InAs in the bottom layer.

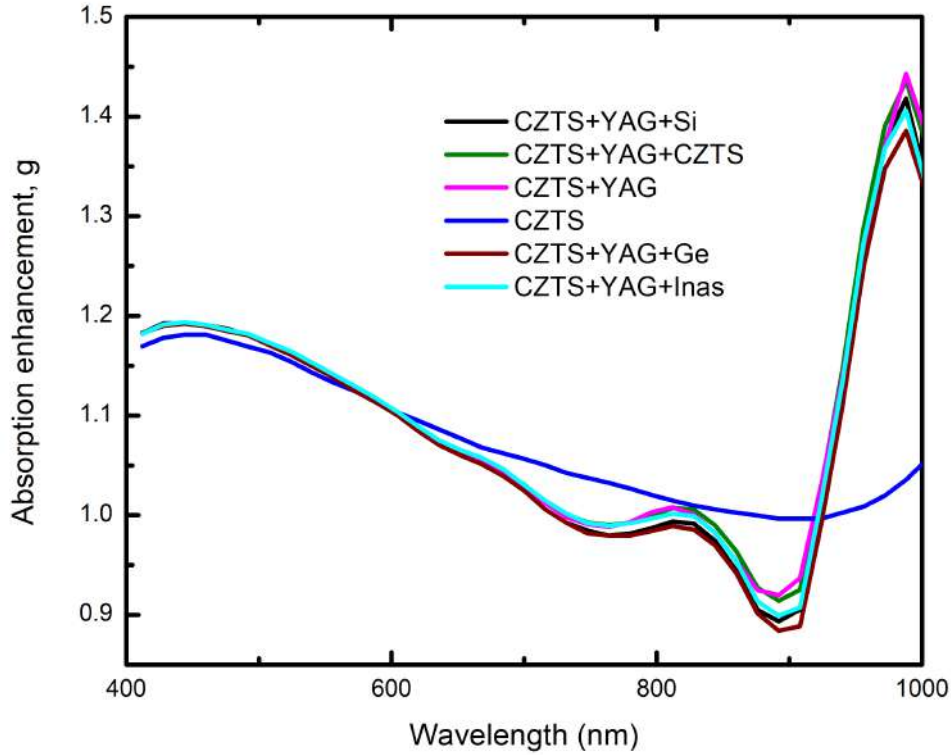


Figure 7.7: Absorption enhancement, g for bowtie-shaped TiN plasmonic nanoplates with upconverter layer tandem solar cell for different absorber materials.

We further compared the absorption enhancement result. The absorption enhancement, g , is defined to show how a solar cell with metal particles performs compared to a bare solar cell. We calculated g from (4.4) for the different absorber layers under the upconverter-incorporated kesterite cell and observed the performance. For tandem cells, we considered silicon with a 1.05 eV bandgap, Ge with a 0.66 eV bandgap, and InAs with a 0.17 eV bandgap. Ge has a larger bandgap than InAs therefore, it has better g than InAs. Silicon has better g than InAs and Ge. As we considered CZTS for both layers, the absorption enhancement performance was better as evident in Figure 7.7. We also observed that with the incorporation of the upconverter layer the absorption enhancement increased. Therefore we considered kesterite tandem solar cells for superior performance.

Chapter 8

Conclusions

8.1 Conclusions

In this dissertation, we first explored the light trapping efficiency, absorption power, and light scattered to the substrate for different plasmonic shapes on si substrate layer photovoltaics. We extensively analyzed monomer, dimer, and triangle forms of nanoparticles. Following calculations and comparison, we selected the ideal shape and size for the nanoparticle and applied it to a kesterite solar cell. The solar cell's power conversion efficiency rose after an up-converter layer was added to reduce transmission loss. Designing and statistically analyzing the electrical and optical performance of the cell with ideal size and shape is the major goal of this thesis. It was crucial to thoroughly investigate kesterite-based plasmonic solar cells in order to choose the right nanoparticle geometry and plasmonic material for kesterite-based solar cells in order to increase path length and hence improve absorption. Moreover, the design and optimization of the upconversion layer for the kesterite solar cell will be beneficial for high-efficiency solar cells. The major results obtained from this research work are summarized as follows:

TiN is a promising alternative plasmonic material for plasmonic and metamaterial applications in visible and near-infrared wavelengths according to the results of our comprehensive study. TiN NPs proved to be a comparable alternative plasmonic material as TiN has a lower carrier concentration and the metallic property in TiN is not lost. Moreover, TiN has larger carrier relaxation rates than those of noble metals. The influence of the TiN spherical nanoparticle on the light absorption enhancement of the thin-film solar cell was studied and revealed to be very promising. The proposed incorporation of NPs in solar cells is feasible for fabrication and showed promising results, it can be a cost-effective and efficient contender. TiN monomer nanoparticles had a better power absorption percentage than Ag, Au, and Al for the whole spectrum on si substrate. It had the highest Q_T value 17 W/m² for 950

nm wavelength. For $r = 15$ nm, the absorption was greater than 1 for the whole wavelength range. Even without intentional optimization, an enhancement factor of 1.2 for a silicon absorber layer was achieved for $r = 100$ nm at 1000 nm wavelength. The power absorption increased from $\sim 19\%$ to $\sim 45\%$ after the addition of TiN NP and further increased to $\sim 53\%$ when we used TiN core-shell NP. The TiN nanosphere incorporated Si PV cell had FF of 0.829 and η of $\sim 22.6\%$.

Dimer of spherical TiN NPs appeared as an efficient alternative plasmonic material for plasmonic and metamaterial applications. The results of our investigation into the effect of TiN dimer spherical NPs on the enhancement of the thin solar cell's light absorption were promising. Comparative analysis of TiN and conventional plasmonic materials suggested that TiN offers comparable performance to Ag and Au for plasmonic applications. By changing the size of TiN dimer NPs, the absorption enhancement peak may be tailored to the required solar spectrum. TiN dimer NPs demonstrated to be beneficial when inserted in tandem solar cells because of their cost-effectiveness along with their abundance and ease to manufacture. After the incorporation of TiN NPs on a silicon substrate, the average absorbed power increased significantly from $\sim 19\%$ to $\sim 75\%$ over the whole spectral range. TiN exhibited better absorption enhancement, g and percentage absorbed power to Ag, Au, and Al dimers for $r = 15$. The average enhancement, G for TiN, Au, and Ag were found to be 0.9972, 0.9953, and 0.9954, respectively, for $r = 15$ nm. TiN dimer NP had the highest Q_{ab} value of ~ 6.2 W/m² which were greater than Ag, Au, and Al.

We showed that particle shape, thickness, source's polarization angle, and dielectric thickness were crucial parameters for designing plasmon-enhanced solar cells. Bowtie-shaped TiN particles with a large fraction of their volume close to the substrate caused effective path length enhancement leading to enhanced near-field coupling. Bowtie-shaped TiN nanoparticle had peak f_{sub} of 0.42. The f_{sub} had no impact on the Si₃N₄ dielectric thickness variation. Hence, the scattering cross-section of the particles can be manipulated by varying the shape, and the thickness of the particles.

We studied the ability to enhance the absorption of the kesterite absorber layer due to the addition of nanoparticles by estimating absorption enhancement and optimizing the shape and size of the nanoparticles. The shapes of nanoparticles investigated are sphere, sphere dimer, and bowtie. The impact of changing the light polarization angle and the thickness of nanoparticles were compared to find out the optimum size and angle. The comparison of the Si and kesterite absorber layer was also analyzed. The results of our study into the effect of TiN NPs on the enhancement of the thin solar cell's light absorption were promising. The bowtie-shaped TiN nanoplate had a higher f_{sub} value of 0.49 for $h=100$ nm on CZTS. The CZTS had a higher f_{sub} value than the Si for both bowtie-shaped NPs. The 100 nm thick bowtie-shaped NP had the highest efficiency at 26.27% and had the $V_{oc} = 0.588$ V and $J_{sc} = 54.01$ mA/cm². The absorbed power for bowtie-shaped TiN NP incorporation enhanced

the average absorption from $\sim 61\%$ to $\sim 88\%$ on the kesterite layer. For $h = 100$ nm the g was greater than 1 for the whole spectral range, and the maximum value was ~ 1.2 . The incorporation of upconverter layer based on YAG increased the solar cell efficiency up to $\sim 28.90\%$. Our proposed design will be beneficial to fabricate high-efficiency thin-film solar cells.

8.2 Future Works

- The benchmarking of the simulation model has been done using planar cells since experimental cells of the model were not available in the literature. Upon the availability of experimental-based studied materials, further model verification is necessary.
- Dimer, monomer, and nanoparticles with triangular forms were used in the solar cell. To determine the optimal performance of light passing through a plasmonic solar cell, additional research can be conducted to assess the performance of different shapes, including hexagon, pentagon, and star-shaped nanoparticles.
- The charge recombination, the sub-band photon transmitted, and the upconversion of the wavelength of a photon cannot be estimated numerically due to the non-linear nature of the upconverter material. To more successfully benchmark the used model, more research is needed on the theoretical and experimental evaluation of upconversion recombination and wavelength transition parameters.
- In a tandem solar cell, additional absorber layers with various band gaps and operating technologies can be added. The absorber layers of a tandem solar cell can be enhanced by plasmonic light concentration. This type of cell can be explored for future prospects.
- Our proposed model was based on alternative plasmonic material TiN. The other alternative plasmonic material can be explored for higher efficiency. Due to their high free electron densities, metallic alloys, intermetallics, and metallic compounds are possible candidates for alternative plasmonic materials. In a single cell, metallic alloys including Ag-Cu, Au-Ag, Ag-Al, Au-Cd, and Ag-In can be investigated.
- Designing and analysis of solar cell with integrated plasmonic nanoparticle and UC/DC layer is necessary for the design and fabrication of high-efficiency thin film solar cells.

References

- [1] A. Tamang, A. Hongsingthong, V. Jovanov, P. Sichanugrist, B. A. Khan, R. Dewan, M. Konagai, and D. Knipp, “Enhanced photon management in silicon thin film solar cells with different front and back interface texture,” *Scientific reports*, vol. 6, no. 1, pp. 1–10, 2016.
- [2] C. Fei Guo, T. Sun, F. Cao, Q. Liu, and Z. Ren, “Metallic nanostructures for light trapping in energy-harvesting devices,” *Light: Science & Applications*, vol. 3, no. 4, pp. e161–e161, 2014.
- [3] M. A. Green, A. Ho-Baillie, and H. J. Snaith, “The emergence of perovskite solar cells,” *Nature photonics*, vol. 8, no. 7, pp. 506–514, 2014.
- [4] E. Manea, E. Budianu, M. Purica, D. Cristea, I. Cernica, R. Muller, and V. M. Poladian, “Optimization of front surface texturing processes for high-efficiency silicon solar cells,” *Solar energy materials and solar cells*, vol. 87, no. 1-4, pp. 423–431, 2005.
- [5] F. Liu, Q. Zeng, J. Li, X. Hao, A. Ho-Baillie, J. Tang, and M. A. Green, “Emerging inorganic compound thin film photovoltaic materials: Progress, challenges and strategies,” *Materials Today*, vol. 41, pp. 120–142, 2020.
- [6] R. Saive, “Light trapping in thin silicon solar cells: A review on fundamentals and technologies,” *Progress in Photovoltaics: Research and Applications*, vol. 29, no. 10, pp. 1125–1137, 2021.
- [7] M. Nakamura, K. Yamaguchi, Y. Kimoto, Y. Yasaki, T. Kato, and H. Sugimoto, “Cd-free cu (in, ga)(se, s) 2 thin-film solar cell with record efficiency of 23.35%,” *IEEE Journal of Photovoltaics*, vol. 9, no. 6, pp. 1863–1867, 2019.
- [8] E. Wesoff, “First solar hits record 22.1% conversion efficiency for cdte solar cell,” *Green Tech Media (PV Modules)*, vol. 24, 2016.
- [9] S. M. Hayes and E. A. McCullough, “Critical minerals: A review of elemental trends in comprehensive criticality studies,” *Resources Policy*, vol. 59, pp. 192–199, 2018.

- [10] M. A. Green, “How did solar cells get so cheap?” *Joule*, vol. 3, no. 3, pp. 631–633, 2019.
- [11] B. Graeser and R. Agrawal, “Pure phase synthesis of Cu_3PS_4 and $\text{Cu}_6\text{PS}_5\text{Cl}$ for semiconductor applications,” *RSC advances*, vol. 8, no. 59, pp. 34 094–34 101, 2018.
- [12] A. Polman, “Plasmonics applied,” *Science*, vol. 322, no. 5903, pp. 868–869, 2008.
- [13] D. T. Gangadharan, Z. Xu, Y. Liu, R. Izquierdo, and D. Ma, “Recent advancements in plasmon-enhanced promising third-generation solar cells,” *Nanophotonics*, vol. 6, no. 1, pp. 153–175, 2017.
- [14] M. Green and S. Pillasi, “Harnessing plasmonics for solar cells, *nat. photonics* 6 (2012) 130–132,” 2012.
- [15] P. Mandal and S. Sharma, “Progress in plasmonic solar cell efficiency improvement: A status review,” *Renewable and sustainable energy reviews*, vol. 65, pp. 537–552, 2016.
- [16] G. Naik, J. Kim, N. Kinsey, and A. Boltasseva, “Alternative plasmonic materials,” in *Handbook of Surface Science*. Elsevier, 2014, vol. 4, pp. 189–221.
- [17] G. V. Naik, J. L. Schroeder, X. Ni, A. V. Kildishev, T. D. Sands, and A. Boltasseva, “Titanium Nitride as a plasmonic material for visible and near-infrared wavelengths,” *Optical Materials Express*, vol. 2, no. 4, pp. 478–489, 2012.
- [18] A. E. Khalifa and M. A. Swillam, “Plasmonic silicon solar cells using Titanium Nitride: a comparative study,” *Journal of Nanophotonics*, vol. 8, no. 1, p. 084098, 2014.
- [19] P. Patsalas, N. Kalfagiannis, and S. Kassavetis, “Optical properties and plasmonic performance of titanium nitride,” *Materials*, vol. 8, no. 6, pp. 3128–3154, 2015.
- [20] N. R. E. Laboratory. Best research-cell efficiency chart. [Online]. Available: <https://www.nrel.gov/pv/cell-efficiency.html>
- [21] X. Qin, A. N. Carneiro Neto, R. L. Longo, Y. Wu, O. L. Malta, and X. Liu, “Surface plasmon–photon coupling in lanthanide-doped nanoparticles,” *The Journal of Physical Chemistry Letters*, vol. 12, no. 5, pp. 1520–1541, 2021.
- [22] T. F. Schulze, J. Czolk, Y.-Y. Cheng, B. Fuckel, R. W. MacQueen, T. Khoury, M. J. Crossley, B. Stannowski, K. Lips, U. Lemmer *et al.*, “Efficiency enhancement of organic and thin-film silicon solar cells with photochemical upconversion,” *The Journal of Physical Chemistry C*, vol. 116, no. 43, pp. 22 794–22 801, 2012.

- [23] D. M. Chapin, C. S. Fuller, and G. L. Pearson, “A new silicon p-n junction photo-cell for converting solar radiation into electrical power,” *Journal of applied physics*, vol. 25, no. 5, pp. 676–677, 1954.
- [24] D. Ginley, M. A. Green, and R. Collins, “Solar energy conversion toward 1 terawatt,” *MRS bulletin*, vol. 33, pp. 355–364, 2008.
- [25] S. Sharma, K. K. Jain, A. Sharma *et al.*, “Solar cells: in research and applications—a review,” *Materials Sciences and Applications*, vol. 6, no. 12, p. 1145, 2015.
- [26] J. Liou and W. Wong, “Comparison and optimization of the performance of si and gaas solar cells,” *Solar Energy Materials and Solar Cells*, vol. 28, no. 1, pp. 9–28, 1992.
- [27] C. Battaglia, A. Cuevas, and S. De Wolf, “High-efficiency crystalline silicon solar cells: status and perspectives,” *Energy & Environmental Science*, vol. 9, no. 5, pp. 1552–1576, 2016.
- [28] S. Roy, M. S. Baruah, S. Sahu, and B. B. Nayak, “Computational analysis on the thermal and mechanical properties of thin film solar cells,” *Materials Today: Proceedings*, vol. 44, pp. 1207–1213, 2021.
- [29] O. Vigil-Galán, M. Courel, J. Andrade-Arvizu, Y. Sánchez, M. Espíndola-Rodríguez, E. Saucedo, D. Seuret-Jiménez, and M. Titsworth, “Route towards low cost-high efficiency second generation solar cells: current status and perspectives,” *Journal of Materials Science: Materials in Electronics*, vol. 26, pp. 5562–5573, 2015.
- [30] M. Kumar, A. Dubey, N. Adhikari, S. Venkatesan, and Q. Qiao, “Strategic review of secondary phases, defects and defect-complexes in kesterite czts–se solar cells,” *Energy & Environmental Science*, vol. 8, no. 11, pp. 3134–3159, 2015.
- [31] Y. Tong, Z. Xiao, X. Du, C. Zuo, Y. Li, M. Lv, Y. Yuan, C. Yi, F. Hao, Y. Hua *et al.*, “Progress of the key materials for organic solar cells,” *Science China Chemistry*, vol. 63, pp. 758–765, 2020.
- [32] N. S. Kumar and K. C. B. Naidu, “A review on perovskite solar cells (pscs), materials and applications,” *Journal of Materiomics*, vol. 7, no. 5, pp. 940–956, 2021.
- [33] J. Chen, D. Jia, E. M. Johansson, A. Hagfeldt, and X. Zhang, “Emerging perovskite quantum dot solar cells: feasible approaches to boost performance,” *Energy & Environmental Science*, vol. 14, no. 1, pp. 224–261, 2021.
- [34] C. Ng, L. Wesemann, E. Panchenko, J. Song, T. J. Davis, A. Roberts, and D. E. Gómez, “Plasmonic near-complete optical absorption and its applications,” *Advanced Optical Materials*, vol. 7, no. 14, p. 1801660, 2019.

- [35] K. Zhou, K. Xian, and L. Ye, “Morphology control in high-efficiency all-polymer solar cells,” *InfoMat*, vol. 4, no. 4, p. e12270, 2022.
- [36] J. Yan and B. R. Saunders, “Third-generation solar cells: a review and comparison of polymer: fullerene, hybrid polymer and perovskite solar cells,” *Rsc Advances*, vol. 4, no. 82, pp. 43 286–43 314, 2014.
- [37] P. Vivo, J. K. Salunke, and A. Priimagi, “Hole-transporting materials for printable perovskite solar cells,” *Materials*, vol. 10, no. 9, p. 1087, 2017.
- [38] M. M. A. MOON, M. F. RAHMAN, and A. B. M. ISMAIL, “Optimization of active region thickness of cdte/cds thin film superstrate solar cell to achieve ~ 25% efficiency: A simulation approach,” in *2018 International Conference on Computer, Communication, Chemical, Material and Electronic Engineering (IC4ME2)*. IEEE, 2018, pp. 1–4.
- [39] S. K. Wallace, D. B. Mitzi, and A. Walsh, “The steady rise of kesterite solar cells,” *ACS Energy Letters*, vol. 2, no. 4, pp. 776–779, 2017.
- [40] A. Wang, M. He, M. A. Green, K. Sun, and X. Hao, “A critical review on the progress of kesterite solar cells: Current strategies and insights,” *Advanced Energy Materials*, vol. 13, no. 2, p. 2203046, 2023.
- [41] D. B. Mitzi, O. Gunawan, T. K. Todorov, K. Wang, and S. Guha, “The path towards a high-performance solution-processed kesterite solar cell,” *Solar Energy Materials and Solar Cells*, vol. 95, no. 6, pp. 1421–1436, 2011.
- [42] X. Liu, Y. Feng, H. Cui, F. Liu, X. Hao, G. Conibeer, D. B. Mitzi, and M. Green, “The current status and future prospects of kesterite solar cells: a brief review,” *Progress in Photovoltaics: Research and Applications*, vol. 24, no. 6, pp. 879–898, 2016.
- [43] M. He, C. Yan, J. Li, M. P. Suryawanshi, J. Kim, M. A. Green, and X. Hao, “Kesterite solar cells: insights into current strategies and challenges,” *Advanced Science*, vol. 8, no. 9, p. 2004313, 2021.
- [44] P. Yu, F. Zhang, Z. Li, Z. Zhong, A. Govorov, L. Fu, H. Tan, C. Jagadish, and Z. Wang, “Giant optical pathlength enhancement in plasmonic thin film solar cells using core-shell nanoparticles,” *Journal of Physics D: Applied Physics*, vol. 51, no. 29, p. 295106, 2018.
- [45] F. Marangi, M. Lombardo, A. Villa, and F. Scotognella, “New strategies for solar cells beyond the visible spectral range,” *Optical Materials: X*, vol. 11, p. 100083, 2021.

- [46] Y. H. Jang, Y. J. Jang, S. Kim, L. N. Quan, K. Chung, and D. H. Kim, "Plasmonic solar cells: from rational design to mechanism overview," *Chemical Reviews*, vol. 116, no. 24, pp. 14 982–15 034, 2016.
- [47] F. Enrichi, A. Quandt, and G. C. Righini, "Plasmonic enhanced solar cells: Summary of possible strategies and recent results," *Renewable and Sustainable Energy Reviews*, vol. 82, pp. 2433–2439, 2018.
- [48] K. Ueno, T. Oshikiri, Q. Sun, X. Shi, and H. Misawa, "Solid-state plasmonic solar cells," *Chemical Reviews*, vol. 118, no. 6, pp. 2955–2993, 2017.
- [49] M. S. ISLAM and A. ZUBAIR, "Plasmon tuning in ultra-thin titanium nitride films," 2023, unpublished.
- [50] J. R. Nagel and M. A. Scarpulla, "Enhanced absorption in optically thin solar cells by scattering from embedded dielectric nanoparticles," *Optics express*, vol. 18, no. 102, pp. A139–A146, 2010.
- [51] P. H. Wang, R.-E. Nowak, S. Geißendörfer, M. Vehse, N. Reininghaus, O. Sergeev, K. von Maydell, A. G. Brolo, and C. Agert, "Cost-effective nanostructured thin-film solar cell with enhanced absorption," *Applied Physics Letters*, vol. 105, no. 18, p. 183106, 2014.
- [52] K. Catchpole and A. Polman, "Design principles for particle plasmon enhanced solar cells," *Applied Physics Letters*, vol. 93, no. 19, p. 191113, 2008.
- [53] N. Zhou, V. López-Puente, Q. Wang, L. Polavarapu, I. Pastoriza-Santos, and Q.-H. Xu, "Plasmon-enhanced light harvesting: applications in enhanced photocatalysis, photodynamic therapy and photovoltaics," *Rsc Advances*, vol. 5, no. 37, pp. 29 076–29 097, 2015.
- [54] J. Ramanujam, D. M. Bishop, T. K. Todorov, O. Gunawan, J. Rath, R. Nekovei, E. Arregiani, and A. Romeo, "Flexible cigs, cdte and a-si: H based thin film solar cells: A review," *Progress in Materials Science*, vol. 110, p. 100619, 2020.
- [55] D.-L. Wang, H.-J. Cui, G.-J. Hou, Z.-G. Zhu, Q.-B. Yan, and G. Su, "Highly efficient light management for perovskite solar cells," *Scientific Reports*, vol. 6, no. 1, pp. 1–10, 2016.
- [56] M. I. Tahmid, M. A. Z. Mamun, and A. Zubair, "Near-perfect absorber consisted of a vertical array of single-wall carbon nanotubes and engineered multi-wall carbon nanotubes," *Opt. Mater. Express*, vol. 11, no. 4, pp. 1267–1281, Apr 2021. [Online]. Available: <https://opg.optica.org/ome/abstract.cfm?URI=ome-11-4-1267>

- [57] M. A. Hasan and A. Zubair, “Cross diabolo hollow notch nanotweezer for optical trapping and manipulation,” *IEEE Photonics Journal*, vol. 14, no. 2, pp. 1–10, 2022.
- [58] D. J. de Aberasturi, A. B. Serrano-Montes, and L. M. Liz-Marzán, “Modern applications of plasmonic nanoparticles: from energy to health,” *Advanced Optical Materials*, vol. 3, no. 5, pp. 602–617, 2015.
- [59] S. Ahn, D. Rourke, and W. Park, “Plasmonic nanostructures for organic photovoltaic devices,” *Journal of Optics*, vol. 18, no. 3, p. 033001, 2016.
- [60] L. Ma, Y.-L. Chen, D.-J. Yang, H.-X. Li, S.-J. Ding, L. Xiong, P.-L. Qin, and X.-B. Chen, “Multi-interfacial plasmon coupling in multigap (Au/Ag)@ cds core–shell hybrids for efficient photocatalytic hydrogen generation,” *Nanoscale*, vol. 12, no. 7, pp. 4383–4392, 2020.
- [61] X. Wang, J. Jian, H. Wang, J. Liu, Y. Pachaury, P. Lu, B. X. Rutherford, X. Gao, X. Xu, A. El-Azab *et al.*, “Nitride-oxide-metal heterostructure with self-assembled core–shell nanopillar arrays: Effect of ordering on magneto-optical properties,” *Small*, vol. 17, no. 5, p. 2007222, 2021.
- [62] M. Ivanchenko, V. Nooshnab, A. F. Myers, N. Large, A. J. Evangelista, and H. Jing, “Enhanced dual plasmonic photocatalysis through plasmonic coupling in eccentric noble metal-nonstoichiometric copper chalcogenide hetero-nanostructures,” *Nano Research*, vol. 15, pp. 1579–1586, 2022.
- [63] M. Xue, L. Li, B. J. Tremolet de Villers, H. Shen, J. Zhu, Z. Yu, A. Z. Stieg, Q. Pei, B. J. Schwartz, and K. L. Wang, “Charge-carrier dynamics in hybrid plasmonic organic solar cells with ag nanoparticles,” *Applied Physics Letters*, vol. 98, no. 25, p. 119, 2011.
- [64] K. M. Mayer and J. H. Hafner, “Localized surface plasmon resonance sensors,” *Chemical reviews*, vol. 111, no. 6, pp. 3828–3857, 2011.
- [65] M. Ihara, K. Tanaka, K. Sakaki, I. Honma, and K. Yamada, “Enhancement of the absorption coefficient of cis-(ncs) 2 bis (2, 2 ‘-bipyridyl-4, 4 ‘-dicarboxylate) ruthenium (ii) dye in dye-sensitized solar cells by a silver island film,” *The Journal of Physical Chemistry B*, vol. 101, no. 26, pp. 5153–5157, 1997.
- [66] A. Baba, K. Wakatsuki, K. Shinbo, K. Kato, and F. Kaneko, “Increased short-circuit current in grating-coupled surface plasmon resonance field-enhanced dye-sensitized solar cells,” *Journal of Materials Chemistry*, vol. 21, no. 41, pp. 16 436–16 441, 2011.

- [67] S. D. Standridge, G. C. Schatz, and J. T. Hupp, “Distance dependence of plasmon-enhanced photocurrent in dye-sensitized solar cells,” *Journal of the American Chemical Society*, vol. 131, no. 24, pp. 8407–8409, 2009.
- [68] B. S. Richards, D. Hudry, D. Busko, A. Turshatov, and I. A. Howard, “Photon upconversion for photovoltaics and photocatalysis: a critical review: focus review,” *Chemical Reviews*, vol. 121, no. 15, pp. 9165–9195, 2021.
- [69] J. De Wild, A. Meijerink, J. Rath, W. Van Sark, and R. Schropp, “Upconverter solar cells: materials and applications,” *Energy & Environmental Science*, vol. 4, no. 12, pp. 4835–4848, 2011.
- [70] S. Fischer, A. Ivaturi, P. Jakob, K. W. Krämer, R. Martin-Rodriguez, A. Meijerink, B. Richards, and J. C. Goldschmidt, “Upconversion solar cell measurements under real sunlight,” *Optical materials*, vol. 84, pp. 389–395, 2018.
- [71] F. Habashi, V. Tsimmerman, and C. Runge, “the periodic table,” *Chem. Educator*, vol. 18, pp. 6–8, 2013.
- [72] F. Lahoz, C. Pérez-Rodríguez, S. Hernández, I. Martín, V. Lavín, and U. Rodríguez-Mendoza, “Upconversion mechanisms in rare-earth doped glasses to improve the efficiency of silicon solar cells,” *Solar energy materials and solar cells*, vol. 95, no. 7, pp. 1671–1677, 2011.
- [73] W. G. van Sark, J. de Wild, J. K. Rath, A. Meijerink, and R. E. Schropp, “Upconversion in solar cells,” *Nanoscale research letters*, vol. 8, pp. 1–10, 2013.
- [74] J.-F. Masson, “Portable and field-deployed surface plasmon resonance and plasmonic sensors,” *Analyst*, vol. 145, no. 11, pp. 3776–3800, 2020.
- [75] J. Mertz, “Radiative absorption, fluorescence, and scattering of a classical dipole near a lossless interface: a unified description,” *JOSA B*, vol. 17, no. 11, pp. 1906–1913, 2000.
- [76] M. Hoese, M. K. Koch, F. Breuning, N. Lettner, K. G. Fehler, and A. Kubanek, “Single photon randomness originating from the symmetric dipole emission pattern of quantum emitters,” *Applied Physics Letters*, vol. 120, no. 4, p. 044001, 2022.
- [77] A. Yang, D. Wang, W. Wang, and T. W. Odom, “Coherent light sources at the nanoscale,” *Annual Review of Physical Chemistry*, vol. 68, pp. 83–99, 2017.
- [78] U. Kreibig and M. Vollmer, *Optical properties of metal clusters*. Springer Science & Business Media, 2013, vol. 25.

- [79] T. P. L. Ung, “Désordre contrôlé sur des nanostructures métalliques pour des applications en plasmonique,” Ph.D. dissertation, Université Paris Saclay (COmUE), 2018.
- [80] P. H. Rekemeyer, C.-H. M. Chuang, M. G. Bawendi, and S. Gradecak, “Minority carrier transport in Lead Sulfide quantum dot photovoltaics,” *Nano letters*, vol. 17, no. 10, pp. 6221–6227, 2017.
- [81] T. L. Zinenko, V. O. Byelobrov, M. Marciniak, J. Čtyroký, and A. I. Nosich, “Grating resonances on periodic arrays of sub-wavelength wires and strips: from discoveries to photonic device applications,” *Contemporary optoelectronics: materials, metamaterials and device applications*, pp. 65–79, 2016.
- [82] K. Frischwasser, K. Cohen, J. Kher-Alden, S. Dolev, S. Tsesses, and G. Bartal, “Real-time sub-wavelength imaging of surface waves with nonlinear near-field optical microscopy,” *Nature Photonics*, vol. 15, no. 6, pp. 442–448, 2021.
- [83] N. Kholmicheva, L. R. Romero, J. Cassidy, and M. Zamkov, “Prospects and applications of plasmon-exciton interactions in the near-field regime,” *Nanophotonics*, vol. 8, no. 4, pp. 613–628, 2019.
- [84] H. A. Atwater and A. Polman, “Plasmonics for improved photovoltaic devices,” *Materials for sustainable energy: a collection of peer-reviewed research and review articles from Nature Publishing Group*, pp. 1–11, 2011.
- [85] V. E. Ferry, M. A. Verschuuren, H. B. Li, R. E. Schropp, H. A. Atwater, and A. Polman, “Improved red-response in thin film a-si:h solar cells with soft-imprinted plasmonic back reflectors,” *Applied physics letters*, vol. 95, no. 18, p. 183503, 2009.
- [86] V. Giannini, Y. Zhang, M. Forcales, and J. G. Rivas, “Long-range surface polaritons in ultra-thin films of silicon,” *Optics express*, vol. 16, no. 24, pp. 19 674–19 685, 2008.
- [87] J. Mapel, M. Singh, M. Baldo, and K. Celebi, “Plasmonic excitation of organic double heterostructure solar cells,” *Applied physics letters*, vol. 90, no. 12, 2007.
- [88] K. Tvingstedt, N.-K. Persson, O. Inganäs, A. Rahachou, and I. V. Zozoulenko, “Surface plasmon increase absorption in polymer photovoltaic cells,” *Applied Physics Letters*, vol. 91, no. 11, 2007.
- [89] J. B. Khurgin, “Replacing noble metals with alternative materials in plasmonics and metamaterials: how good an idea?” *Philosophical Transactions of the Royal Society A: Mathematical, Physical and Engineering Sciences*, vol. 375, no. 2090, p. 20160068, 2017.

- [90] N. Kinsey, M. Ferrera, V. Shalaev, and A. Boltasseva, “Examining nanophotonics for integrated hybrid systems: a review of plasmonic interconnects and modulators using traditional and alternative materials,” *JOSA B*, vol. 32, no. 1, pp. 121–142, 2015.
- [91] Y. Wang, A. Capretti, and L. Dal Negro, “Wide tuning of the optical and structural properties of alternative plasmonic materials,” *Optical Materials Express*, vol. 5, no. 11, pp. 2415–2430, 2015.
- [92] G. V. Naik, J. Kim, and A. Boltasseva, “Oxides and Nitrides as alternative plasmonic materials in the optical range,” *Optical materials express*, vol. 1, no. 6, pp. 1090–1099, 2011.
- [93] M. Raugei and E. Leccisi, “A comprehensive assessment of the energy performance of the full range of electricity generation technologies deployed in the united kingdom,” *Energy Policy*, vol. 90, pp. 46–59, 2016.
- [94] C. Clavero, “Plasmon-induced hot-electron generation at nanoparticle/metal-oxide interfaces for photovoltaic and photocatalytic devices,” *Nature Photonics*, vol. 8, no. 2, pp. 95–103, 2014.
- [95] L. Kuzu, “Electromagnetic scattering from chiral materials using the finite difference frequency domain method,” 2006.
- [96] Y. Zhang, H. Sun, S. Zhang, S. Li, X. Wang, X. Zhang, T. Liu, and Z. Guo, “Enhancing luminescence in all-inorganic perovskite surface plasmon light-emitting diode by incorporating au-ag alloy nanoparticle,” *Optical Materials*, vol. 89, pp. 563–567, 2019.
- [97] Z. Wang and P. Cheng, “Enhancements of absorption and photothermal conversion of solar energy enabled by surface plasmon resonances in nanoparticles and metamaterials,” *International Journal of Heat and Mass Transfer*, vol. 140, pp. 453–482, 2019.
- [98] R. Sangno, S. Maity, and R. Mehta, “Plasmonic effect due to silver nanoparticles on silicon solar cell,” *Procedia Computer Science*, vol. 92, pp. 549–553, 2016.
- [99] L. Wang, M. Hasanzadeh Kafshgari, and M. Meunier, “Optical properties and applications of plasmonic-metal nanoparticles,” *Advanced Functional Materials*, vol. 30, no. 51, p. 2005400, 2020.
- [100] D. Titus, E. J. J. Samuel, and S. M. Roopan, “Nanoparticle characterization techniques,” in *Green synthesis, characterization and applications of nanoparticles*. Elsevier, 2019, pp. 303–319.

- [101] A. A. Tabrizi and A. Pahlavan, “Efficiency improvement of a silicon-based thin-film solar cell using plasmonic silver nanoparticles and an antireflective layer,” *Optics communications*, vol. 454, p. 124437, 2020.
- [102] F. Qin, X. Chen, Z. Yi, W. Yao, H. Yang, Y. Tang, Y. Yi, H. Li, and Y. Yi, “Ultra-broadband and wide-angle perfect solar absorber based on tin nanodisk and ti thin film structure,” *Solar Energy Materials and Solar Cells*, vol. 211, p. 110535, 2020.
- [103] N. Akhtary and A. Zubair, “Titanium nitride based plasmonic nanoparticles for photovoltaic application,” *Opt. Continuum*, vol. 2, no. 7, pp. 1701–1715, Jul 2023.
- [104] S. Ferré, A. Peinado, E. Garcia-Caurel, V. Trinité, M. Carras, and R. Ferreira, “Comparative study of sio₂, si₃n₄ and tio₂ thin films as passivation layers for quantum cascade lasers,” *Optics express*, vol. 24, no. 21, pp. 24 032–24 044, 2016.
- [105] E. D. Palik, *Handbook of optical constants of solids*. Academic press, 1998, vol. 3.
- [106] J. Kischkat, S. Peters, B. Gruska, M. Semtsiv, M. Chashnikova, M. Klinkmüller, O. Fedosenko, S. Machulik, A. Aleksandrova, G. Monastyrskiy *et al.*, “Mid-infrared optical properties of thin films of aluminum oxide, titanium dioxide, silicon dioxide, aluminum nitride, and silicon nitride,” *Applied optics*, vol. 51, no. 28, pp. 6789–6798, 2012.
- [107] M. Xi, S. Ding, N. Li, and Z. Wang, “Angular scattered light intensity of dipole–multipole plasmonic hybridization,” *The Journal of Physical Chemistry C*, vol. 125, no. 42, pp. 23 231–23 239, 2021.
- [108] C. Mahala, M. D. Sharma, and M. Basu, “Near-field and far-field plasmonic effects of gold nanoparticles decorated on zno nanosheets for enhanced solar water splitting,” *ACS Applied Nano Materials*, vol. 3, no. 2, pp. 1153–1165, 2020.
- [109] N. Kongsuwan, A. Demetriadou, M. Horton, R. Chikkaraddy, J. J. Baumberg, and O. Hess, “Plasmonic nanocavity modes: From near-field to far-field radiation,” *ACS Photonics*, vol. 7, no. 2, pp. 463–471, 2020.
- [110] L. Schumacher, J. Jose, D. Janoschka, P. Dreher, T. Davis, M. Ligges, R. Li, M. Mo, S. Park, X. Shen *et al.*, “Precision plasmonics with monomers and dimers of spherical gold nanoparticles: nonequilibrium dynamics at the time and space limits,” *The Journal of Physical Chemistry C*, vol. 123, no. 21, pp. 13 181–13 191, 2019.
- [111] W. Ye, R. Long, H. Huang, and Y. Xiong, “Plasmonic nanostructures in solar energy conversion,” *Journal of Materials Chemistry C*, vol. 5, no. 5, pp. 1008–1021, 2017.

- [112] C. F. Bohren and D. R. Huffman, *Absorption and scattering of light by small particles*. John Wiley & Sons, 2008.
- [113] M. Pascale, G. Miano, R. Tricarico, and C. Forestiere, “Full-wave electromagnetic modes and hybridization in nanoparticle dimers,” *Scientific reports*, vol. 9, no. 1, p. 14524, 2019.
- [114] N. Venugopal, V. Gerasimov, A. Ershov, S. Karpov, and S. Polyutov, “Titanium nitride as light trapping plasmonic material in silicon solar cell,” *Optical Materials*, vol. 72, pp. 397–402, 2017.
- [115] T.-S. Deng, J. Parker, Y. Yifat, N. Shepherd, and N. F. Scherer, “Dark plasmon modes in symmetric gold nanoparticle dimers illuminated by focused cylindrical vector beams,” *The Journal of Physical Chemistry C*, vol. 122, no. 48, pp. 27 662–27 672, 2018.
- [116] T. D. Lee and A. U. Ebong, “A review of thin film solar cell technologies and challenges,” *Renewable and Sustainable Energy Reviews*, vol. 70, pp. 1286–1297, 2017.
- [117] N. Kholmicheva, L. Royo Romero, J. Cassidy, and M. Zamkov, “Prospects and applications of plasmon-exciton interactions in the near-field regime,” *Nanophotonics*, vol. 8, no. 4, pp. 613–628, 2018.
- [118] S. Adachi, “Physical properties: compiled experimental data,” *Copper Zinc Tin Sulfide-Based Thin-Film Solar Cells*, pp. 149–179, 2014.
- [119] A. Ziti, B. Hartiti, H. Labrim, S. Fadili, A. Batan, A. Ridah, and P. Thevenin, “Growth and characterization of czts thin films synthesized by electrodeposition method for photovoltaic applications,” in *IOP Conference Series: Materials Science and Engineering*, vol. 948, no. 1. IOP Publishing, 2020, p. 012025.
- [120] A. Haddout, A. Raidou, and M. Fahoume, “A review on the numerical modeling of cds/czts-based solar cells,” *Applied physics A*, vol. 125, pp. 1–16, 2019.
- [121] N. Akhtary and A. Zubair, “Light trapping using dimer of spherical nanoparticles based on titanium nitride for plasmonic solar cells,” 2023.
- [122] D. Verma, T. O. Saetre, and O.-M. Midtgård, “Review on up/down conversion materials for solar cell application,” in *2012 38th IEEE Photovoltaic Specialists Conference*. IEEE, 2012, pp. 002 608–002 613.
- [123] B. G. Akinoglu, B. Tuncel, and V. Badescu, “Beyond 3rd generation solar cells and the full spectrum project. recent advances and new emerging solar cells,” *Sustainable Energy Technologies and Assessments*, vol. 46, p. 101287, 2021.

- [124] G. Kakavelakis, K. Petridis, and E. Kymakis, “Recent advances in plasmonic metal and rare-earth-element upconversion nanoparticle doped perovskite solar cells,” *Journal of Materials Chemistry A*, vol. 5, no. 41, pp. 21 604–21 624, 2017.
- [125] X. Huang, N. Cutinha, A. A. de Velasco, P. Chandler, and P. Townsend, “Upconversion in erbium doped yag ion-implanted waveguides,” *Nuclear Instruments and Methods in Physics Research Section B: Beam Interactions with Materials and Atoms*, vol. 142, no. 1-2, pp. 50–60, 1998.